ABSTRACT

Title of Document:	USE OF 3D PRINTED POLY(PROPYLENE FUMARATE) SCAFFOLDS FOR THE DELIVERY OF DYNAMICALLY CULTURED HUMAN MESENCHYMAL STEM CELLS AS A MODEL METHOD TO TREAT BONE DEFECTS
	Martha Elizabeth Ottenberg Wang, Doctor of Philosophy, 2014
Directed By:	John P. Fisher, Ph.D., Fischell Family Distinguished Professor Fischell Department of Bioengineering

This project investigates the use of a tissue engineering approach of an absorbable polymer, poly(propylene fumarate) (PPF) to provide long term mechanical stability while delivering a bioactive material, precultured human mesenchymal stem cells (hMSC) encapsulated in hydrogel, to repair bone defects. Annually over 2.2 million bone grafting procedures are performed worldwide; however, current treatment options are limited for critically sized and load bearing bone defects. Much progress has been made in development of bone tissue replacements within the field of bone tissue engineering. The combination of a polymer scaffold seeded with cells for the eventual replacement by host tissue has

shown significant promise. One such polymer is PPF, a synthetic linear polyester. PPF has been shown to be biocompatible, biodegradable and provide sufficient mechanical strength for bone tissue engineering applications. Additionally PPF is able to be photocrosslinked and therefore can be fabricated into specific geometries using advanced three-dimensional (3-D) rapid prototyping. Current technology to culture and differentiate hMSCs into osteoblasts has been enhanced with the development of the tubular perfusion system (TPS). The TPS bioreactor has been shown to enhance osteoblastic differentiation in hMSCs when encapsulated in alginate beads. Although this system is effective in differentiating hMSCs it lacks the sufficient mechanical strength for the treatment of bone defects. Therefore this work suggests a combination strategy of harnessing the ability of the TPS bioreactor to enhance osteoblastic differentiation with the mechanical properties of poly(propylene fumarate) to develop a porous PPF sleeve scaffold for the treatment of bone defects. This is accomplished through four steps. The first step investigates the cytotoxicity of the polymer PPF. Concurrently the second step focuses on designing, fabricating and characterizing PPF scaffolds. The third step investigates the degradation properties of 3D printed porous PPF scaffolds. The fourth step characterizes alginate bead size and composition for use within the PPF sleeve scaffolds. The successful completion of these aims will develop a functional biodegradable bone tissue engineering strategy that utilizes PPF fabricated scaffolds for use with the TPS bioreactor.

USE OF 3D PRINTED POLY(PROPYLENE FUMARATE) SCAFFOLDS FOR THE DELIVERY OF DYNAMICALLY CULTURED HUMAN MESENCHYMAL STEM CELLS AS A MODEL METHOD TO TREAT BONE DEFECTS

By

Martha Elizabeth Ottenberg Wang

Dissertation submitted to the Faculty of the Graduate School of the
University of Maryland, College Park, in partial fulfillment
of the requirements for the degree of
Doctorate of Philosophy
2014

Advisory Committee:

Dr. John P. Fisher	Professor, Fischell Department of Bioengineering, Committee Chair
Dr. Maureen Dreher	Biomedical Engineer, Division of Solid and Fluid Mechanics, Office of Science and Engineering Laboratories, Center for Devices and Radiological Health, Food and Drug Administration
Dr. Adam Hsieh	Associate Professor, Fischell Department of Bioengineering
Dr. Isabel Lloyd	Associate Professor, Department of Material Science and Engineering
Dr. Silvina Matysiak	Assistant Professor, Fischell Department of Bioengineering

Dedication

To my husband, Jim, for without his love and support this would not have been possible.

Acknowledgements

I would like to thank my advisor, John P. Fisher, for without his support and guidance this work would not have been possible. I would also like to thank Maureen L. Dreher for all of her instruction and help during all of the work characterizing our scaffolds. I would also like to thank my committee members for their helpful questions and suggestions throughout this process.

I would also like to acknowledge the undergraduate researchers whose work contributed significantly to this project: Joshua Thompson for his work with the TPS bioreactor, Charlotte Vorwald for her expertise in PPF synthesis and modular design skills, Julie Etheridge for her work in evaluating the cytotoxicity of PPF. I would also like to thank Charlotte Piard, for her contributions to the degradation study and who was invaluable in lab. I'd also like to thank Paola Pisanti for her friendship during her time in the US. And to all of my labmates, thank you for all your help and support over the years.

Last but not least, I would like to recognize my family for all that they have done for me. To my grandfather, Leonard Wenzel, thank you for starting me down this path so many years ago. To my parents, thank you for your never-ending support, optimism, and encouragement. To my husband, Jim, thank you for your guidance, patience, support, and most importantly, your encouragement. And to my children, Alexander and Elizabeth, thank you for showing me how much joy there is in life.

Table of Contents

List of Tables

List of Figures

Chapter 1: Introduction, Objectives and Background

1.1 Introduction

Although there are an estimated 2.2 million bone graft cases performed annually worldwide there is still a lack of clinical treatment options.[2] Bone tissue engineering has emerged to develop alternative methods for the treatment of bone defects. Bone defects are currently repaired by using bone grafts; cements; metal rods, plates and screws; and some polymers. Successful resolution of bone defects requires the treatment to be noncytotoxic, mechanically strong, and if degradable, it must be efficacious at enhancing tissue ingrowth during the period of host integration. Bone tissue engineering believes that the optimal tissue replacement could be generated with a porous scaffold, mimicking the bone's natural environment for cells seeded in the scaffold. This is believed to allow for both host tissue in-growth and scaffold tissue growth *in situ*.[3]

Of the 2.2 million bone grafting cases allograft, autograft and xenograft are often used as repair products. However, each of these has their individual drawbacks such as pain, infection and disease transmission.[2, 4, 5] Other materials that are used for bone repair include non-skeletally sourced materials such as metals, ceramics and polymers. Current research has identified that use of metals for bone graft repairs may provide sufficient physical strength but have poor patient site integration.[6] Additionally metal repairs are unable to grow or be remodeled along with the natural physiological demands of the patient.[7] Though ceramics tend to be brittle they are biocompatible and some have been shown to be osteoconductive.[8] Some of the most studied ceramics are based on biodegradable tricalcium phosphate and hydroxyapatite.[9] However since HA lacks sufficient mechanical strength it is not used solely to repair load bearing bone defects.

Therefore much research has been performed on the suitability of polymers for bone tissue engineering. Polymers can fill both the need for strength and patient site integration. Most recent

biomaterial research for bone tissue engineering has focused on biodegradable polymers due to their ability for cell seeding, dynamic scaffold design to match defect shape and size perfectly and for their biocompatibility.[10]

Development of a successful scaffold for bone tissue engineering depends on the polymer's physical and biological characteristics. For successful implantation into the defect site, the polymer, plus any other materials used during fabrication, must be: strong, noncytotoxic, biodegradable, and easily sterilizable.[3, 11] For scaffold fabrication using rapid prototyping such as stereolithography, the polymer must be photopolymerizable with a non-cytotoxic initiator and have low viscosity at high molecular weights. Once these characteristics of the polymer are fulfilled, then the design of an optimized scaffold may begin. To fabricate scaffold designs that have precise geometries and mechanically strong we utilized three dimensional (3D) printing. The bioactive material in this case are human mesenchymal stem cells (hMSC), encapsulated in alginate. The alginate constructs are precultured in a perfusion bioreactor to enhance osteogenic differentiation. We hypothesize that the absorbable polymer carrier scaffold and the hMSC encapsulated in alginate would provide a novel tissue engineering method for the treatment of bone tissue defects.

1.2 Objectives

The overall objective of this work is to develop a combination strategy to harness the ability of the TPS bioreactor to enhance osteoblastic differentiation with the mechanical properties of poly(propylene fumarate) (PPF) for the treatment of bone defects. This goal is accomplished through the following objectives:

1. The first objective was to evaluate the cellular response elicited when exposed to poly(propylene fumarate). Before investigating the use of PPF as a component to treat bone defects we first had to ensure that it is noncytotoxic when implanted *in vivo*. This was accomplished through evaluating the cellular response of four different cell types under three different culture conditions.

2. The second objective was to design and investigate the use of porous PPF scaffolds. These porous PPF scaffolds were fabricated using three dimensional (3D) printing technology. The range of scaffold parameters such as pore size, wall thickness, and porosity were first investigated using a modular design approach. Of the wide range of designs possible, twelve designs were investigated further for their vascularization potential. *In silico* modeling was used to evaluate the impact of scaffold parameters on vascularization. Concurrently scaffolds were 3D printed and implanted in an in vivo subcutaneous rat model to provide a qualitative comparison.
3. The third objective was to evaluate the structural and cytocompatibility properties of 3D printed PPF scaffolds during *in vitro* degradation. This was accomplished by degrading 3D printed scaffolds over a 32 week time period. At each timepoint changes in scaffold mechanical and structural properties were evaluated. Concurrently, the cytotoxicity of degradation byproducts was measured to predict if the PPF scaffold would elicit a cytotoxic response when implanted.
4. The fourth objective was to characterize the size and composition of alginate beads to act as the bioactive component of our combination strategy. These alginate beads contain human mesenchymal stem cells (hMSCs) which are dynamically cultured in the TPS bioreactor to enhance osteoblastic differentiation. Additionally hydroxyapatite was investigated to enhance osteoblastic differentiation under dynamic culture conditions. The work for each of these objectives is detailed in the following chapters.

1.3 Background: Bone Repair Strategies and Toxicity Testing

1.3.1 Introduction

Material biocompatibility is a key factor used to evaluate various types of *in vivo* implants. The long-term success of any implant depends on how biocompatible it is; those materials that provoke little to no immune response and minimize cytotoxicity in patients yield the best outcomes.[12] In this chapter, we review some of the current regulations for determining the cytotoxicity of materials, specifically those used for bone repair. The most popular such materials are bone grafts, metals (rods, plates and screws), ceramics, and polymers.

Current biocompatibility testing for materials used in bone repair is governed by the U.S. Food and Drug Administration (FDA). According to their standards, all life-supporting biomaterials are considered Class III Devices and must be demonstrated as safe before gaining marketing approval. While most bone repair materials fall into this category, tissue products (bone grafts – xenograft, allograft, and autograft) are regulated under the FDA's Good Tissue Practices and are exempt from toxicity and biocompatibility testing. Therefore, our discussion will omit bone grafts and focus on non-tissue, acellular materials.

Bone is a versatile tissue, so finding a suitable material to repair or replace it is difficult. Our skeleton is made of both cortical and cancellous bone. Cortical bone bears weight. As such, it is very dense, with a porosity of approximately 5-10%. It can undergo compressive stresses in the range of 0.2 – 2942MPa, and it has elastic moduli up to 17GPa.[3, 13, 14] Cancellous bone is less dense, with a porosity of approximately 50-90%. It can undergo compressive stresses in the range of 2 - 15MPa, and it has elastic moduli up to 445MPa.[3, 13] Non-tissue materials such as metals, ceramics, and polymers can mimic these primary structural bone properties; however some materials fail at mimicking the skeleton's other functions.

The skeleton's secondary purpose is metabolic.[15] These metabolic functions, along with the structural functions, are accomplished through maintenance of a rigid skeletal extracellular matrix (ECM). This ECM is regulated in part by hormones, which allow ion release as part of the body's metabolic process, but it is also regulated by bone's three main cell types: osteoblasts, osteocytes, and osteoclasts. Osteoblasts are responsible for the secretion and mineralization of ECM. Osteoclasts are responsible for ECM resorption, allowing for the remodeling of bone. Non-tissue, acellular materials lack the abilities of resorption, secretion, and mineralization.

The problems with current bone repair materials are as follows: Research has identified that metals provide sufficient physical strength but have poor patient site integration.[6] Additionally, metal repairs are unable to grow or undergo remodeling along with the natural physiological environment of the patient.[7] Conversely, ceramics have shown improved site integration but tend to be brittle and lack the necessary mechanical strength.[6, 9] Because neither material fully meets the needs of bone repair, much research has been performed on the suitability of polymers for bone tissue engineering.

Polymers can fill both requirements of strength and sufficient patient integration for eventual replacement. Most recent biomaterial research for bone tissue engineering has focused on biodegradable polymers due to the potential for cell seeding, dynamic scaffold design to match defect shape and size, and biocompatibility.[10]

The FDA requires *in vitro* biocompatibility testing prior to any interactions with an *in vivo* system. The first levels of *in vitro* tests aim to elucidate any potential material cytotoxicity. With this information, material and device developers can safely and effectively move onto the more sophisticated interactions in an *in vivo* system. A well-designed and implemented cytotoxicity testing plan may eliminate the need for wasteful *in vivo* studies, as it will identify any outstanding toxicity issues prior to implantation.[16] However, there are currently no standards for cytotoxicity testing in polymers.

There has been much written about the different types of materials used for bone tissue repair.[8, 10, 17-19] Therefore we will focus in more detail metals, ceramics, and polymers, as well as the current

state of cytotoxicity testing for each.

1.3.2 Metal Alloys / Compounds

Metals were first used as aids in bone repair in the 1890s, and there has since been much development in the utilization and application of metal alloys and compounds for more advanced treatments.[20] Original methodology included the use of rods and pins for stabilization while the body synthesized new bone.[21] However, metals and bone do not fully share mechanical properties, so the application of rods and pins can create newly developed bone that lacks the ability to handle average stress loads via a process called the stress shielding effect.[22] This is commonly seen in hip replacements.[23]

Stainless steel and cobalt-chromium alloys are popular choices for implants. The most commonly used material is 316L austenitic Stainless Steel (316L SS), which is found in a wide array of surgical tools and implanted devices.[24, 25] The primary components of 316L SS are iron, chromium, nickel, magnesium, and molybdenum; the biocompatibility of 316L SS and its components has been demonstrated over many years of implantation *in vivo*.[24] However, the presence of nickel can lead to allergic reactions and sensitization with extended exposure, which is why current research is evaluating the use of stainless steel without nickel.[26] Biocompatibility testing of nickel-free stainless steel has been completed and deemed the material satisfactory, a fact that is additionally supported by its possession of key mechanical properties; Despite these positive factors, the big concern of nickel-free stainless steel is that it is difficult to machine.[24]

Titanium and its alloys are some of the most desirable materials for skeletal applications due to its low elastic modulus, which can result in lower sheer stresses.[27] It is used in many formats, including plates, screws, and rods. Many biocompatibility studies have shown that in addition to titanium's ability to provide sufficient mechanical support for new bone growth, the material is relatively inert, giving it an improved resistance to corrosion.[28] Metal biocompatibility can be linked to its ionization tendency, and

titanium naturally forms a surface oxide, leading to its successful biocompatibility.[29, 30] However this reduced surface interaction with the surrounding tissue can lead to issues with integration.[25] To increase the surface interaction, researchers have been evaluating the use of coatings like hydroxyapatite (HA).[30] Surface modification with chemicals and the addition of matrix proteins are some of the other evaluated methods of improving osseointegration.[31]

Alloys like titanium with 6% aluminum and 4% vanadium (Ti 6% - Al, 4% - V) were once a popular choice in orthopedics. However, aluminum (Al) has been linked to Alzheimer's and vanadium (V) has demonstrated strong cytotoxicity; conclusions about titanium alloys that include these metals are debatable. There is concern about the use of this alloy in areas with high sheer stress, which causes particles to be released from the surface of the device and enter the patient's blood and tissues. However, studies evaluating the effects of pure titanium and aluminum, as well as the effects of titanium and aluminum particles, have shown no cytotoxicity to various types of cells.[28, 32]

Recent research has focused on developing titanium and ceramic compositions as a functionally graded material (FGM) for implantation. Functionally graded materials utilize layering techniques to allow for improved cell growth while maintaining the structural integrity of the material.[31] Research focusing on the addition of hydroxyapatite to titanium demonstrated a non-cytotoxic reaction and an increased bone growth rate compared to materials without hydroxyapatite.[33] Clinical trials have demonstrated the benefits of HA coatings, including improved healing times, increased fixation, and improved bone apposition.[34] Additionally, the inclusion of 2-3% poly(L-lysine) polymers in apatite-based coatings has drawn interest; this organoapatite yields improved tissue integration.[30, 35-37] Basic *in vivo* and *in vitro* testing has been performed on organoapatite, including investigation into the material's impact on osteoinduction and cellular proliferation, but no biocompatibility testing has been published.[36, 38] This idea looks to combine the best of all three materials normally used in bone repair, ceramics, polymers, and metals, which leads us to our discussion of ceramics in bone repair.

1.3.3 Ceramics

Ceramics are the original materials used for repairing bone voids, whether the damage is due to trauma or surgery.[21] They have good biocompatibility and little to no cytotoxicity because they are protein free; the immune response to ceramic implantation is negligent.[9] Although many ceramics are strong they do not provide the requisite mechanical properties due to low fracture strength and poor fatigue resistance (Table 1.3.1).{Li, 1995 #272} One significant characteristic of ceramics for bone tissue engineering, especially calcium phosphates, is that they have been shown to be osteoconductive.[17] Bioactive ceramics display osteoconductive properties and bond to bone even in the absence of fibrous interfaces; these specialized ceramics include calcium phosphates, bioactive glass, and bioactive compounds of glass and ceramic.[17, 34] Calcium phosphates, like biodegradable tricalcium phosphates and hydroxyapatite, are among the most studied ceramic materials.[9]

Table 1.3.1: Ceramics commonly investigated for bone tissue engineering applications.

Ceramic	Chemical Formula	Compressive Strength (MPa)	Reference
Alumina	Al_2O_3	20 – 90 (porous)	{Yoon, 2008 #273}
Hydroxyapatite	$Ca_{10}(PO_4)_6(OH)_2$	< 400	{Rezwan, 2006 #11}
Tricalcium Phosphate	$Ca_3(PO_4)_2$	15	{Galois, 2002 #274}
Zirconia	ZrO_2	136.3	{Mansur, 1998 #276}

Tricalcium phosphate is a powder of monocalcium phosphate monohydrate, alpha tricalcium phosphate, and calcium carbonate—these materials yield a small grain size. The mixture is then added to a sodium phosphate solution, which is applied to the bone defect either through injection or direct applications; after approximately 10 - 15 minutes, it hardens.[21, 39] The most important factor regarding

the use of tricalcium phosphate is that it has been shown to be biocompatible.

Hydroxyapatite (HA) cement is a preparation of calcium phosphate. While it lacks the necessary mechanical strength to be used on its own in load-bearing repairs, it is frequently used in the repair of non-stress loaded traumas, such as cranial defects, and as a component of bone void fillers.[38, 40-45] Because hydroxyapatite degrades very slowly, it is particularly advantageous for use with defects that require long-term treatments. Other advantages come from its similarities in composition and structure to native bone mineral.[40] It provides desirable surface roughness and the ability to adhere directly to bone, which is why it is commonly used in conjunction with degradable polymers.[46] Additionally, it can be used to modify the surface of metal alloys to allow for improved bone adhesion and integration.[26, 27, 34] Some studies have demonstrated the ability of blood vessels to grow into HA after implantation and subsequent degradation.[47] Additional research has delved into combining HA, collagen, and bone morphogenetic proteins for improved bone repair.[48] Biocompatibility testing has been performed with HA to investigate the impact of particle size both *in vivo* and *in vitro*.[49, 50] Overall, hydroxyapatite was found to be safe for implantation.[37, 51]

1.3.4 Polymers

Polymeric materials represent some of the best opportunities for bone tissue repairs. They have the positive characteristics of metal alloys and ceramics without some of the negative characteristics. For example, polymers can provide mechanical strength and may be resorbable, which allows for natural bone ingrowth. Additionally, they can be applied using a variety of methods, including injection and curing using photocrosslinking.[52-54] They may be naturally derived or synthetically made materials.[11] As such, polymer biocompatibility is largely varied due to degradative byproducts, surface chemistry, and the method of the polymer's erosion.[55]

The polymers most commonly used for bone repair include polylactides, poly(methyl methacrylate), poly(urethane), ultra-high molecular weight polyethylene, and poly(propylene

fumarate).[56] All polymers experience degradation over time, whether by exposure to heat, hydrolysis, oxidation, enzymatic reactions, or mechanical stresses.[9] Even so-called non-degradable polymers would be better termed slowly-degrading polymers; their timeline for degradation is significantly longer than their implanted time, but they still ultimately break down.[55] Many polymer byproducts, although innocuous in general, can cause side effects such as lowered pH, which can then damage the local environment. Table 1.3.2 lists some of the most common polymers used for bone tissue applications and their degradation byproducts.

Table 1.3.2: Polymers commonly used in tissue engineering applications.

Polymer	Repeating Unit	Compressive Strength (MPa)	Biodegradation Time (months)	Degradation Products	Bulk Degradation /Surface Erosion	Reference
PDLLA	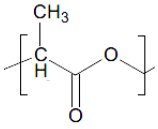	35-150	12-16	Lactic acids	Bulk	[3, 57]
PGA	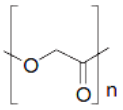	220-405	6-12	Glycolic acid	Bulk	[3, 9, 58, 59]
PLGA	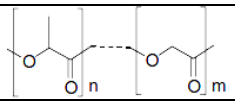	41.2-55.2	1-12	Lactic and glycolic acids	Bulk	[3, 58]
PMMA	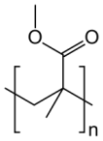	66.3- 77	>> 24 (thermal)	Methyl methracylate	Bulk	[60]
PLLA	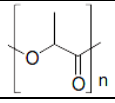	40-120	>24	Lactic acids	Bulk	[3, 11]
PPF	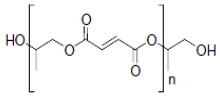	20-70	>24	Fumaric acid, propylene glycol	Bulk	{Fisher, 2002 #47}

1.3.4.1 Polymer Degradation and Byproducts

Degradation rate and byproducts are two major design concerns for scaffolds used in skeletal tissue engineering. Polymers degrade through hydrolysis of ester bonds or through enzymatic degradation

of the polymer backbone.[3] The polymers outlined in Table 1 are biocompatible and produce degradation byproducts that are non-cytotoxic; these acidic degradation products are naturally occurring within the body and pose little biocompatibility risk.[58, 61] However, previous studies have shown that massive degradation and release of these acids may trigger an immune response.[61] Slow degradation combined with an increased ability for the tissue to process or remove the products can counteract this problem.[61] Thus, optimal polymers have few acidic degradation products and degrade slowly to avoid any immune response. Slow degradation also allows for implant strength until tissue regeneration and ingrowth is complete enough to handle weight bearing.[62]

Degradation can occur primarily at the surface or throughout the polymer, depending on the chemical composition of the polymer. Degradation times are affected by molecular weight as well as by the chemical structure.[3] Poly-α-hydroxy esters, PLA, and PGA allow for hydrolytic degradation through de-esterification.[3] Studies have observed that thick segments of polymers will degrade quicker on the inside of the sample than at the surface in a process known as heterogeneous degradation, which is due to neutralization of the carboxylic end groups at the surface of the polymer. The ability of oligomers at the surface to diffuse into the surroundings is also a factor; oligomers inside the polymer do not diffuse as easily. [3] However, with three dimensional (3D) printing, the smallest scaffolds' strut thickness ranges from 50µm-250µm, which is much smaller than the samples used during heterogeneous degradation studies.[63, 64]

Most polymers currently evaluated for 3D printed scaffolds degrade via bulk degradation (Table 1). Bulk degradation can cause issues, including scaffold failure.[3] However, in skeletal tissue engineering, bulk degradation is not seen as a significant issue because of the long degradation times and the rate of bone growth within the scaffold. Bone tissue has shown to grow into the space provided by bulk degradation; this is desirable for the complete resorption and replacement of these scaffolds.[65]

1.3.4.1.1 Poly(Methyl Methacrylate) (PMMA)

Poly (methyl methacrylate) (PMMA) has been commonly used as a main component of bone cements for more than 30 years.[66] Its ability to be polymerized *in situ* and delivered via injection makes it an ideal candidate for use multiple applications including spinal fusion surgeries, craniofacial repair and as a fixation method to anchor prosthesis to the native bone in arthroplasties.[66-68] As PMMA is used frequently as a long term repair of a defect or as a fixation method, degradation has not been extensively studied. Many studies have evaluated one of the main defects of PMMA, the lack of mechanical strength, subsequent crack formation and eventual loosening of the cemented prosthesis.[69] Much work has been focused on developing PMMA-based composite materials to improve the mechanical strength as PMMA alone has a compressive strength below that of bone.[60, 68] The addition of materials bioactive ceramics, biodegradable polymers, and polysaccharides allows for the reduction in exothermic reaction, cement shrinkage after polymerization, and improved osseointegration.[14, 70, 71] All of these factors have been shown to improve the use of PMMA *in vivo*.[68] However significant concerns of cytotoxicity have been documented both due to increased formation of fibrous tissue where the body is exposed to the PMMA and exposure to the toxic monomer, methylmethacrylate, during polymerization.[66, 72] Since the formation of PMMA *in situ* is exothermic, many studies have identified that the localized increase in temperature may be one of the contributing factors to necrosis at the site of use.[66, 73, 74]

1.3.4.1.2 Saturated Aliphatic Polyesters (PLA, PGA)

Poly(lactic acid) (PLA) and its three forms (PLLA, PDLA, and PDLLA), along with poly(glycolic acid) (PGA) and its co-polymer poly(lactic-*co*-glycolic acid), degrade through hydrolysis and produce lactic and glycolic acid as products.[3] Physical characteristics and degradation rates vary over the range of molecular weights for these polymers; generally, PLA degrades slower than PGA (Table 1).

Recent SLA fabrication has created gyroid pore formations using PDLLA-NVP as a resin to

enhance osteoblast proliferation.[75] Additionally, pre-osteoblasts were able to be seeded and proliferate on PDLLA-NVP scaffolds.[57] Although PDLLA has a high glass transition temperature, it may be combined with a diluent for use with SLA.[75] This work illustrates the idea that saturated aliphatic polyesters, like PLA and PGA, may be feasible for skeletal tissue engineering if they are made into strong, slowly degrading scaffolds seeded with osteoblasts.

1.3.4.1.3 Poly(Propylene Fumarate) PPF

Poly(propylene fumarate) (PPF) is an absorbable aliphatic polyester polymer that has been well characterized for use in bone tissue engineering scaffolds.[52, 76-79] Prior work has shown that the use of diethyl fumarate (DEF), one reagent used to make PPF, within poly(propylene fumarate) scaffolds increases crosslinking density and stiffness; adding the precursor DEF also lowers the viscosity enough for use in rapid prototyping.[52] Other studies have demonstrated that PPF degradability depends on molecular weight and crosslinking density.[80, 81]

PPF scaffolds were originally photocrosslinked using only BAPO, however this formulation was found to be unsuccessful for use in 3D printing. The polymer resin of PPF, DEF, and BAPO required the use of a dye to sequester light, thus reducing any crosslinking outside of the desired area. Previous work suggested the addition of titanium dioxide (TiO2) to control the depth of polymerization and therefore the accuracy of the scaffold layer thickness[1]; plate and post scaffolds have been successfully fabricated with PPF, DEF, BAPO, and TiO_2 using cDLP technology in the envisionTEC Perfactory® additive manufacturing device (Figure 3.1). Although this work has been promising, current research has demonstrated even higher accuracy during scaffold fabrication by adding additional dyes such as 2-hydroxy-4-methoxybenzophenone (HMB) along with TiO2.

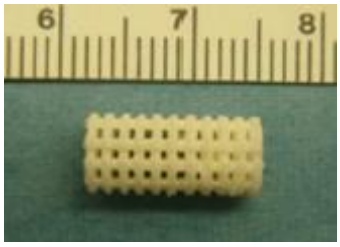

Figure 1.3.1: Photograph of fabricated plate and post PPF scaffold.[1]

Previous studies have evaluated the use of PPF with SLA to produce scaffolds with controlled pore size and wall thickness.[64, 82-84] Many studies have looked at using propylene fumarate as a

copolymer because it is a linear unsaturated molecule, which would allow for the addition of copolymers along the polymer backbone.[85-87] These properties suggest the use of PPF in SLA fabricated scaffolds for its osteoblastic properties and slow degradation time, combined with quickly degrading co-polymers used for the delivery of additional growth factors or genes.

1.3.4.1.4 Biocompatibility Impact of Other Materials Used for Crosslinking

Polymer biocompatibility is not solely dependent on the parameters of the polymer itself; it is also dependent on the materials used to prepare crosslinked polymers: the initiator, photoinitiator, and dye. Many photoinitiator and dye combinations currently used in the creation of 3D printed scaffolds are known to be toxic.[1] However, research has focused on the development of biocompatible photoinitiator and dye packages, such as oxybenzone and titanium dioxide (TiO_2).[1] Oxybenzone (2-hydroxy-4-methoxybenzophenone), or HMB, is used commercially as an ultraviolet absorber in sunscreen.[88] Many studies have evaluated the toxicity and metabolic pathways of HMB, and it is considered safe for topical application[88-91]; these studies have also determined that HMB is not genotoxic *in vivo.[89]* TiO_2 is commonly used as a food and drug coloring agent, as well as an active ingredient in sunscreen.[1] The rutile form, with crystals 250 – 305nm in size, is used as an ultraviolet attenuator.[1] The toxicity of TiO_2 as a topical agent in sunscreens has been well characterized; it has been deemed nontoxic.[92] Many studies have investigated the toxicity of TiO_2 for non-topical applications and have found it to have low toxicity levels even at intravenous doses of 5mg/kg of patient weight.[92, 93] However, at much greater doses (e.g. 2592mg/kg), acute toxicity was seen in mice that had intraperitoneal injections of nanoparticle TiO_2.[73]

1.3.5 Toxicity Evaluation Methods

To evaluate a material's suitability for patient implantation, biocompatibility must be evaluated. Three ascending levels of testing are required for this evaluation: first, toxicology studies are performed

in vitro and in animals; second is animal *in vivo* testing with the material used as designed; and finally, human clinical trials.[16] Currently, ISO Standard 10993 represents the framework of tests recommended by the FDA for assuring the safety of a material prior to approval.[94]

1.3.5.1 ISO Standard 10993

The FDA's guidance document is titled "Use of International Standard ISO 10993, 'Biological Evaluation of Medical Devices' – Part 1: Evaluation and Testing." This standard provides guidelines for all levels of evaluation, from the basic level of cytotoxicity to systemic toxicity from implantation.

Specifically, ISO Standard 10993-5 addresses "Tests for In Vitro Cytotoxicity." The goal of the standard is to "determine the biological response of mammalian cells *in vitro* using appropriate biological parameters."[95] Overall, it provides general guidelines to ensure appropriateness of test conditions and evaluation. These guidelines aim to remove any unnecessary variables from testing, and they include recommendations for cell lines, sterilizing and aseptic techniques, solvent choices, statistical replications, and appropriate positive, negative, and blank controls. The standard also details a three-pronged approach for the evaluation of potential cytotoxicity of medical devices: extract testing, direct contact testing, and indirect contact testing.

Extract testing evaluates the cytotoxicity of leachable components from the medical device. The testing occurs after the medical device is incubated for at least 24 hours in a non-cytotoxic solvent, e.g. cell culture media with or without serum. The incubation temperature can range from physiological to autoclave sterilizing conditions to best mimic the environment that the medical device will encounter prior to exposure to the patient. Specifically, the standard states, "extraction conditions should attempt to simulate or exaggerate the conditions of clinical use so as to determine the potential toxicological hazard, without causing significant changes in the test material such as fusion, melting or alteration of the chemical structure."[95] The extract and media solution is then used to replace the media used to culture subconfluent cells, 80% confluent, for at least 24 hours. After 24 hours, any negative impact on the cells

is evaluated and compared to negative, positive, and blank media controls per the guidelines set in the standard.

Indirect contact testing is used to qualitatively evaluate cytotoxicity by exposing cells to the material after diffusing through an agar layer or through a filter. This method is helpful, like extract testing, for evaluating materials which may have a greater cytotoxic load. Diffusion allows for a gradual exposure to the material compared to direct contact testing, which does not allow for graded evaluation of the material's impact. The method uses cells that are grown to subconfluency, which are then covered by a layer of agar mixed with growth media, which is allowed to solidify. Then the engineered material is placed on top of the agar and allowed to incubate for 24 to 72 hours, at which point the sample is removed and the cells are evaluated for signs of toxicity. Alternatively, cells can be grown to subconfluency on a filter, which is then transferred, cell side down, on to a layer of solidified agar. The material is then placed on the acellular side of the filter and incubated for 2 h ± 10 minutes. Cells are evaluated for signs of toxicity per table 1.

Direct contact testing, as implied by its name, evaluates the cytotoxicity of the material when cells are in direct contact. The cell lines used for the test may be grown to subconfluency on top of the material, or the material may be placed on top of the cells after they've grown. The media is replaced and the culture is incubated for at least 24 hours. Cytotoxic effects are determined per the guidelines set in the standard.

ISO Standard 10993 also covers other areas of biocompatibility testing. Systemic toxicity and pyrogenicity testing is governed under ISO Standard 10993-11, "Test for Systemic Toxicity." ISO 10993-6 provides the testing framework for implanted materials through the "Tests for Local Effects after Transplantation."[95]

Previous studies have tested the byproducts of polymer degradation[96] but there has been little focus on developing a method to test the toxicity of the polymer at different points during degradation. As discussed previously, the current testing scheme for implantable materials focuses on evaluating the

cytotoxicity of the leachable components during the first 24-48 hours of implantation. However, this testing scheme is most valuable for durable polymers; those that do not experience significant degradation during implantation. For polymers that are implanted with the express purpose of degradation then it would be best to develop a testing scheme that evaluates both the leachable components and degradation byproducts during the lifespan of the degrading polymer. Additionally tests to evaluate biodegradability have been well documented and implemented but very few studies look at the biocompatibility of the degraded polymer.[97]

1.3.6 Conclusion and Future Directions

With the increased use of biodegradable polymers in tissue engineering and medical device applications there is a need for standards to evaluate the cellular response to the degradation byproducts. Currently *in vitro* testing of biodegradable polymers is evaluated after 24 hours. New standards could be developed to investigate the impact of degradation products during long term implantations. Ideally these standards would initially investigate the impact of degradation *in vitro* as to improve the polymers during the initial stages of research. These new standards could expand the use of extract testing to look at the release of potentially cytotoxic byproducts during long term degradation. Evaluation of the systemic impact of degradation by products would be beneficial to better predict the response *in vivo*. Additionally if cytotoxicity testing can better predict *in vivo* cellular response then testing could be performed at the initial round of biomaterial development so that time, materials and other resources are not wasted on materials that are cytotoxic.

1.4 Background: Signal Expression of hMSCs during Differentiation[1]

1.4.1 Introduction

Current trends in tissue engineering focus on the impact of exogenous and endogenous signals on cells seeded in scaffolds. To fully understand the potential impact of these signaling molecules we must first review their signal expression pathways. In this chapter we focus on two of the most common cells used in skeletal tissue engineering osteoblasts and chondrocytes. We will discuss the basic biology of the skeletal system and investigate the impact of the different signaling molecules such as hormones, cytokines, growth factors, and the mechanotransduction signaling pathway on cell phenotype and gene expression.

In tissue engineering the implementation of a successful tissue scaffold is dependent on three factors, an appropriate cell type, developing a scaffold to mimic the surrounding tissue, and then using cell signaling to drive cells to express the correct phenotype and genes. Through understanding of the signals that impact osteoblast and chondrocyte functions we can improve *in vivo* use of engineered tissue scaffolds.

1.4.2 Biology of Osteoblasts

1.4.2.1 Bone Extracellular Matrix

The skeleton's primary purpose is to provide structural support however its secondary purpose is metabolic.[15] These purposes are accomplished through maintenance of a rigid skeletal extracellular matrix (ECM) regulated for the release of ions through hormones. Bone is made of three cells, osteoblasts, osteocytes and osteoclasts, and the ECM.

---

[1]Adapted from: MO Wang and JP Fisher. "Signal Expression" Ch 7. In: The Biomedical Engineering Handbook, 4th Ed., (Fisher, Mikos eds.) CRC Press, Taylor & Francis, London. (2013)

Table 1.4.1: List of Abbreviations

Akt	v-akt murine thymoma viral oncogene homolog
ALP	alkaline phosphatase
BAD	BCL2-associated agonist of cell death
BAX	BCL2-associated X protein
BCL-2	B-cell CLL/lymphoma 2
BMP	bone morphogenic protein
CD44	CD44 molecule (Indian blood group)
c-fos	FBJ osteosarcoma oncogene
ECM	extracellular matrix
ERK	extracellular signal-regulated kinase
FAC	focal adhesion complex
FADD	fas-activated death domain protein
FAK	focal adhesion kinase
Fas	TNF receptor superfamily, member 6
FGF	fibroblastic growth factor
GAGs	glycosaminoglycan
GH	growth hormone
gp130	interleukin 6 signal transducer (gp130, oncostatin M receptor)
Grb2	growth factor receptor-binding protein 2
Herp2	homocysteine-responsive endoplasmic reticulum-resident ubiquitin-like domain member 2 protein
HesR-1	hairy and enhancer of split related-1
HeyI	hairy/enhancer-of-split related with YRPW motif 1
IGF	insulin-like growth factor
IGF-1R	insulin-like growth factor-1 receptor
IGFBP	insulin-like growth factor binding protein
IL	interleukin
IL-1RA	interleukin-1 receptor antagonist
IL-1RAP	interleukin-1 receptor associated protein
IL-6R	interleukin-6 receptor
IL-R	interleukin receptor
IRAK	interleukin-1 receptor activate kinase
IRS	insulin receptor substrate
JNK	c-Jun N-terminal kinases
JunB	jun B proto-oncogene
Lrp-5	low density lipoprotein receptor-related protein 5
MAPK	mitogen-activated protein (MAP) kinases
M-CSF	macrophage colony-stimulating factor

MEK	map erk kinase
MGP	matrix Gla protein
MMP	matrix metalloproteinase
NF-κB	nuclear transcription factor - kappaB
NO	nitric oxide
NOS2	nitric oxide synthase type II
OCN	osteonectin
PDGFR	platelet-derived growth factor receptor
PGDF	platelet-derived growth factor
PGE2	prostaglandin E2
PI3K	phosphatidylinositol 3-kinases
PK	protein kinase
PTH	parathyroid hormone
Raf	proto-oncogene serine/threonine-protein kinase
Ras	rat sarcoma guanine triphosphatase
Rel	C-Rel proto-oncogene protein
Runx2	runt-related transcription factor 2
Shc	src homology 2 domain containing transforming protein 1
sIL-6R	soluble interleukin-6 receptor
Smad	mothers against decapentaplegic homolog
Smurfs	smad ubiquitin regulatory factors
Sox9	sex-determining region Y-related gene
Src	sarcoma
STAT	signal transducer and activator of transcription
Tcf7	transcription factor 7
TGF	transforming growth factor
TIMP	tissue inhibitor of metalloproteinase
TNF	tumor necrosis factor
TRADD	tumor necrosis factor receptor-associated death domain protein
TRAF	tumor necrosis factor receptor-associated factor
VEGF	vascular endothelial growth factor
g1	vegetalising factor-1
Wnt	wingless-type MMTV integration site family

Osteoblasts are responsible for the secretion and mineralization of ECM. Osteocytes are mature osteoblasts encased within the ECM. Osteoclasts are responsible for ECM resorption allowing for the remodeling of bone.

The extracellular matrix consists mainly, greater than 90%, of type 1 collagen.[98] The non-collagenous components of the ECM include γ -carboxyglutamic acid-containing proteins, glycoproteins, enzymes, and sialoproteins.[98] The γ-carboxyglutamic acid-containing proteins in the ECM are osteonectin (OCN) and matrix Gla protein (MGP). OCN is only found in mineralized tissues and is one of the most abundant non-collagen proteins in the ECM.[98] MGP is structurally similar to OCN but is found in many tissues throughout the body.[98] The sialoproteins osteopontin and bone sialoprotein are RGD-containing matrix proteins within in the SIBLING family. The enzymes in bone ECM are alkaline phosphatase and matrix metalloproteinases. Matrix metalloproteinases (MMP) all have the ability to digest ECM facilitating the movement of cells and therefore moderating the resorption and remodeling of bone. MMPs are used as a metric of bone homeostasis. Fibronectin, osteonectin, thrombospondin and proteoglycans are the glycoproteins found in the ECM.[98]

Osteoblasts are responsible for the secretion and mineralization of the ECM. Osteoblasts differentiate from pluripotent mesenchymal cells through four stages. Each stage has a distinct phenotype with the expression of different bone matrix proteins. The first stage consists of the differentiation into an osteoprogenitor cell. In this stage bone morphogenic protein (BMP)-2 and wingless-type MMTV integration site family (Wnt) signaling is up regulated for the commitment to the osteoblastic cell line. The second stage is the transition from an osteoprogenitor to a pre-osteoblast cell. PTH helps to commit the osteoprogenitor this process; this stage is identified by the up regulation of alkaline phosphatase (ALP), runt-related transcription factor 2 (Runx2), and collagen Ia gene expression.[99, 100] The third stage, the mature osteoblast is identified by the up regulation of ALP, collagen Ia, OCN, Runx2, Osterix, and other genes.[101] We will focus on the signaling impact of mature osteoblasts, the main producer of ECM proteins and the subsequent mineralization of the ECM.[100, 101] The fourth stage occurs with the terminal differentiation of the mature osteoblast into an osteocyte and elevated levels of apoptosis.[100, 101] OCN, Runx2 and low density lipoprotein receptor-related protein 5 (Lrp-5) are the main genes expressed in this stage.[100]

1.4.3 Biology of Chondrocytes

1.4.3.1 Cartilage ECM

Articular cartilage is a heterogeneous avascular, aneural and alymphatic tissue consisting of chondrocytes and its surrounding ECM.[102-104] Its purpose is to act as a low-friction, material that is resistant to compressive loading. The ECM is divided into four zones, superficial, middle, deep and calcified.[103, 105] The ECM consists mainly of collagen, proteoglycans, and noncollagenous proteins.[106] Unlike bone ECM, chondrocyte ECM is composed of 90% type II collagen. Other collagen types present are collagen types VI, IX, X, and XI.[106, 107] The remaining ECM is composed of proteoglycans, aggrecan, glycosaminoglycan (GAGs), hyaluronic acid, decorin, biglycan, and perlecan.[108] Proteoglycans are heavily glycosylated, consisting of a long linear chain of carbohydrate polymers that are covalently bonded to glycosaminoglycan chains.[98] GAGs are negatively charged allowing them to swell with water so when depressed they are able to dispel the water, compress and reform when the compression subsides.[109] Collagen fibers create a mesh of these molecules by binding decorin and biglycan to collagen fibers and then trapping proteoglycans and GAGs within the network.[105, 110] This collagen meshwork works to provide great tensile strength and the ability to remain intact under compressive forces.[105, 106, 110]

Though chondrocytes only compose ~5% of the total volume and are sparsely distributed throughout the tissue they are responsible for synthesizing and maintaining cartilage homeostasis.[102, 107, 111] Chondrocytes are spherical in morphology and contained within a pericellular matrix, made of type VI collagen and biglycan.[106, 108] Type VI collagen fibers interact with hyaluronic acid, biglycan, and decorin to provide the framework for ECM attachment and the transmission of mechanical stimuli to the cell.[106, 108]

Chondrocytes also differentiate from pluripotent mesenchymal cells to either hypertrophic chondrocytes (transient cartilage) or to chondrocytes (permanent articular cartilage).[112, 113] Transient

cartilage refers to the cartilage that is found during chondrogenesis in endochondral ossification and growth plate development.[112, 113] We will focus on the terminal differentiation into chondrocytes located in permanent articular cartilage. The differentiation of the mesenchymal cell into a chondrocyte is marked by the up regulation of sex-determining region Y-related gene (Sox9) and the secretion of ECM components type IIb collagen and aggrecan and is up-regulated by the addition of transforming growth factor (TGF)-β1 and BMP-7.[112-114]

1.4.4 Signaling Pathway Overview

Intracellular cell signaling occurs through the translation of extracellular mechanical or chemical stimuli into a cellular response. The signaling pathways from these translations occur through the same general process. An extracellular signal, such as a cytokine, growth factor or hormone, is transmitted through the cellular membrane into the cytoplasm. Once inside the cell it may either continue to the nucleus via second messengers, or interact within the intracellular region with other cell components (e.g. the cytoskeleton) leading to the desired cellular effect whether it is a change in gene expression, phenotype, or metabolism. The cell signaling pathway studies referenced in this chapter used bovine, murine, human and other mammalian derived cells. Since this is an overview of the major cell signaling pathways we have not differentiated between each mammalian cell type.

Autocrine signaling occurs when signaling molecules released from a cell bind to receptors located on the same cell. Similarly paracrine signaling refers to signaling molecules that bind to receptors located on neighboring cells. Endocrine signal occurs when systemically circulating signaling molecules (e.g. hormones) bind to receptors located in cells external to their place of production.

Cytokines, growth factors and hormones are some of the extracellular signaling molecules that initiate signaling pathways. Cytokines (e.g. interleukins, interferons) are primarily used for maintaining cell homeostasis and the body's defensive pathways. Growth factors, closely related to cytokines, are primarily used in the regulation of cell growth and proliferation such as TGF-β superfamily and insulin-

like growth factor (IGF). Hormones (e.g. parathyroid hormone, growth hormone) interact with cells through endocrine signaling.

Signaling pathways occur through the attachment of an extracellular signal, a ligand, to a cell receptor protein either spanning or extending from the plasma membrane of the cell. Receptor proteins are most commonly transmembrane, structurally consisting of three segments, extracellular, intracellular and a hydrophobic segment located within the plasma membrane. One notable exception is for hormone signaling which mainly occurs through intracellular receptors. Once the ligand binds to the receptor the intracellular protein has a conformational change initiating the signal cascade through activation of proteins or other second messengers (e.g. kinase, phosphatase, calcium). Since multiple signals may lead to the same phenotypic response or to different outcomes it can cause a whole tissue response from the same signaling molecules interacting with different receptors and cells.

Once the desired cellular effect has occurred the ligand may be released from the receptor, then either degrade or bind with another receptor. Receptor and ligand complexes may also be internalized through clathrin-mediated endocytosis. Once internalized the complexes may be recycled back to the cell surface via early endosomes or degraded in late stage endosomes. Alternatively complexes may be degraded through endocytosis and transportation to the proteasome by calveolin-positive vesicles. For example Transforming growth factor beta (TGF-β) receptors are internalized through both the clathrin-mediated and caveolar pathways.[115, 116] Intracellularly, after second messengers complete their role in the signaling cascade they may be degraded through ubiquitination, observe a conformational change to become inactive permanently or inactive until later activation.

Cell homeostasis is maintained through complex feedback loops and the balance of anabolic and catabolic growth factors and cytokines.[117] Anabolic growth factors and cytokines work to maintain homeostasis by increasing the expression of gene for increased cell proliferation and for the proteins that make up the ECM. In contrast, catabolic growth factors and cytokines work to change gene expression levels to produce proteins that work to degrade the proteins that are components of the ECM.

Since osteoblasts and chondrocytes share the much of the same environment, the skeletal system, they are exposed to some of the same signaling molecules. However the same signaling molecules may impact osteoblasts and chondrocytes differently. We will look in depth at some shared cytokines and growth factors such as TGF-β1, IGF-1, BMP-2, BMP-7, tissue necrosis factor (TNF)-α and interleukin (IL) -1.

1.4.5 Anabolic Growth Factors/Cytokines

1.4.5.1 Insulin-like Growth Factor

IGF-1 is considered to be the main anabolic factor for chondrocyte growth, proliferation, and survival.[104, 111, 118] It is structurally similar to insulin and consists of a single chain of 70 amino acids, with a molecular weight of approximately 7.5kDa.[119] IGF functions as an endocrine, autocrine and paracrine growth factor.[118, 120] As an endocrine growth factor it is circulated systemically after production in liver but it also may act through autocrine or paracrine signaling as in osteoblasts and chondrocytes when it is synthesized and incorporated into the ECM. [104, 121] To maintain stability in the ECM IGF-1 is bound to an antagonist, the IGFBP.[121]

4.5.1.1 IGF Signaling Pathway

IGF-1 signaling is initiated through the ligand binding of insulin-like growth factor-1 receptor (IGF-1R), a transmembrane glycoprotein tetramer. IGF-1R is a tyrosine kinase receptor with its two α and two β subunits connect by disulfide bonds.[102, 120] For IGF-1 to bind to its receptor it must first cleave the antagonist insulin-like growth factor binding protein (IGFBP). There are 6 known IGFBPs that may bind to both IGF-1 and IGF-2.[119, 122] IGFBPs are used for IGF transport and increasing IGF stability and therefore their half-lives.[121] After cleavage, ligand binding occurs with the extracellular α subunit IGF-1R, then the β subunit, which spans the membrane, autophosphorylates its intracellular tyrosine phosphorylation site.[123] Once phosphorylated, the major substrates, insulin receptor substrate (IRS)-1, IRS-2, and src homology 2 domain containing transforming protein 1 (Shc) may bind, become

phosphorylated, and then begin the signaling pathways [119, 124, 125] (Figure 4.1). IRS-1 initiates the phosphatidylinositol 3-kinases /v-akt murine thymoma viral oncogene homolog (PI3K/Akt) pathway mediating the antiapoptotic effects of IGF1R by phosphorylating and therefore inactivating BCL2-associated agonist of cell death (BAD).[124] Concomitantly the rat sarcoma guanine triphosphatase/ mitogen-activated protein kinases (Ras/MAPK) pathway is initiated by the IRS-2 pathway and by the phosphorylation of Shc. The Ras/MAPK pathway leads to increased cell proliferation, and possibly the mediation of oxidative stress cell damage and apoptosis.[102, 124]

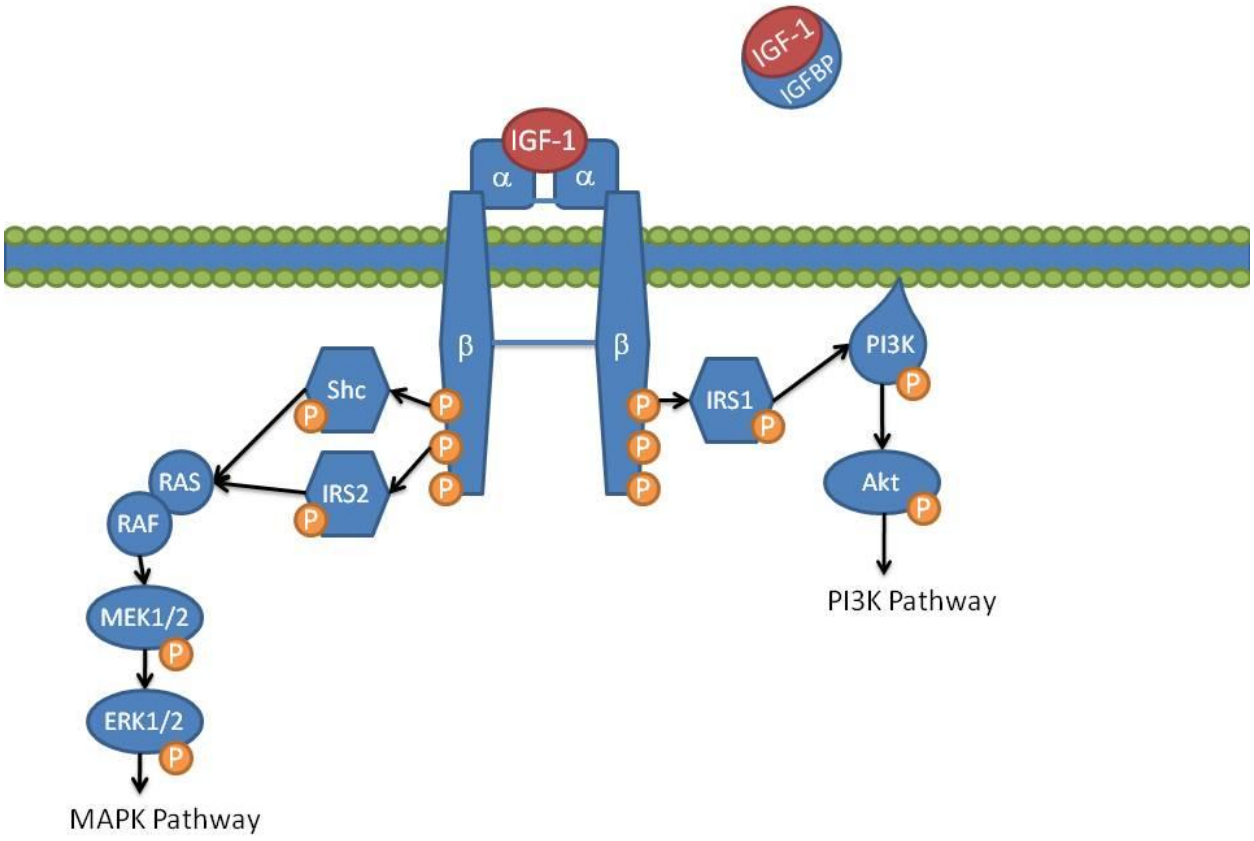

Figure 1.4.1: IGF-1 signaling pathway [124], To initiate the IGF-1 signaling pathway first the antagonist IGFBR must be cleaved from the ligand. After proteolysis, the IGF-1 ligand may bind with its receptor, IGF-1R to initiate auto phosphorylation. Once IGF-1R is phosphorylated it subsequently initiates a phosphorylation chain of Shc and IRS1/2 to activate the MAPK and PI3K pathways.

1.4.5.1.2 IGF-1 in Osteoblast and Chondrocytes

Of all the growth factors osteoblasts produce, IGF-1 and IGF-II are the most abundant.[121] Although osteoblasts are capable of producing all six IGFBR, primarily in osteoblasts IGF binds with IGFBP-3, -4, -5.[120, 122] Of which IGFBPs -4 and -5 are the most abundant within the ECM.[121] Of the six IGFBP -1, -2, -4, -6 are known to inhibit osteoblast function while IGFBP -3 stimulates.[121] IGFBP-5 is the most controversial as it both inhibits and stimulates IGF interaction with osteoblasts.[121, 122] IGFBR concentrations may differ depending on the levels of IGF-1 through autocrine and paracrine signaling.[120] In order to access IGF-1 osteoblasts secrete MMP and serine proteases which cleave IGFBPs [120] to free IGF-1 for ligand binding. Osteoblast apoptosis is mediated through the IGF-1 activation of the PI3K/Akt pathway.[124] Additionally osteoblast proliferation is regulated through the activation of the extracellular signal-regulated kinase/ mitogen-activated protein (MAP) kinases (ERK/MAPK) pathway. [124] In osteoblasts IGF-1 is known to be under the control of PTH, exposure to PTH causes osteoblasts to express IGF-1.[120] In turn, IGF-1 has shown to stimulate osteoblast proliferation and ECM production.[126]

In chondrocytes IGF-1 stimulates an increase of proteoglycans, aggrecan, hyaluronan and collagen synthesis.[104, 118] IGF-1 initiates proteoglycan production by activating both the PI3K and ERK/MAPK pathways; however, only the PI3K pathway is required for the synthesis.[118, 127] Also through the activation of the PI3K pathway chondrocytes have been shown to express type II collagen.[102] IGF-1 has been shown to inhibit ECM degradation by decreasing the production of MMP-13, one of the major factors in ECM degradation.[109, 127] Reduction of MMP production occurs through the activation of the ERK/MAPK pathway.[127, 128] Also, IGF-1 in chondrocytes upregulates IL-1RII, a decoy receptor for the cytokine IL-1, protecting the cell from the catabolic IL-1 signaling pathway. [129] Interestingly, IGF-1 in chondrocytes has shown to not activate either the c-Jun N-terminal kinases (JNK) or p38 proteins as seen in other cell types.[128] IGF-1 also is able to inhibit apoptosis that is normally caused through the TNF receptor superfamily, member 6 (Fas) antibody activation creating an

imbalance in BCL2-associated X protein/ B-cell CCL/lymphoma 2 (BAX/BCL-2) concentration levels, as well as a decrease of Focal adhesion kinase (FAK) and integrin expression.[130] As discussed previously IGF-1 increases integrin expression and therefore increases the number of mechanoreceptors available which may increase MAPK pathway activation.[102, 124]

1.4.5.2 Transforming Growth Factor β Superfamily

Among the many signaling molecules that effect osteoblasts and chondrocytes, the TGF-β superfamily consists of one of the largest range of impact factors. The TGF-β superfamily can regulate cell differentiation, proliferation, maintenance and apoptosis.[100, 131-133] The TGF-β superfamily consists of a set of structurally conserved dimeric proteins held in place through hydrophobic interactions. TGF- β1, TGF- β2, TGF- β3 isoforms, bone morphogenetic proteins (BMPs), vegetalising factor-1 (Vg1), and Activin are some of the proteins within the superfamily.[132, 133]

4.5.2.1 TGF-β Signaling Pathway

The TGF-β superfamily cell signaling pathways are well characterized (Figure 4.2). Cell signaling occurs through association with two transmembrane serine/threonine glycoprotein kinase receptors, type I (TβR-I) and type II (TβR-II).[134] Both receptors are dimers; upon ligand binding to the TβR-II, TβR-I is recruited to make a heterotrimeric complex. The dormant TβR-I is activated through phosphorylation by the constitutively phosphorylated active TβR-II. After phosphorylation TβR-I most commonly initiates the signaling pathway by phosphorylating the mothers against decapentaplegic homolog (Smad) receptor protein, or less commonly via the Non-Smad pathway.[134-137]

Smads, or mothers against decapentaplegic homologs, are made of three subclasses: receptor regulated (R)-, inhibitory (I)-, and common mediator (Co)- Smads. R-Smads, Smad1, Smad2, Smad3, Smad5, Smad8, bind with the activated TβR-I. Once phosphorylated R-Smads bind with Co-Smad, Smad4, and enter the nucleus to regulate gene transcription. I-Smads, Smad-6 and Smad-7, regulate gene

expression through inhibiting the interaction of TβR-I and R-Smads.[138, 139]

The Smad pathway regulates the transcription of specific genes through three methods. First is the direct binding of an R-Smad- Smad4 complex to the DNA. The second method occurs through the interaction with other protein receptors to activate transcription. Additionally R-Smad-Smad4 complexes may effect gene transcription through binding with either genes co-activators or co-repressors.[140]

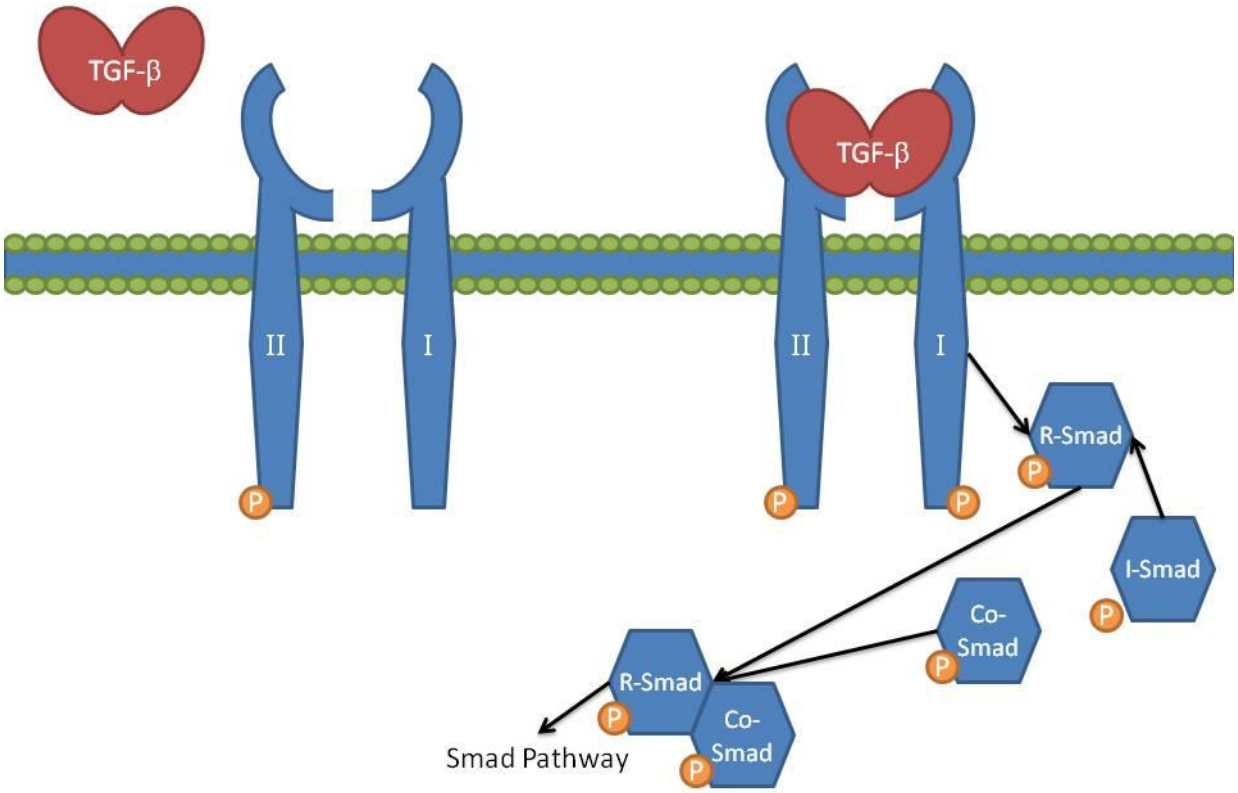

Figure 1.4.2: TGF-β signaling pathway. When the ligand, TGF- β, binds to its receptor the signaling pathway is activated. Once ligand binding occurs the constitutively phosphorylated T β R-II receptor phosphorylates T β R-I. This initiates the phosphorylation of R-Smads, and the subsequent binding with Co-Smads to activate the Smad pathway. *Adapted from Izzi and Attisano [141].*

1.4.5.2.2 TGF-β1

Transforming growth factor β1, TGF-β1, is the most abundant member of the TGF-β superfamily.[134] It impacts cell proliferation, differentiation and apoptosis of both chondrocytes and

osteoblasts.[135] TGF-β1 signaling pathway occurs through Smad activation as well as through non-Smad pathways including activation of the ERK, JNK, and p38 MAPK pathways.[137, 142] TGF-β is found in the ECM surrounding osteoblasts as well as in chondrocytes.

In osteoblasts TGF-β1 blocks apoptosis and allows for the transdifferentiation into osteocytes. TGF-β1 impacts osteoblasts during early differentiation by increasing the expression of Runx2, along with BMP, however; during late differentiation and osteoblast maturation it suppresses Runx2, collagen 1, ALP and osteocalcin production. Additionally as the osteoblasts mature it has been demonstrated that all receptors are down regulated therefore it is hypothesized that mature osteoblasts are less sensitive to TGF-β1 and its inhibition of matrix mineralization.[134] During late differentiation osteoblasts express collagen 3 (MMP13) which leads to the degradation of ECM, signaling the transition for osteoclast resorption.[135] Studies have shown that the increased collagen 3 expression caused by TGF-β1 signaling occurs optimally through activation of both the MAPK and the Smad pathways.[135] TGF-β1 also down regulates ALP, osteocalcin, collagen I and BMP-2 mRNA expression.[143]

In chondrocytes the impact of TGF-β1 on ECM production has conflicting reviews. [104, 144, 145] It has been shown to both stimulate the synthesis of ECM and decrease proteoglycan production.[104, 142] Specifically chondrocytes in the presence of TGF-β expresses increased levels of aggrecan.[146] Additionally TGF-β1 has been shown to prevent chondrocyte apoptosis when stimulated with TNF-α.[147] TGF-β1 plays a main roles in ECM maintenance by reducing ECM degrading enzymes such as collagenase and MMP inhibitors.[148, 149] Due to the success of prior individual studies using TGF-β1 or IGF-1 to improve chondrocyte growth, proliferation and ECM production, current work focuses on combining these growth factors and has shown increased collagen and proteoglycan synthesis.[103, 104, 150]

1.4.5.2.3 BMP

One of the best characterized growth factor of the TGF-β superfamily for use with osteoblasts is

BMPs. Since their identification in the 1960s there have been over 30 BMP family members identified and 20 of which have been well characterized.[151-153] Structurally BMPs are a dimeric protein with seven cystine amino acid residues, six of which form an intrachain disulfide bonds and the seventh is used to form dimers through an interchain disulfide bond.[154]

Since BMPs are part of the TGF-β superfamily they follow the same cell signaling pathway, through binding of serine/threonine kinase receptors which initiate the Smad and non-Smad pathways.[154] Whereas the TGF-βs use Smad2 and Smad3 for signal transduction, the BMP family uses Smad1, Smad5 and Smad8 as R-Smads. As in TGF-β signaling, Smad4 is the Co-Smad and Smad6/7 are I-Smads. BMP signaling may be inhibited five ways, the nonsignaling of pseudoreceptors, intracellularly through I-Smads, ubiquitination caused by smad ubiquitin regulatory factors (Smurfs), and antagonist binding of R-Smads, and extracellularly through antagonist binding of BMP.[138, 155] Some of the BMP antagonists are noggin, gremlin, sclerostin.[155, 156]

1.4.5.2.3.1 BMP-2 and BMP-7

The effects of BMP-2 and BMP-7 on osteoblast differentiation, growth, proliferation and apoptosis are well documented, and currently are used for clinical applications in the healing bone defects.[131, 154] Of the BMP family, BMP-2, is known as a main factor in osteoblast homeostasis and BMP-7, is regarded as a main factor in chondrocyte function. [102]

BMP-2 can be a positive or a negative factor in osteoblast homeostasis. BMP-2 has been shown to promote osteoblast apoptosis as well as impact Notch and Wnt signaling through the regulation of hairy/enhancer-of-split related with YRPW motif 1 (*HeyI*) also known as hairy and enhancer of split related-1 (HesR-1) or homocysteine-responsive endoplasmic reticulum-resident ubiquitin-like domain member 2 protein (Herp2) and transcription factor 7 (Tcf7) transcription factors.[131, 157, 158] BMP-2 promotion of apoptosis occurs through the BMP-1 receptor.[131] It also has been shown to promote apoptosis through a non-Smad protein kinase (PK) C-dependent pathway.[157] The non-Smad PKC-

dependent path increases BAX/BCL-2 and increases the amount of cytochrome c released from the mitochondria therefore which activates caspase-9 and the other effector caspases to initiate osteoblast apoptosis.[157] TGF-β1 exerts a negative regulation of BMP-2 at transcription.[143]

For chondrocytes BMP-2 has been shown to increase the expression of some ECM proteins, such as aggrecan and type II collagen.[102, 159] However it was also shown to have negative impacts as well such as ECM degradation.[102] BMP-2 has also been shown to upregulate vascular endothelial growth factor (VEGF) transcription and translation in chondrocytes.[160]

BMP-7 is known to have a positive effect on cartilage homeostasis, maintaining levels of collagen II and ECM.[161, 162] Chondrocytes incubated with BMP-7 had increased levels of proteoglycan synthesis even in the presence of the catabolic cytokine, IL-1.[163] Additionally BMP-7 is known to improve chondrocyte survival as well as inhibit proinflammatory responses initiated by exposure to IL-1 or IL-6.[163]

1.4.5.3 Vascular Endothelial Growth Factor, Platelet-Derived Growth Factor and Fibroblastic Growth Factor

Other major growth factors in osteoblast and chondrocyte functioning are VEGF, platelet-derived growth factor (PDGF) and fibroblastic growth factor (FGF). VEGF, made of seven members, VEGF-A – VEGF-F is constitutively expressed by chondrocytes and osteoblasts.[164, 165] In osteoblasts VEGF synthesis is believed to be upregulated by BMP-2 and by TGF-β1 through the MAPK pathway.[165, 166] VEGF interacts with osteoblast cell receptors for the regulation of cell migration and ECM mineralization.[166, 167] On chondrocytes VEGF interacts with cell receptors that regulate cell survival.[166] VEGF levels are low in mature chondrocytes in articular cartilage but are higher in the growth phase, leading to the idea that increased expression of VEGF could lead to increased matrix synthesis.[168] Additionally VEGF is thought to regulate chondrocyte apoptosis through regulating the BCL-2/BAD concentration levels.[168]

PDGF binds to the platelet-derived growth factor receptor (PDGFR) on osteoblasts to increase gene expression for osteoblast proliferation through tenascin-C [169]. Studies evaluating the effect of PDGF, or platelet derived growth factor, on chondrocytes concluded that PDGF had a stimulatory effect on chondrocytes. However for differentiating chondrocytes PDGF has been shown to be α antagonist, causing a decrease in the amount of proteoglycan produced.[111]

FGF-2 is a highly conserved heparin-binding growth factor. In osteoblasts and chondrocytes it is produced and then stored in the ECM.[170, 171] FGF-2 induces increased osteoblastic proliferation and TGF-β1 production.[164] FGF-2 also is known to improve cell survival in osteoblasts through PI3K/Akt pathway and through the inhibition of caspase-3.[171, 172] Additionally FGF-2 activates the MAPK pathway in osteoblasts.[171] In chondrocytes, FGF-2 is known to increase cell proliferation and upregulate GAG synthesis .[173] Also with mechanical loading chondrocytes use FGF-2 to activate the ERK1/2 pathway.[170]

1.4.6 Catabolic Growth Factors/Cytokines

To maintain tissue homeostasis catabolic growth factors must provide ECM degradation at the same rate of the anabolic growth factor ECM expression. The main catabolic cytokines are interleukins, interferons, lymphokines, and prostaglandins. We will focus on IL-1, IL-6, and TNF-α, proinflammatory cytokines associated with the degradation of both bone and cartilage ECM. [102, 109]

1.4.6.1 IL-1

IL-1 is a family of more than nine polypeptides, originally discovered as IL-1β, IL-1α and interleukin-1 receptor antagonist (IL-1Ra) and is one of the best understood proinflammatory cytokine. [174, 175] It is believed to be a main factor in the development of osteoarthritis is diarthrodial joints. [128, 129, 176] IL-1 is synthesized in its inactive form and is activated by a protease cleavage to begin the signaling cascade.

The expression of IL-1 is controlled by two antagonists IL-1RI and IL-1RII (Figure 4.3). [129] Signaling is only initiated with the ligand binding of IL-1 to IL-1RI because IL-1RII is a decoy receptor and will not initiate the IL-1 signaling pathway. [129, 174] Once IL-1RI binding occurs, IL-1RI recruits and binds with IL1RAP. [175] Interleukin-1 receptor activate kinase-1/ interleukin-1 receptor activate kinase-2 (IRAK1/2) and the adaptor protein MyD88 then activate tumor necrosis factor receptor-associated factor (TRAF)-6. [174, 175] TRAF6 then initiates the ERK, MAPK, JNK, p38 and NF-κB pathways. [175, 177, 178]

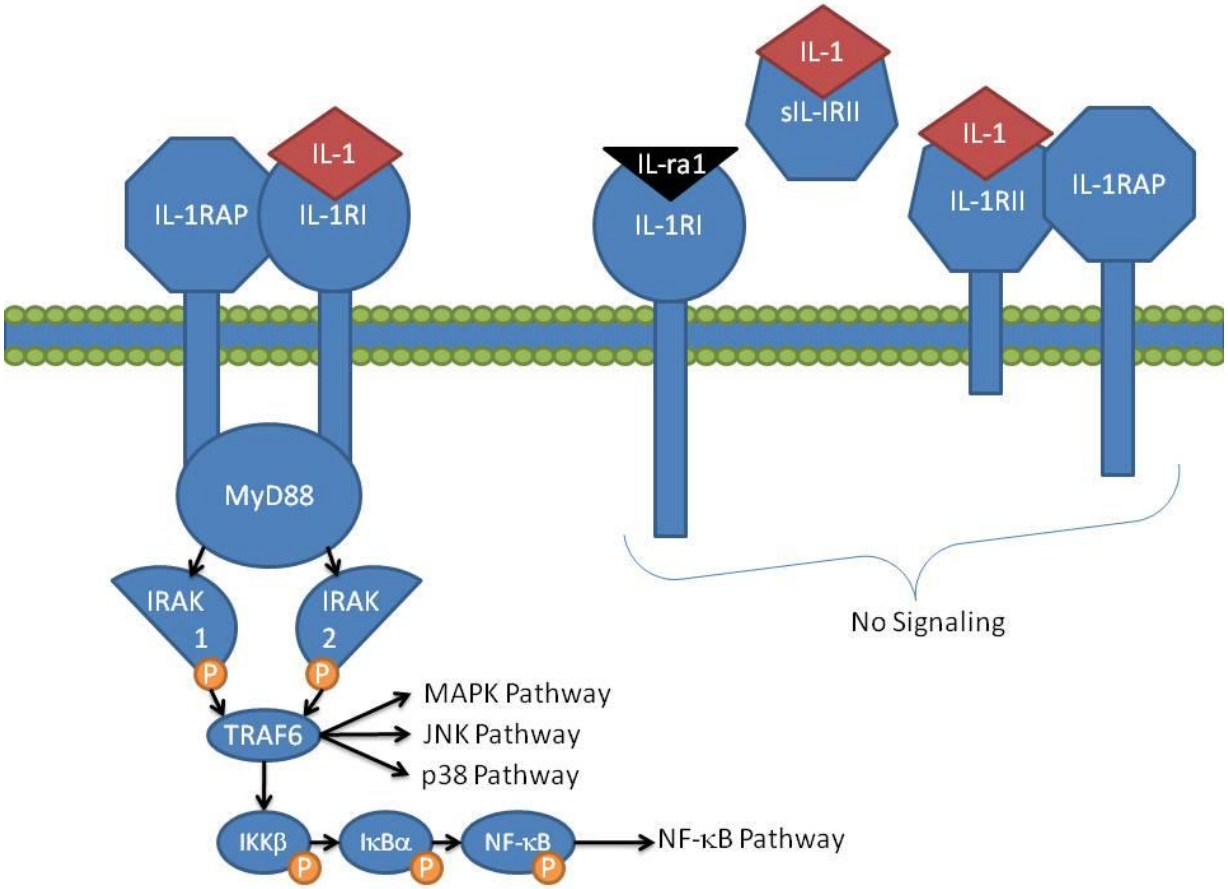

Figure 1.4.3: IL-1 signaling pathway. IL-1 signaling is controlled by IL-IRI and IL-IRII. IL-1RII is a decoy receptor and signaling is only initiated when IL-1 binds with IL1-RI. Once bound, IL-1RAP is recruited and along with the adaptor protein, MYD88, IRAK1/2 are phosphorylated to initiate the NF-κB pathway. Adapted from Boch [174] and Blanchard [179].

NF-κB is regarded as the "master switch" of the inflammation cascade. [108] It is a member of the C-Rel proto-oncogene protein (Rel) family. [180] As an inactive protein it is bound to I-κB, if I-κB is phosphorylated the NF-κB subunits, (commonly 50 and p65), reform into a dimer and initiate the NF-κB signaling pathway. [180, 181] NF-κB translocates to the nucleus and mediates gene transcription through binding to DNA at κB sites. [175, 176]

1.4.6.1.1 IL-1 in Osteoblasts and Chondrocytes

IL-1 has been identified as the main cytokine for the resorption of bone while inhibiting new bone formation since the discovery of its role in 1983. [182, 183] IL-1α inhibits ECM mineralization, decreases type I collagen synthesis, and decreases ALP. [184] IL-1α also increases bone resorption by stimulating osteoblast expression of macrophage colony-stimulating factor (M-CSF) and prostaglandin E2 (PGE_2) while decreasing expression of OPG, all known factors in the recruitment and differentiation of osteoclasts. [185] IL-1β is also known to increase osteoblast apoptosis through the increased expression of Fas. [186]

The impact of IL-1 on chondrocytes in osteoarthritic cartilage has been well studied. In response to IL-1 and lipopolysaccharide stimulation chondrocytes have been shown to use nitric oxide (NO) to inhibit proteoglycan synthesis and cell proliferation. [187] Additionally IL-1 increases NO production by activating nitric oxide synthase type II (NOS2). [108] Chondrocytes cultured with IL-1 had inhibited levels of collagen type II synthesis known to occur through the down regulation of one component of type II collagen. [117, 128] Not only does IL-1 reduce collagen II production but it also upregulates the production of MMPs and aggrecanases to degrade the ECM. [117] IL-1 moderates the impact of TGF-β by initiating the nuclear transcription factor - kappaB (NF-κB) pathway to synthesize a transcription factor that competes with the transcription factors for TGF-β and in turn causes the down regulation of TGF-β .[117] IL-1 also accomplishes this through the increased expression of Smad7 to inhibit TGF-β

signaling. [117]

1.4.6.2 IL-6

There are 10 identified members of the IL-6 family however IL-6 has been shown to be the most influential on bone resorption and formation. [179] It has been shown to be anabolic by increasing ECM mineralization, ALP expression and inhibiting apoptosis but also has catabolic effects through the inhibition of osteoblast proliferation and stimulating osteoclastic resorption. [179, 188] Since osteoblasts express low levels of interleukin-6 receptor (IL-6R), soluble interleukin-6 receptor sIL-6R is necessary for IL-6 to have a significant impact at physiological levels.

IL-6 signaling is initiated with ligand binding to IL-6R and interleukin 6 signal transducer (gp130). [189] IL-6 binding causes the activation of tyrosine kinases on JNK to activate the SHP2/SCH and signal transducer and activator of transcription (STAT) 1/3/5 pathways. STAT1/3/5 leads to the catabolic phenotypes through p21, RANKL, BAX/BCL2 pathways. [179, 190] The activation of SHP2/SHC leads to the anabolic pathways of IRS1/2, PI3K, and Ras/ proto-oncogene serine/threonine-protein kinase (Raf). These anabolic phenotypes are seen through the expression of IL-6, tissue inhibitor of metalloproteinase (TIMP)-1, Mcl-1, FBJ osteosarcoma oncogene (c-fos) and jun B proto-oncogene (JunB). [179] Additionally culturing osteoblasts with IL-6 increased the transcription of IGF-1 and BMP-6, both growth factors known to increase osteoblast proliferation. [190] However IL-6 also acts catabolically though the stimulation of osteoblasts to release paracrine factors to activate osteoclasts. [189]

The effects of IL-6 on chondrocytes are also in debate. Chondrocytes cultured with IL-6 showed catabolic effects including reduced proteoglycan synthesis and increased MMP production. [108, 128] Other studies showed that IL-6 had anabolic effects with chondrocytes increasing TIMP production and activation of collagen synthesis. [128] This difference seems to be dependent on the availability of sIL-6R. [108] If sIL-6R is present then the catabolic inhibition of proteoglycan synthesis and MMP

stimulation occurs. [108]

1.4.6.3 TNF-α

TNF-α is a membrane bound protein that once cleaved may act as a cytokine similar in function to IL-1. [128] TNF-α is proteolytically cleaved by MMPs then binds with TNF-R1 or TNF-R2, both found on osteoblasts and chondrocytes. [128] Once bound the TNF receptor and ligand complex form a trimer and begins the signaling pathway. TNF receptors associate with tumor necrosis factor receptor-associated death domain protein (TRADD) to initiate the signaling pathways through FADD and TRAF2/5. [102, 191] TRAF 2/5 lead to the activation of the NF-κB and MAPK pathways. [102, 128, 191] The FADD pathway initiates apoptosis through the activation of the caspase pathway.

TNF-α inhibits osteoblastic mineralization of the ECM by decreasing gene expression of collagen Ia, IGF-1, ALP, and osteocalcin. [191] Additionally in osteoblasts TNF-α is able to inhibit anabolic BMP signaling through the activation of NF-κB and the degradation of Runx2 by upregulation of Smurf1/2. [192, 193] TNF-α also inhibits ALP activity, preventing bone growth after remodeling. [192] Apoptosis of osteoblasts is also promoted through the NF-κB pathway. [193] In osteoblasts and in chondrocytes TNF-α increases catabolic activity by stimulating gene expression of MMPs. [161, 191]

Increased levels of TNF-α is known to be a marker of damaged cartilage. [102] TNF- α regulates a number of chondrocyte factors including ECM degradation, apoptosis, and MMP synthesis. [194, 195] TNF- α controls the synthesis of ECM components through multiple pathways. It inhibits the synthesis of collagen II through the NF-κB pathway and decreases the mRNA production of aggrecan through the MAPK pathway. [161] TNF- α also initiates ECM degradation through the upregulation of MMPs and aggrecanase through the MAPK pathway. [195, 196] Like IL-1, TNF- α also increases the production of NO through the activation of NOS2. [108]

1.4.7 Hormones

1.4.7.1 Growth Hormone and Parathyroid Hormone

Endocrine signaling is an important regulator of osteoblast and chondrocyte signaling. [124, 197] Growth hormone (GH) and parathyroid hormone (PTH) are two of the most dynamic regulators of cell growth, proliferation, ECM synthesis and survival. [101, 120, 124, 198] GH is a key regulator of IGF-1 through the activation of IRS-1 by JNK within the GH pathway. GH can also activate ERK1/2 and MAPK signaling pathway in osteoblasts. Similarly PTH works to regulate both osteoblast proliferation and apoptosis. [197] PTH activates both the PKA and PKC pathways to regulate the expression of gene for the production of collagenase III, osteocalcin. [197] PTH inhibits osteoblast apoptosis through both the regulation of BCL-2/BAD ratio and the increased expression of Runx2 to maintain survival genes. [199] PTH has also been shown to increase the production of IL-6, which may activate osteoclast functions. [98]

1.4.7.2 Adiponectin

Adiponectin is a hormone that is more present in women than in men, similar in structure to TNF-α.[200] Recent studies have linked increased levels of adiponectin to cartilage degeneration. [201] Culture of chondrocytes with adiponectin showed an increased production of IL-6, MMP-3, and MMP-9. It also increased the production of NOS2. [201] In osteoblasts adiponectin has an alternate effect. It has shown to upregulate mRNA expression of ALP along with causing an increase in matrix mineralization.[202]

1.4.8 Mechanotransduction

In addition to initiating intracellular signal expression through the binding of signaling molecules to receptor, changes in the physical environment also initiate cell signaling through a process called mechanotransduction. Physical stimuli is transferred from the ECM to receptors on the cell surface then through the cell membrane and transmitted to the nucleus to make changes in gene expression. [203]

Mechanotransduction occurs through three steps: 1)ECM-coupling, where the mechanically stimulated ECM interacts with the transmembrane protein, 2)coupling, where the forces are transmitted from the transmembrane protein to biochemical signals within the cell, and 3)gene expression change, biochemical signals are regulated by nuclear transcription changing gene expression levels. [110]

For both chondrocytes and osteoblasts mechanotransduction occurs through integrins, cadherins and Ca^{+2} channels. [203, 204] Integrins are the main mode of mechanotransduction as they connect the ECM to the cytoskeleton and other intracellular signaling molecules. [15, 110, 205] Integrins are a αβ heterodimeric transmembrane receptors. [110] Each integrin domain consists of an extracellular

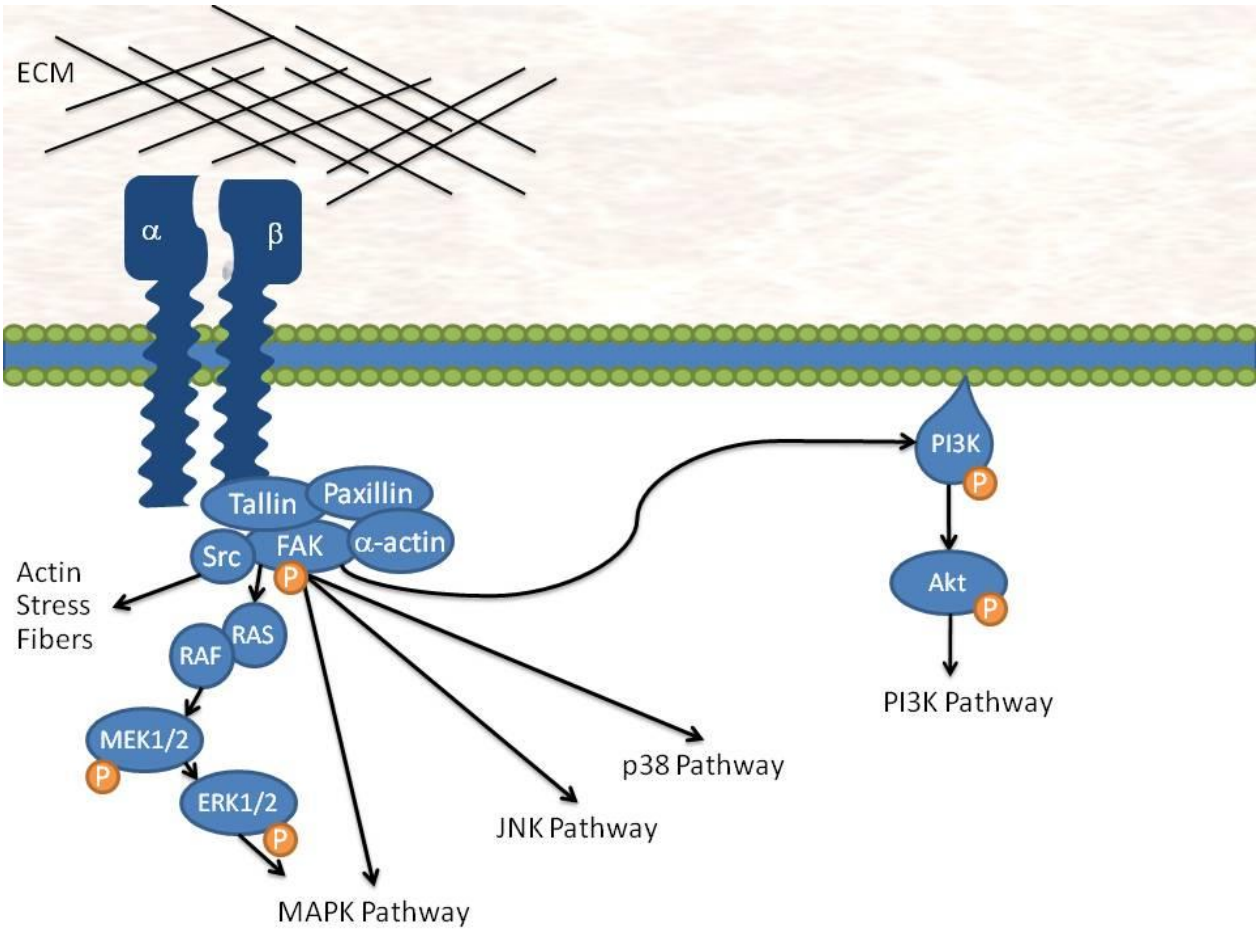

Figure1.4.4: Integrin mechanotransduction signaling. [209] Ligand binding initiates mechanotransduction. Once ligand binding occurs, additional integrins, FAK, and adapter proteins are recruited to create FACs. With the subsequent activation and autophosphorylation of FAK the MAPK, JNK, p38 and PI3K pathways are initiated.

segment, a transmembrane region and an intracellular region. [15, 106, 110] There are 18 known α and 8 known β subunits in mammals. [110, 112] Principally, in the cytoplasm the β subunit is for binding whereas the α subunit functions in a regulatory manner. [106] Integrin ligand binding can occur with collagen, fibronectin, vitronectin and laminin [110] depending on the domain structure.

Integrin signal pathways are initiated by ligand binding to either an extracellular or intracellular subunit domain. For this chapter we will focus on the integrin pathway for extracellular mechanotransduction as it is the most common transmission of physical stimuli. Once the extracellular domain binds with a ligand, multiple actions occur, including the clustering of multiple integrins, the recruitment of focal adhesion kinases and adapter proteins (Figure 1.4.4). [110] Adapter proteins (paxillin, tensin, talin, α-actin) bind, along with FAK to form a complex allowing the binding of the cytoplasmic tail to the actin cytoskeleton forming actin stress fibers. [15, 100, 110, 206] FAK is one of the main components of the integrin mechanotransduction pathway. [15, 106] Once associated with the focal adhesion complex (FAC), FAK is subsequently activated, autophosphorylates and then binds with sarcoma (Src) to form a Src-homology-2 binding domain. [102, 110] As an SHC-2 it is able to phosphorylate other proteins such as paxillin and tensin. [110, 206]

This process is additive as the concomitant phosphorylation activates additional paxillin and tensin, forming more FACs. The recruitment of these enzymes, proteins and other necessary substrates to a concentrated area improve reaction kinetics by reducing any spatial dependence on substrates necessary for signal transduction. Activated FAK also initiates the PI3K, p38 and JNK pathways, as well as ERK1/2 to concomitantly initiate the MAPK pathway. The MAPK pathway may control cell proliferation, survival and differentiation, as it can function in an anabolic or catabolic manner (Figure 4.5). [106, 171, 175]

Integrin binding and subsequent clustering may activate other mechanosensing cell components such as stretch activated ion channels and growth factor receptors and cell-surface associated proteoglycans. [110] This allows for other signal transduction through other mechanoreceptors such as lipid raft domains, caveolins, and adherens junctions. [15, 203]

Growth factors such as TGF-β1 and IGF-1 have shown to increase the expression of integrins as well as the production of Shc, Erk1/2 and other second messengers seen in the integrin pathway therefore there is an interaction between growth factor and integrin signaling pathways. [106, 111, 198, 207, 208] This is especially seen by the activation of the MAPK pathway by both growth factors and integrins to regulate cell proliferation and survival. [124]

1.4.8.1 Osteoblasts

Bone is known to be sensitive to loading and shear stresses and may be anabolic depending the rate, degree and frequency of loading. [15, 203, 210] For osteoblasts ion channels, integrins, connexins, and plasmid membrane components play a role in transmitting mechanical stimuli into chemical signals. [15, 203] Integrins are a primary method of mechanotransduction in osteoblasts. [15] These integrins transmit signals mainly through the β1 subunit. [15] Specifically osteoblasts have been demonstrated to activate integrin αvβ1 and integrin β1 during periods of mechanical stress. [15] FAK is phosphorylated at tyrosine during osteoblast mechanical stimulation which then concomitantly activates the MAPK pathway through interactions with c-src, Ras and growth factor receptor-binding protein 2 (Grb2). [15] Specifically the MAPK pathway is activated through ERK1/2 which has shown to increase the production of collagen III and collagen I as well as increase proliferation. [15, 211] Loading has also been shown to activate osteoblasts to increase matrix production, upregulate IGF-1, VEGF, TGF-β1, BMP-2 and BMP-4. [203] Mechanical stress through shear stress also impacts osteoblast function causing the tyrosine

phosphorylation in FAK which may regulate cell growth and survival in osteoblasts. [15] The upregulation of these growth factors leads to the conclusion that there is likely crosstalk between the anabolic growth factors and integrin signaling to upregulate bone's response to physical stimuli. [203]

1.4.8.2 Chondrocytes

Understanding mechanotransduction in chondrocytes is integral in developing an optimal tissue engineered cartilage replacement because of the wide range of mechanical stresses that cartilage endures. Without this understanding of the impact of tensile, shear or compressive forces on chondrocytes *in vivo* one cannot develop a tissue replacement robust enough to ensure cell survival and proliferation. [110] Mechanical cyclical stimulation from the ECM impacts chondrocyte development, morphology, phenotype, function and even survival. [106, 212]

Chondrocytes receive mechanical stimuli through multiple receptors including stretch-activated ion channels, CD44 molecule (Indian blood group) (CD44), anchorin II, and integrins. As in chondrocytes the main mechanotransduction receptors are integrins. The main integrins expressed in chondrocytes are: $\alpha1$, $\alpha3$, αv, and $\alpha5\beta1$, with $\alpha1\beta5$ as the primary integrin. [106, 208] The $\alpha1\beta5$ integrins transmit mechanical changes to the ECM through its interactions with fibronectin. [213] Integrin transduction of mechanical stimuli can regulate differentiation, matrix remodeling, and cell survival for chondrocytes. [106, 207] In chondrocyte ligand binding of collagen II to the integrin $\beta1$ subunit causes the activation of Shc and subsequently the Ras-MAPK signaling pathway. [106] The Ras-MAPK pathway is known to regulate chondrocyte growth, differentiation and apoptosis. [106, 175] The Ras-MAPK pathway may induce apoptosis through multiple pathways: activating caspase 3 and subsequent PARP cleavage; inhibiting map erk kinase (MEK), and by activating JNK pathway. [106]

Chondrocytes cultured under cyclical loading show an increase in GAG production. [214] Even in the presence of catabolic cytokines, IL-1β, mechanical loading of chondrocytes caused an upregulation of both proteoglycan synthesis and cell proliferation. [187, 215] Oscillatory loading of superficial zone

chondrocytes increased proteoglycan synthesis but not in middle or deep zone chondrocytes. [216] Not all stress is anabolic to chondrocytes, chondrocytes in monolayer express higher levels of NO in response to increasing fluid flow shear stresses. [187] NO may contribute to chondrocyte loss of phenotype, apoptosis and ECM degradation.[180, 201, 217]

1.4.8 Dual Growth Factor Studies

With the success of many anabolic growth factors increasing cell proliferation and ECM synthesis current studies are interested in elucidating any positive impact by combining multiple growth factors in tissue engineering scaffolds. Exogenous delivery of multiple growth factors works to recapitulate the complex *in* vivo environment. See Table 1.4.2 for a list of different biomaterials, delivery of growth factors and their impact on cell proliferation and ECM synthesis. Newer studies have begun to elucidate the role of sequentially adding growth factors to best recapitulate the *in vivo* milieu. This is the next logical step in growth factor studies to develop/design an optimal tissue engineering scaffold. However there are currently not enough studies to be able to conclusively determine which combination of anabolic growth factors provide the optimal signaling for cell proliferation and ECM synthesis.

Table 1.4.2: Impact of Dual Growth Factor Delivery

Growth Factors	Targeted Cell Type	Growth Factor Delivery Material	ECM Synthesis	Cell Proliferation	Reference (s)
BMP-2, IGF-1	Chondrocyte	Agarose Gel	++		(Elder and Athanasiou, 2009)
BMP-2, IGF-I, TGF-β1	Chondrocyte	Agarose Gel		+	(Elder and Athanasiou, 2009)
IGF-1, TGF-β	Chondrocyte	oligo (poly (ethylene glycol) fumarate), gelatin	-	-	(Holland et al., 2007, Holland et al., 2005)
IGF-1, TGF-β	Chondrocyte	poly (lactic acid-co-glycolic acid)	+		(Elisseeff et al., 2001)
IGF-1, TGF-β1	Chondrocyte	poly (ethylene oxide) hydrogels in poly (lactic acid-co-glycolic acid) (PLGA)	+		(Elisseeff et al., 2001)
IGF-1, TGF-β1	Osteoblast	poly(D,L-lactide)	+		(Wildemann et al., 2004)
IGF-1, FGF-2, TGF- β1	Chondrocyte	PLGA fiber mesh		+	(Pei et al., 2002)
IGF-1, TGF-β1	Chondrocyte	Polyglycolic acid	-	+	(Blunk et al., 2002)
VEGF, BMP-2	Osteoblast (Bone)	PLGA microspheres in PPF rod surrounded by gelatin hydrogel	++		(Kempen et al., 2009)
VEGF, BMP-2	(Osteoblast) Bone	gelatin microsphere in PPF scaffold	++		(Patel et al., 2008)

1.4.9 Conclusion

Understanding the wide range of impact from cytokines, growth factors and hormones on osteoblasts and chondrocytes allows for their combination and use in designing an optimal tissue engineering scaffold for the skeletal system. Growth factors such as TGF-β and IGF-1 are anabolic for both osteoblasts and chondrocytes; whereas cytokines such as IL-1 and TNF-α are catabolic. In addition to the growth factors and cytokines that act as autocrine and paracrine signaling molecules one must take into account the impact of hormones such as PTH, GH and adiponectin when developing bone and cartilage replacements. With further studies as to the additive effects of dual delivery of growth factors one will be able to determine the optimal factors in developing a tissue engineering replacement for either bone or cartilage.

Chapter 2: Evaluation of the In Vitro Cytotoxicity of Crosslinked Biomaterials[1]

2.1 Introduction

Cell and tissue response are key factors in the design and application of successful biomaterials. One method to evaluate cell and tissue response is to measure *in vitro* cytotoxicity, or its quality of being toxic to a cell. Cell toxicity is determined by cell lysis (death) or the inhibition of cell proliferation. Prior to investigating a material *in vivo*, cytotoxicity can provide insight to any potential issues with the local tissue response.

For bone tissue regeneration key factors in designing ideal biomaterials include mechanical strength, biocompatibility, and consistent mechanical performance during degradation.[218] Poly(propylene fumarate) (PPF) is a well characterized polymer that has been demonstrated to fit these characteristics.[52, 219] PPF is an aliphatic polyester with a repeating unit that contains a carbon-carbon double bond, flanked by two ester groups.

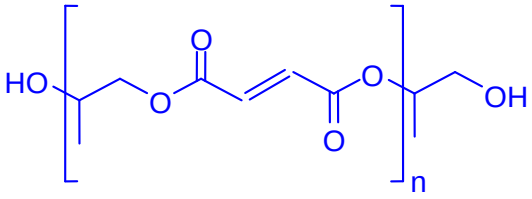

Poly(Propylene Fumarate)

Figure 2.1: A Schematic of Poly(propylene fumarate). Poly(propylene fumarate) contains a repeating unit of two ester groups flanking a carbon-carbon double bond.

Covalent crosslinking of PPF occurs through the unsaturated carbon bond on the fumarate functional group either by thermal- or photo-initiation. Hydrolytic degradation of the ester bond produces fumaric acid and propylene glycol as byproducts.[220] As fumaric acid is a known byproduct of the Kreb's cycle and propylene glycol is commonly used as a food additive, both of these degradation products are thought to be nontoxic in low concentrations.[218]

---

[1]Adapted from: MO Wang, Etheridge, JM, Thompson, JA, Vorwald, CE, Dean, D, and JP Fisher. "Evaluation of the In Vitro Cytotoxicity of Crosslinked Biomaterials." Biomacromolecules. 2013, 14 (5), pp 1321–1329 DOI: 10.1021/bm301962f

Previous studies have evaluated the cell and tissue response and degradability of thermally crosslinked PPF and have found it to be acceptable for *in vivo* implantation with responses ranging from a lack of an inflammatory response to a mild inflammatory response. [81, 221, 222] Although previous studies have evaluated the toxicity of thermally crosslinked PPF they were performed either using *in vivo* models or when using an *in vitro* model, they did not implement the previously developed standards for *in vitro* cytotoxicity. With the further development of PPF as a photocrosslinkable polymer, many studies have evaluated the use of PPF as a coating for cortical bone implants, a scaffold to repair critical sized bone defects, and as a delivery method for signaling factors. [79, 223-225] Additional studies have evaluated the *in vitro* degradation of photocrosslinked PPF. [226] *In vivo* studies of photocrosslinked PPF have identified it as having a mild tissue response initially following implantation but after 8 weeks a reduction in this response was observed. [78] Previous work has also identified that un-crosslinked PPF co-polymers (PPF/PPF-diacrylate (PPF/PPF-DA)) are highly cytotoxic (viability <3%), compared to crosslinked networks; whereas crosslinked PPF networks had cell viabilities >80%.[227] This study investigates the *in vitro* cytotoxicity of PPF that has been photocrosslinked using the photoinitiator bis(2,4,6-trimethylbenzoyl) phenylphosphine oxide (BAPO) using the ISO 10993-5 standards.

We hypothesized that PPF will have a low cytotoxic response as its degradation byproducts are nontoxic, and previous research has demonstrated biocompatibility using other crosslinking methods. To test this we investigated the cellular response of four cell types: fibroblasts (L929), pre-osteoblasts (MC3T3) and mesenchymal stem cells (human and canine) (hMSC, cMSC) to PPF. The cell types studied where chosen to represent the many tissues that PPF will interact with *in vivo* during bone regeneration.

2.2 Experimental Section: Materials and Methods

2.2.1 Poly(propylene fumarate) synthesis and film fabrication

Poly(propylene fumarate) was synthesized in a two-step process as described previously.[228]

Briefly, propylene glycol and diethyl fumarate were combined in a 3:1 molar ratio. Zinc chloride and hydroquinone were added in a 0.01:0.002 molar ratio to act as catalyst and radical inhibitor, respectively. The solution was reacted under a flow of nitrogen gas producing ethanol as a byproduct and *bis*(hydroxypropyl) as the intermediate. The second step is a transesterification of the intermediate, performed under a vacuum, to produce PPF with propylene glycol as a byproduct. Gel permeation chromatography was used to calculate the number average molecular weight (M_n) and polydispersity index (PDI) of the purified PPF. For the 3 hour UV crosslinked PPF (180M PPF) M_n = 1100g/mol and PDI = 2.7; for the PPF films crosslinked using 30 minute UV exposure (30M PPF) the M_n = 1290g/mol and PDI = 2.01. Thin films of PPF were photocrosslinked using BAPO as an initiator according to previously reported methods.[229] A solution of 4g BAPO in 10 mL methylene chloride was prepared. The PPF mixture was spread evenly onto a glass plate and placed into the oven to spread for 2 minutes. A glass plate was depressed on top of the PPF mixture to create a thin film. The two plates were then placed in a UV cross-linking light box for 3 hours (180M) or 30 minutes (30M). The films were then washed in phosphate buffered saline (PBS) for 15 minutes to remove surface debris followed by a 30 minutes wash in acetone to remove soluble components and then washed twice, 15 minutes in PBS to remove any remaining acetone. One group was left un-washed to evaluate the soluble components of the 30M film (UN-30M).

2.2.2 Sol Fraction and Crosslinking Density

To assess the crosslinking density the sol fraction was measured per the previously described method.[52] Samples of the photocrosslinked film were weighed (W_i) prior to incubation in acetone, the solvent. The samples were then submerged in the solvent for 24 h. After incubation, samples were dried overnight and weighed again (W_d). Sol fraction was calculated using the formula

$$sol\ fraction = \frac{W_i - W_d}{W_i}\ x\ 100\%$$

Crosslinking density (q) was then approximated using the Charlesby-Pinner equation and the relationship between crosslinking coefficient (δ), the weight average degree of polymerization (X_w) and the sol fraction (s). Sol fraction and crosslinking coefficient are related by the Charlesby-Pinner equation which assumes the following: a high degree of crosslinking without main chain scission, the initial molecular weight distribution is random (PDI ≈ 2), that the structure of the polymer does not affect crosslinking or main chain scission, and that the degree of crosslinking and main-chain scission is proportional to the radiation dose. From the crosslinking coefficient, the weight average degree of polymerization (X_w), derived from $M_{w,}$ and M_o, the molecular weight of the monomer unit (156.19Da), the crosslinking density was approximated using the following formula.[28] [230]

$$q = \frac{1}{s + \sqrt{s}} - \frac{M_w}{M_o}$$

2.2.3 Material Preparation

Tests were performed using either a 12 well or 24 well tissue culture polystyrene plate (Corning, Corning, NY) with surface areas of 3.8cm^2 or 1.9cm^2, respectively. High-density polyethylene (HDPE) (U.S. Plastic Corp, Lima, OH) and polyurethane film containing 0.1% zinc diethyldithiocarbamate (ZCF) (Hatano Research Institute, Food and Drug Safety Center, Kanagawa Japan) samples were measured to a minimum of 38mm^2 or 20mm^2, for the 12 well or 24 well tests, respectively, to ensure that at least 10% of the surface area of the well was covered by the material. After washing and drying, the PPF was apportioned using a calculation of the density of PPF ρ, (ρ = 1.3g/cm^3), film thickness (t), and the required area of sample (A) using the formula

$$Sample\ weight \geq \rho tA$$

This formula ensured that the surface area of each sample was at least 10% of the total well surface area. Each material used was sterilized at 121°C for 15 minutes prior to use in cell culture. For extract studies the method used is the same, but the required sample mass is halved because both sides of the sample are exposed to media.

2.2.4 Cell Culture

Four cell types were evaluated: L929 (ATCC, Manassas, VA), MC3T3 (ATCC), hMSC (Lonza, Walkersville, MD), and cMSC (Case Western Reserve University, Cleveland, OH). L929, mouse fibroblasts, are suggested for use per ISO Standard 10993-5. L929 cells were cultured per the manufacturer's specifications with Minimum Essential Medium (MEM) (Life Technologies, Frederick, MD) and 10% horse serum (Life Technologies). MC3T3, a mouse osteoblast precursor cell, were cultured per the manufacturer's specifications with alpha Minimum Essential Medium (αMEM) (Life Technologies) containing ribonucleosides, deoxyribonucleosides, 2 mM L-glutamine (Life Technologies), 1 mM sodium pyruvate (Life Technologies), and 10% fetal bovine serum (FBS) (Life Technologies). The hMSCs were cultured as previously described and per the manufacturer's protocol, with Dulbeccos Modified Eagle Medium (DMEM) (Life Technologies), supplemented with 10% fetal bovine serum (Life Technologies), 1.0% v/v penicillin/streptomycin (Life Technologies), 0.1mM non-essential amino acids (Life Technologies), and 4mM L-glutamine (Life Technologies).[231, 232] The cMSCs were cultured with low glucose DMEM (Life Technologies) containing 10ng/mL of fibroblast growth factor and 10% FBS. Cells were plated and grown to ~80% confluency prior to initiating the assays.

2.2.5 Cytotoxicity Assays

For all assays HDPE (U.S. Plastic Corp.) was used as a negative, or non-cytotoxic, control. Cells cultured under normal, or blank conditions and without any material were used as a blank control (blank). For the direct and indirect testing a polyurethane film containing 0.1% zinc diethyldithiocarbamate (ZCF) was used as a positive, or a cytotoxic, control which has been shown to provide a reproducible cytotoxic response.[89, 90] For the extract testing a 70% dilution of methanol was used as a cytotoxic control.

Following ISO standard 10993-5 three different culturing methods were implemented to evaluate if there is a cytotoxic response to PPF: direct contact, indirect contact and extract tests. For the direct contact test (Figure 2.2A) cells were plated and cultured per the methods described above. The direct contact test allows for the physical interaction of the cells and the material. The test was initiated by placing the material onto the cell monolayer. The material was incubated at 37°C and 5% CO_2 for 24 h

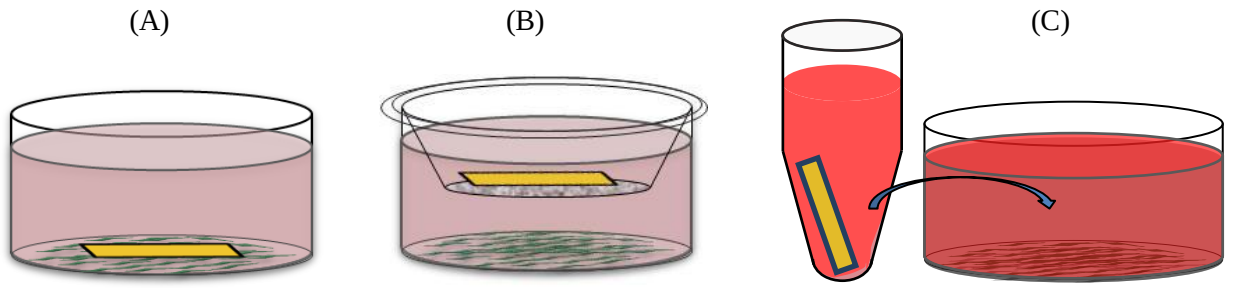

Figure 2.2: A Schematic of the Cytotoxicity Tests. (A) Direct contact test where cells are seeded and the material is placed directly on top of cell sheet. (B) Indirect contact test where the material is placed into a transwell insert, which is cultured with cells seeded on the bottom of the well plate. (C) Extract test where the material is incubated in the appropriate culture media for 24

after which the cytotoxicity of the material was evaluated qualitatively with fluorescence microscopy and quantitatively through the XTT cell metabolic activity assay (Roche, Mainheim, Germany). To reduce disrupting the cell monolayer the materials were removed using a Pasteur pipet attached to a vacuum line so that the material and the media were removed simultaneously.

The indirect contact test (Figure 2.2B) allows for the interaction of any leachable byproducts to interact with the cell monolayer without direct contact of the material. The materials were placed into a transwell microplate membrane insert (3.0µm size exclusion) (Corning, Corning, NY) above the cell surface and submerged in the culture media. The treatment groups were incubated at 37°C and 5% CO_2 for 24 h prior to cytotoxic evaluation with XTT cell metabolic activity assay and fluorescence microscopy.

The extract test (Figure 2.2C) evaluates the cytotoxicity of any leachable byproducts from the material by the simulation of clinical application. Cells were plated and grown to 80% confluency prior to

initiating the assay. The materials (PPF and HDPE) were incubated with the appropriate culture media at a concentration of $3cm^2$/mL for 24 h. After 24 h, the cell culture media was removed and replaced with the extract media. Cells were then incubated at 37°C and 5% CO_2 for 24 h prior to cytotoxic evaluation with XTT cell metabolic activity assay and fluorescence microscopy. For the cytotoxic control the culture media was removed and cells were incubated with 70% methanol for 30 minutes prior to evaluation of cytotoxicity.

2.2.6 XTT Assay

The Cell Proliferation Kit II (XTT) (Roche, Mainheim, Germany) was used to quantitatively evaluate cell metabolic activity. XTT (2,3-bis-(2- methoxy-4-nitro-5-sulfophenyl)-2H-tetrazolium-5-carboxanilide) was used according to the manufacturer's protocols. The electron coupling and XTT labeling reagents were thawed and immediately combined in a 1µl:50µL ratio. Then the XTT solution was added to the cell culture wells, 500µl or 1mL for a 24 well or a 12 well plate, respectively. Absorbance was measured after 4 hours of incubation at 37°C with a M5 SpectraMax plate reader (Molecular Devices, Sunnyvale, CA). Net absorbance was calculated (A_{450}-A_{650}) for each sample of the three biological replicates. Relative cell metabolic activity was normalized to the mean of the blank culture media. Samples were evaluated, the mean cell metabolic activity and standard deviations are reported (n=5).

2.2.7 Osmolality

The osmolality of the cell culture media was measured using the Advanced™ Micro Osmometer (Advanced Instruments, Inc, Norwood, MA) using freezing point depression. The osmolality of the cell culture media measured after 24 hours of direct contact with the material, per the direct contact test. A 20µL sample was used to measure the total molar concentration of dissolved solids, three samples were used per treatment group (n = 3).

2.2.8 Fluorescence Imaging

Live/dead imaging was performed to qualitatively evaluate cell viability as described previously[233]. A live/dead solution was prepared with 4 µM of calcein AM (Invitrogen, Carlsbad, CA) and 2 µM of ethidium homodimer (Invitrogen, Carlsbad, CA) in PBS. Prior to the addition of the live/dead stain, cells were washed with PBS to remove any remaining culture media and FBS. Cells were incubated with the live/dead solution in dark conditions for 30 minutes prior to imaging. For the positive, or cytotoxic, control, cells were incubated with 70% methanol 30 minutes prior to the addition of the live/dead solution. Images were obtained with a fluorescence microscope (Axiovert 40CFL, filter set 23, Zeiss, Thornwood, NY) fitted with a digital camera (SPOT Insight 1120, or SPOT Idea 2920, Diagnostics Instruments, Sterling Heights, MI) and with an inverted TE2000-E microscope (Nikon, Melville, NY) outfitted with a CoolSnap HQ^2 (Photometrics, Tucson, AZ) digital camera.

2.2.9 Statistics

Statistical analysis was performed using ANOVA and Tukey's multiple pairwise comparison ($p<0.05$). All tests were performed in triplicate ($n=3$) unless otherwise specified. Values provided are mean ± standard deviation. Please note that only relevant statistical relationships are denoted on figures.

2.3 Experimental Section: Results

The objective of this work was to evaluate if there is a cytotoxic response to PPF. For each of the three cytotoxicity tests (direct, indirect, and extract) the cell metabolic activities of the cells exposed to 180M PPF were found to be statistically different than those exposed to the cytotoxic control, ZCF, and not statistically different from the cells exposed to HDPE, and blank culture media. Additionally, no changes in cell viability, morphology, vacuolization or detachment were observed in the cells exposed to 180M PPF, HDPE or blank culture media.

Sol fraction was measured and used to estimate the crosslinking density of the PPF films used for

cytotoxicity evaluation. For the 180M PPF films the sol fraction was found to be 3% ± 2% (n = 7) (Table 5.1) and the crosslinking density was estimated to be 58 ± 25% (n = 7) (Table 5.2). The sol fraction for sterilized 180M PPF, 4 ± 3% (n=4), and pre-sterilized 180M PPF, 3 ± 0% (n = 3), were found to be statistically similar (Table 5.1). The sol fraction for 30M PPF films was found to be 53 ± 4% (n = 3) (Table 2.1) and the crosslinking density was calculated to be 10 ± 0% (n = 3) (Table 2.2). The crosslinking densities and the sol fractions of the 180M and 30M films were found to be statistically different ($p<0.05$).

Table 2.1: Sol Fraction of PPF

Sol Fraction of PPF	
180M PPF (n=7)	3% ± 2%
Pre-sterilization PPF (n=3)	3% ± 0%
Sterilized PPF (n=4)	4% ± 3%
30M PPF (n=3)	53% ± 4%

Table 2.1: Sol fraction was measured to calculate crosslinking density. The 180M PPF films were evaluated pre-sterilization and post sterilization to ensure that sterilization did not have an impact on the sol fraction. These groups were found to be statistically similar, and therefore it was determined that sterilization did not have an impact on the sol fraction. The 30M PPF films have a sol fraction significantly greater than the 180M PPF films ($p<0.05$)

Table 2.2: Crosslinking Density of PPF

Crosslinking Density of PPF	
180M Crosslinked PPF (n=7)	58% ± 25%
30M Crosslinked PPF (n=3)	10% ± 0%

Table 2.2: Crosslinking Density of PPF. Crosslinking density was then calculated from the sol fraction using the Charlesby-Pinner equation, crosslinking coefficient, the weight average degree of polymerization (X_w). as described previously[230],27,28. The difference in crosslinking density between the 180M PPF and the 30M PPF films was found to be statistically significant ($p<0.05$)

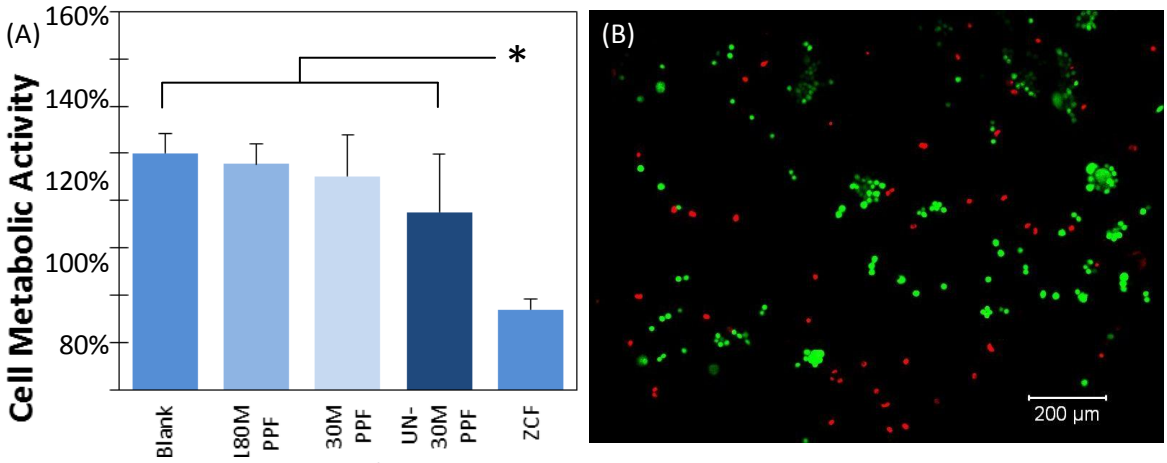

Figure 2.3 Cytotoxicity of 30M PPF. A): Cell Metabolic Activity: Cell metabolic activity for L929 cells cultured with 180M PPF, 30M PPF,UN-30M PPF and those cultured with only the culture media (Blank) were found to be statistically different from those cultured with the cytotoxic control ($p<0.05$). The (*) symbol represent a statistical difference between ZCF and all other groups ($p<0.05$). B): Fluorescent images of L929 cells. Calcein AM (green) represents live cells, and ethidium homodimer (red) represents dead cells. Cells incubated with UN-30M PPF showed increased cell detachment and cell death.

The cytotoxicity of 30M, UN-30M, and 180M PPF films was investigated using the direct contact test. There was a statistical difference in the cell metabolic activities of L929 cells cultured with 30M, 180M, and UN-30M PPF films, and the blank culture media when compared to the cell metabolic activity of the cells cultured with the cytotoxic control, ZCF (Figure 2.3A). The cell metabolic activities of the UN-30M PPF and the blank culture media were found to be statistically different (Figure 2.3A). The cell metabolic activities were 100.0 ± 8.6% (blank) 95.4 ± 8.7% (180M), 90.2 ± 17.6% (30M PPF), and 75.2 ± 24.7% (UN-30M PPF). Qualitative verification showed an increase in cell death with a large number of detached cells and dead cells in the UN-30M PPF treatment group (Figure 2.3B).

For the direct contact test, 180M PPF was shown to support a similar level of cell metabolic activity as HDPE, a material previously designated as non-toxic. Also, the cell metabolic activities of cells cultured with 180M PPF and to those cultured with blank culture media were found not to be statistically different (Figure 2.4). The L929 cells had the highest cell metabolic activity of 102.4 ± 14.6%

when directly cultured with 180M PPF. The cell metabolic activities were found to be 96.1 ± 11.5% (MC3T3), 100.3± 10.1% (hMSC), and 77.1 ± 13.0% (cMSC). These results were statistically different ($p<0.05$) from the cells cultured with the cytotoxic control, ZCF.

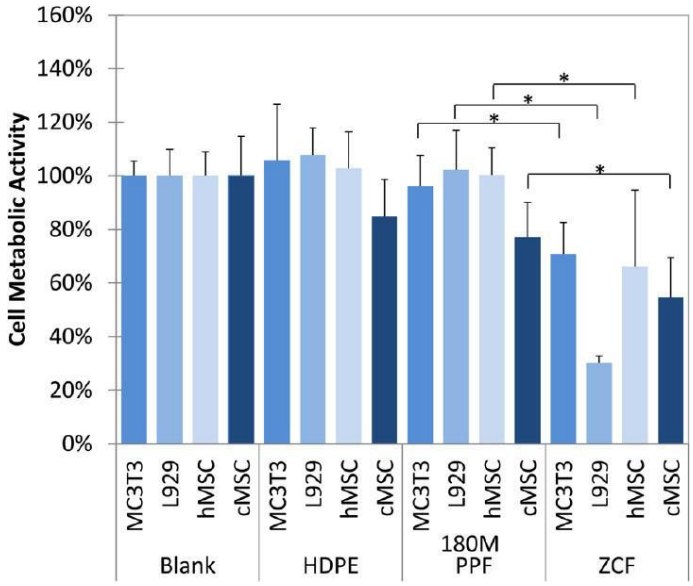

Figure 2.4: Cell Metabolic Activity (Direct Contact). Four different cell populations (MC3T3, L929, hMSC, and cMSC) were cultured in monolayer and in direct contact with HDPE, 180M PPF, ZCF, or nothing (Blank). Each cell type cultured in direct contact with 180M PPF was found to have significantly higher metabolic activity when compared to those in contact with the positive, cytotoxic control, ZCF ($p<0.05$, * designated a statistical difference between groups). There were no statistical differences found between cells cultured with 180M PPF, HDPE or under blank culture media.

Fluorescence imaging was used to confirm the XTT assay results. No changes in cell morphologies were seen in cells cultured directly with 180M PPF (Figures 2.5A – 2.5D). hMSCs that were directly exposed to 180M PPF were observed to have a spread, spindle-like morphology and appeared to be fully attached to the culture plate surface (Figure 2.5A). This spread, elongated morphology was consistent with cells that were directly exposed to HDPE (Figure 2.5E) and those that were incubated with blank culture media (Figure 2.5I). Imaging of L929 cells revealed that a normal, round morphology and confluent cell monolayer were maintained after direct incubation with 180M PPF (Figure 2.5C). The spread, confluent morphology that was observed per each cell type (Figures 2.5A - 2.5L) was notably different than the robust amount of cell detachment and cell death that was observed for cells exposed to ZCF, the cytotoxic control. Cell detachment and morphological change was observed (Figures 2.5M - 2.5P) during the direct contact test.

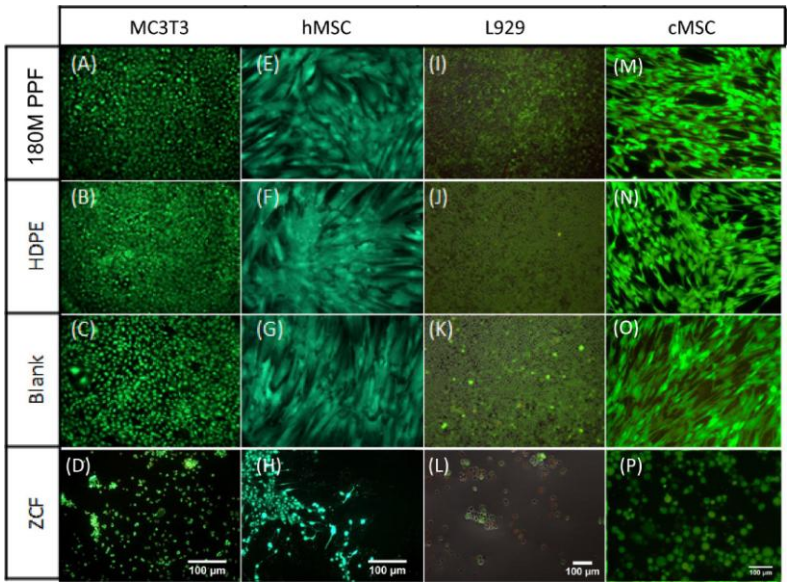

Figure 2.5: Direct Contact Test. Fluorescent images of cells, where calcein AM (green) represents live cells, and ethidium homodimer (red) represents dead cells. A - D: MC3T3 cells cultured with (A) 180M PPF (B) HDPE, (C) Blank media, (D) ZCF; 4E- 4H: hMSC cultured with (A) 180M PPF (B) HDPE, (C) Blank media, (D) ZCF; I -L: L929 cells cultured with cultured with (A) 180M PPF (B) HDPE, (C) Blank media, (D) ZCF; M - P: cMSC cells cultured with (A) 180M PPF (B) HDPE, (C) Blank media, (D) ZCF. Normal cell morphology was observed in the populations cultured with 180M PPF, HDPE and blank media.

Similar results were documented for the indirect contact test. Cell metabolic activity levels were found to be statistically similar compared to those cultured with either 180M PPF, HDPE or under blank culture media for each cell type. The highest levels of cell metabolic activity were seen in the MC3T3 cells when cultured with 180M PPF with 106.5± 7.7%. The other cell metabolic activities, when cultured indirectly with 180M PPF, were 103.5 ± 10.8% (L929), 90.6 ± 9.8% (hMSC), and 86.6 ± 6.0% (cMSC) (Figure 2.6). The lack of cytotoxic response to indirect culturing with 180M PPF was visually confirmed, no documented changes in morphology were observed compared to the non-cytotoxic control or the blank

Figure 2.6: Cell Metabolic Activity (Indirect Contact). Four different cell populations (MC3T3, L929, hMSC, and cMSC) were cultured in monolayer under indirect contact with HDPE, 180M PPF, ZCF, or nothing (Blank). Each cell type cultured under indirect contact with 180M PPF was found to have significantly higher metabolic activity when compared to those cultured with the positive, cytotoxic control, ZCF ($p<0.05$, * designated a statistical difference between groups). There were no statistical differences found between cells cultured with 180M PPF, HDPE or under blank culture media.

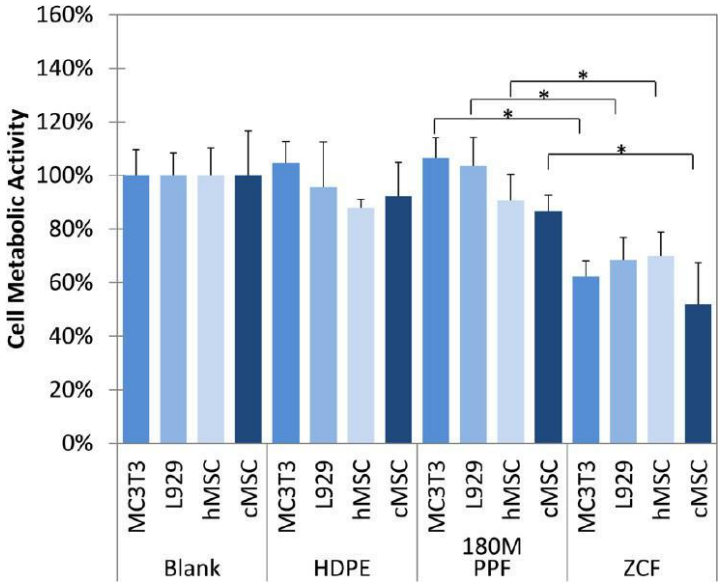

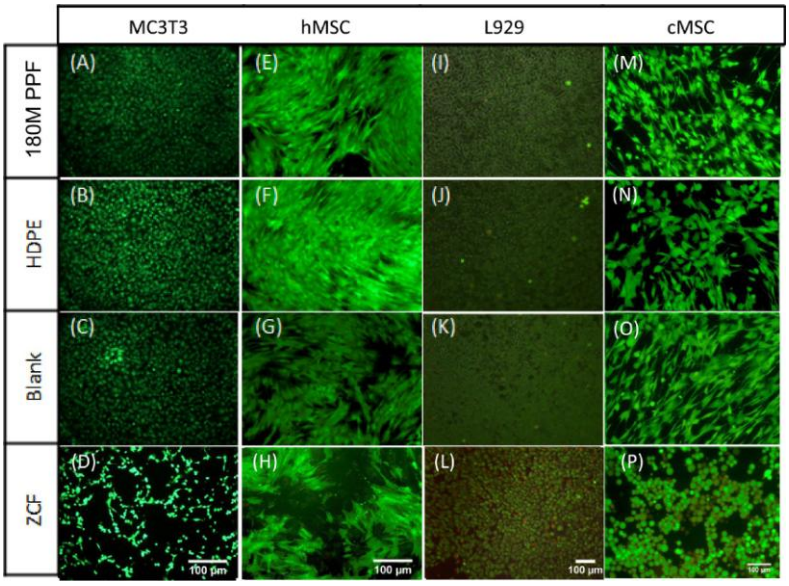

Figure 2.7: Indirect Contact Test. Fluorescent images of cells, calcein AM (green) represents live cells, and ethidium homodimer (red) represents dead cells. 6A -6D: MC3T3 cells cultured with (A) 180M PPF (B) HDPE, (C) Blank media, (D) ZCF; 6E-6H: hMSC cultured with (A) 180M PPF (B) HDPE, (C) blank media, (D) ZCF; 6I -6L: L929 cells cultured with cultured with (A) 180M PPF (B) HDPE, (C) blank media, (D) ZCF; 6M -6P: cMSC cells cultured with (A) 180M PPF (B) HDPE, (C) blank media, (D) ZCF. Normal morphology was seen in the treatment groups cultured with 180M PPF, HDPE and blank media.

culture media (Figures 2.7A-2.7E). Confluent, normal morphology was observed for cells exposed to 180M PPF, HDPE and blank culture media for each cell type (Figures 2.7A – 2.7C, 2.7E-2.7G, 2.7I-2.7K, 2.7M – 2.7O). A confluent monolayer was observed for each cell type indirectly exposed to 180M PPF. The hMSCs were elongated, spread, and maintained a characteristic spindle shape (Figure 2.7E). MC3T3s and L929s cultured with 180M PPF (Figures 2.7A and 2.7I) had similar confluency, morphology, viability, and had no noticeable cell detachment or abnormal morphology when compared to those cultured with HDPE or under blank culture media (Figures 2.7C, 2.7G, 2.7K and 2.7O). Cells exposed to the cytotoxic control, ZCF, were less spread compared to cells in the blank control. Detachment of the cell monolayer was also observed for the cells exposed to ZCF (Figures 2.7D, 2.7H, 2.7L and 2.7P). A significant change in morphology was observed in the MC3T3s exposed to the cytotoxic control (Figure 2.7D), cells became spherical and detached from the monolayer surface as compared to MC3T3 cells exposed to 180M PPF.

As with the indirect and direct contact tests, the extract test revealed that all cells cultured with HDPE extract or blank media had statistically similar cell metabolic activities compared to those cultured with 180M PPF extract. The cell metabolic activity of cells cultured with 180M PPF were found to be

statistically different ($p<0.05$) to those of the cells cultured with the cytotoxic control, 70% methanol (Figure 2.8). When cultured with the 180M PPF extract the cell metabolic activity levels were found to be 126.5 ± 16.2% (cMSC), 87.2 ± 8.2% (MC3T3), 100.1 ± 32.3% (L929), and 100.5 ± 12.2% (hMSCs).

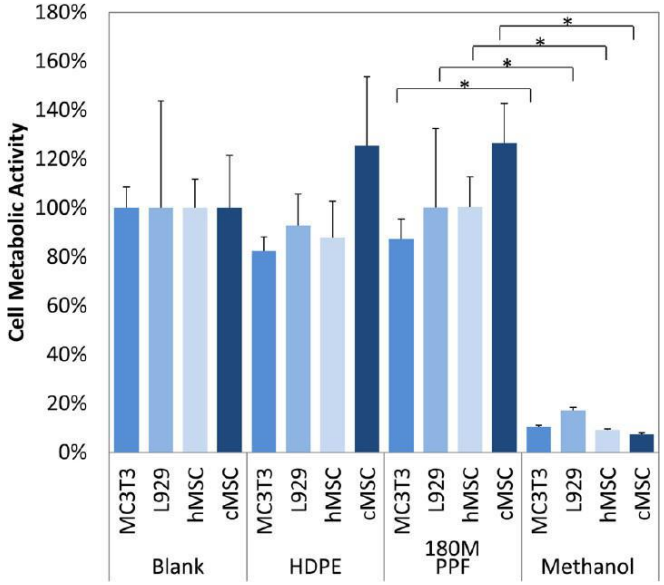

Figure 2.8: Cell Metabolic Activity (Extract) Four different cell populations (MC3T3, L929, hMSC, and cMSC) were cultured in monolayer with extract media of HDPE, 180M PPF, ZCF, or nothing (Blank). Each cell type cultured with 180M PPF extract media was found to have significantly higher metabolic activity when compared to those cultured with the positive, cytotoxic control, methanol ($p<0.05$, * designated a statistical difference between groups). There were no statistical differences found between cells exposed to extract media from 180M PPF, HDPE or under blank culture media.

Fluorescence imaging was used to qualitatively verify cell viability. For all four cell types, no significant morphological changes were observed in cell populations that were incubated with 180M PPF, HDPE and blank media (Figures 2.9A – 2.9C, 2.9E-2.9G, 2.9I-2.9K, 2.9M – 2.9O). All cells exposed to 70% methanol appeared red indicating a significant decrease in viability of the entire population per cell type (Figures 2.9D, 2.9H, 2.9L, 2.9P).

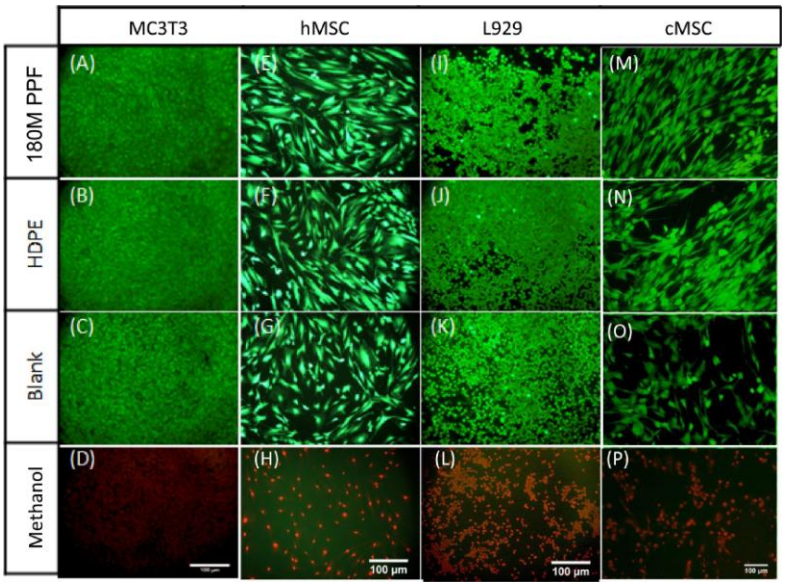

Figure 2.9: Extract Test. Fluorescent images of cells, calcein AM (green) represents live cells, and ethidium homodimer (red) represents dead cells. 8A -8D: MC3T3 cells cultured with (A) 180M PPF (B) HDPE, (C) blank media, (D) 70% methanol; 8E- 8H: hMSC cultured with (A) 180M PPF (B) HDPE, (C) blank media, (D) 70% methanol; 8I -8L: L929 cells cultured with cultured with (A) 180M PPF (B) HDPE, (C) blank media, (D) 70% methanol; 8M -8P: cMSC cells cultured with (A) 180M PPF (B) HDPE, (C) blank media, (D) 70% methanol. Normal morphology was seen in the treatment groups cultured with 180M PPF, HDPE and blank media.

2.4 Experimental Section: Discussions

Cytotoxic effects can hinder the natural assimilation process that is required for successful *in vivo* integration of a biomaterial. The ideal *in vitro* test mimics the *in vivo* physiological environment. This study therefore chose cells to represent tissues that PPF will interact with *in vivo* in various bone tissue engineering therapies along with the cell line suggested per ISO 10993-5.[93, 95] The use of the ISO Standard 10993 allows for the comparison of the biocompatibility of PPF to other biomaterials. Other ISO Standard 10993-compliant cytotoxicity studies have evaluated implanted biomaterials such as electrospun collagen/chitosan nanofibers, poly (ε-caprolactone)/calcium sulfate and hydroxyapatite–ethylene vinyl acetate co-polymer.[234-236] Overall, our study demonstrated that 180M PPF has the same cytotoxic response as a known non-cytotoxic material when cultured with fibroblasts, preosteoblasts and mesenchymal stem cells.

Cellular response to a biomaterial can be impacted by both the crosslinked material and the soluble monomers that may leach out. For PPF, previous studies identified that uncrosslinked monomers of PPF based polymers have low cell viability.[227] We also determined that samples with a high sol fraction with leachable components remaining in the network impacted cell viability negatively. This was primarily seen when these films were not washed with acetone prior to evaluation (UN-30M). The acetone removes the soluble components of the polymer films, leaving only the fully crosslinked network. To evaluate the cytotoxicity of PPF films with high sol fractions, a direct contact test using L929 was performed to compare the 30M, UN-30M, and the 180M PPF films (Figure 2.3). The cell metabolic activities of the UN-30M PPF and the blank culture media were found to be statistically different (Figure 2.3A). With increasing sol fraction and therefore decreasing crosslinking density, a trend of decreasing cell metabolic activity was observed (Figure 2.3A). Cell viability was qualitatively confirmed using live/dead fluorescent imaging. The UN-30M PPF treatment group showed some cell death (Figure 2.3B). To ensure that the cytotoxicity of the crosslinked polymer network was evaluated, and not impacted by

the leachable components, the 180M PPF films were used for the remainder of the direct, indirect and extract tests.

The sol fraction of the 30M PPF films was determined to be 53% compared to the 180M PPF films that had a sol fraction of 3% (Table 2.1). Assuming that the Charlesby-Pinner equation is a representative model of the crosslinking during UV irradiation for PPF, the crosslinking densities were 10% (30M) and 58% (180M). [230] Previous studies have shown that although photocrosslinking of PPF is initiated with BAPO, the crosslinking rate can be augmented with heat.[237] To ensure that sterilization, autoclaving at 121°C, had no impact on sol fraction, the sol fraction was measured pre and post-sterilization**.** Sterilization was found to have no impact, as the sol fraction for the sterilized and pre-sterilized 180M PPF were found to be statistically similar (Table 2.1).

All three cytotoxicity tests demonstrated that the cell metabolic activity of cells exposed to 180M PPF directly (Figure 2.4), indirectly (Figure 2.6), or as an extract (Figure 2.8), were statistically different from cells exposed to the cytotoxic controls. Parallel tests using HDPE and blank culture media showed similar results as to the 180M PPF and were confirmed visually using fluorescence imaging. The greatest cell metabolic activity, a representative of cell viability, was seen in the extract tests; with values as large as 126.5 ± 16. 2% (Figure 2.8) for the cMSCs cultured with PPF extract. Cell metabolic activity levels were normalized using the blank culture media allowing for the possibility of metabolic levels greater than 100% to be achieved. The general trend of cell metabolic activities was lower in the indirect culture test (Figure 2.6) than in the extract test and lowest in the direct culture test (Figure 2.4). These results were as expected, as they followed a general trend of increasing interaction with the materials. The extract test and indirect culture tests provide for no physical interaction of the material with the cell monolayer, whereas the direct culture test allows for the material to be placed directly adjacent to the cell monolayer. The direct contact test also allows for the physical disruption of the cell monolayer, which may increase the cytotoxic impact. These results were acutely present for the tests using ZCF, the cytotoxic control.

Cell death and detachment was greatest in the direct contact tests when cultured with ZCF (Figure

2.5D, 2.5H, 2.5L, 2.5P) compared to the indirect culture test with ZCF (Figure 2.7D, 2.7H, 2.7L, 2.7P). We suggest that this is due to the culture method. There may be some concern that degrading materials may impact cell viability through an increase osmotic pressure. To rule out increasing osmotic pressure as the reason for decreased cell viability during the tests, the osmolality of the direct culture test was measured. The blank media was found to have the highest osmolality (342 ± 5 mOSM) and was statistically different from all other medias. Since there was no documented increase in osmotic pressure after the direct contact test, we believe that the cytotoxicity of the ZCF is due to the direct contact with the material itself, and less the soluble factors released by the ZCF. During the direct contact test the most prominent sites of cell detachment were observed where the cytotoxic material was placed. However, cell morphological changes, detachment, and death were present throughout each cell culture for cells exposed to ZCF.

Comparatively, the cellular response to indirect incubation with ZCF did not elicit massive cell sheet detachment as with the direct contact test. The greatest cytotoxic impact of ZCF was seen directly below the transwell insert. These results are consistent with the expected response due to the localized increased concentration of soluble factors. Direct contact would have a greater concentration of cytotoxic material when compared with indirect contact, where a smaller localized concentration is observed. In indirect contact experiments, the transwell inserts allow for ZCF to sit above the cell monolayer and not contiguous to the cell layer. These results are consistent with the fact that the direct contact test is cited as most sensitive of the three tests utilized.[89, 90, 92]

Of particular interest were the differing responses to the cytotoxic control seen in the four cell types studied. The use of ZCF as cytotoxic control has been established previously for multiple cell types with varying cytotoxic responses.[89, 90, 92, 238] L929 cells had the greatest cytotoxic response to ZCF when compared to the MC3T3, hMSC and cMSC cells. Robust cell death, as well as lifting of the cell sheet, was seen most prominently in the L929 cells after incubation with ZCF. Previous studies have identified the L929 cell line as having a relatively high sensitivity compared to other fibroblasts, epithelial

cells and astrocytes.[89, 90] We expected that both mesenchymal stem cell populations (hMSC, cMSC) would have similar responses to the ZCF as they both are MSC populations from mammals. For both tests using the ZCF the cMSC had a lower cell metabolic activity indicating a stronger cellular response than the hMSCs. Other similarities were expected between the MC3T3 and L929 cell lines, as previous studies established that both MC3T3 and L929 cells had similar cytotoxic responses.[239] However this was not the case for our study. The cytotoxic response during the direct contact test of the L929 cells was statistically different ($p>0.05$) than the MC3T3 cells. For both the indirect contact and extract tests the cell metabolic activities of L929 and MC3T3 are not statistically different. For the indirect culture and extract tests there were no distinctive variation by cell type in responses to the cytotoxic control.

2.5 Conclusion

Cytotoxicity testing, consisting of direct contact, indirect contact and extract testing on multiple cell types was performed to determine the cytotoxic response of cells exposed to PPF in bone tissue engineering applications. For all cell types and cytotoxicity tests, the cell metabolic activity of cells exposed to 180M PPF were found to be statistically different ($p<0.05$) from the cytotoxic control, ZCF, as well as not statistically different when compared to blank culture media and cells recommended by the ISO 10993-5 standard when exposed to the negative control, high-density polyethylene (HDPE). To confirm these results qualitatively, cell morphology, viability, vacuolization and detachment were evaluated. These results confirmed that there was little to no cytotoxic response of cells exposed to PPF. Therefore PPF appeared to not elicit a cytotoxic response under all of the experimental conditions for which it was evaluated. These results demonstrate that PPF has a similar cytotoxic profile to a known non-cytotoxic material (HDPE). Additionally, previous studies have demonstrated that PPF scaffolds can be used for the culture and osteoblastic differentiation of MSCs.[219, 229, 240] We suggest that PPF is a suitable material for bone tissue engineering as it showed a lack of cytotoxic response through its ability to support cell metabolic activity at similar levels compared to HDPE, a known non-toxic material.

Chapter 3: Evaluating 3D Printed Biomaterials: A Novel Approach Using Poly(Propylene Fumarate) Scaffolds

3.1 Introduction

The development and use of three dimensional (3D) printed scaffolds represents a huge opportunity for the regenerative medicine community. However, once a design is created and fabricated, evaluation of what is a successful design for host integration remains a non-standardized process. There is an unmet need for a consistent set of tools to evaluate 3D printed regenerative medicine designs. This study proposes a combined set of methods, or a toolbox, that can be used to identify scaffold designs for enhanced host integration. Our toolbox consists of the following techniques: 1) modular design, 2) micro computed tomography, 3) biocompatibility and mechanical testing, and 4) *in silico* modeling. These methods evaluate scaffolds by first identifying the range of possible designs available for the scaffolds using a modular approach. Then a set of scaffold parameters from within the design space are chosen for fabrication and the 3D printed scaffolds are nondestructively compared to the design specifications. The scaffolds are evaluated for biocompatibility and mechanical attributes, according to well established ISO and ASTM standards. Lastly, they are evaluated for successful host integration by modeling angiogenesis. This approach can be applied to the broad scope of tissue engineered products from conception through development. We illustrate this methodology by applying our toolbox to the design and evaluation of porous 3D printed poly(propylene fumarate) scaffolds.

3D printing represents an accurate (i.e., matches design) and precise (i.e., reproducible) method for the fabrication of porous scaffolds; however, we would like to know the exact limits of scaffold accuracy and the reproducibility of that accuracy. Currently, the most common methods for evaluating scaffold parameters, such as porosity and pore size, are destructive.[13] Therefore, we sought to implement a nondestructive method to evaluate the fabricated scaffold. This method can be used after the initial printing of the scaffold through its lifetime. Evaluation over the scaffold's lifetime allows for the

researcher to understand the impacts of small changes in pore size which may impact cell and tissue ingrowth.[241-244] These small changes in scaffold properties after implantation may also provide clues as to changes in mechanical properties.

Suitable mechanical properties and biocompatibility are necessary characteristics for a successful tissue engineering scaffold. The critical role of mechanical properties over the lifetime of a scaffold is well understood as this is a requirement of many implanted materials. Similarly, guidelines for biocompatibility have been well established to ensure successful native tissue interaction after the material implanted. Since these characteristics are commonly required for many implanted materials, there has been significant research into developing consistent evaluation methods.[95, 245] For this study, we used poly(propylene fumarate) (PPF) as the main polymer resin component to print the scaffold designs. PPF has been thoroughly characterized for its mechanical and biocompatibility properties.[52, 64, 219, 246, 247] Additionally, PPF is biodegradable and photocrosslinkable that has been has shown to exhibit minimal cytotoxicity.[81, 222, 226, 240, 247] Since the biocompatibility and mechanical properties have been well established for PPF we will discuss the other methods which comprise our toolbox to identify the necessary scaffold parameters for successful vessel ingrowth.

Besides providing mechanical stability, successful regenerative medicine scaffolds provide architecture conducive to cell attachment, vascularization and tissue ingrowth.[248] One of the most important factors of successful host integration is the development of a vascular network within the scaffold after implantation.[249] Development of a vascular network has been shown to be successful with porous, degradable scaffold sleeve designs with a lumen.[250] Such a design, like our scaffold design (Figure 3.1), can provide the necessary mechanical support while allowing for proper nutrient and waste transport and vascularization. This hollow, cylindrical design is able to withstand compressive loads within a bone defect when fabricated using a high modulus material like PPF, as well as contain the biological treatment, acting as a delivery vehicle for the biologically active component. Ideally the hollow, cylindrical design is also porous to allow for improved nutrient transport and vessel ingrowth

compared to solid wall designs.

Research suggests that an ideal approach for obtaining precise mechanical and nutrient transport properties is through the use of modular scaffold designs.[251] Modular designs allow for tuning of the scaffold parameters such as pore size and porosity. Specifically, tuning porosity and pore size may be used to control degradation rate and mechanical properties which in turn may be optimized for cell differentiation and neotissue formation.[13] For example, in bone tissue engineering applications, the use of a modular design may allow for the optimization of porosity, while constraining other properties such as elastic strength. Previously, varying pore sizes and porosities within an individual modular design was difficult to achieve when using scaffold fabrication methods such as porogen leaching. This, in turn, made it difficult to decouple the effects of pore properties and mechanical properties. Fortunately, 3D printing has facilitated the fabrication of complex designs at very high resolution, e.g. 15- 60 μm.[1] Modeling the wide range of scaffold parameters available with modular designs allows us to identify the design space in which we can choose the optimal scaffold parameters to best elicit the desire physiological response. These parameters would include pore size, porosity and scaffold dimensions.

The variables of porous designs, such as the pore size and porosity of cell-seeded scaffolds have demonstrated significant roles in successful tissue engineered constructs.[252] In examining bone as an example, we want to promote bone formation and vessel ingrowth, as these parameters greatly influence cell attachment, cell distribution, and cell migration, which in turn affect the cell signaling for osteogenic differentiation.[241] Additionally, pore size and porosity have been shown to impact vascularization and osteoconduction.[219, 242-244] For example, scaffolds with pore sizes of 2 - 6 μm and 33.5 % porosity yielded no bone ingrowth while scaffolds with 30-100 μm pore sizes and 46.9 % porosity yielded 50 μm of osteoid and fibrous tissue ingrowth.[253, 254] Factors such as degradation rate and mechanical stability are highly dependent on pore size and porosity, ultimately affecting bone formation.[241] Similarly, for vascularization, scaffolds with pores greater than 140 μm demonstrated increased functional capillary density compared to scaffolds with smaller pores.[255] Other studies suggest that the rate of

vascularization increases with increasing pore sizes, and at a pore size of 270 μm the potential for scaffold interference in vascularization is removed.[256] Interconnected pores ranging from 300 - 500 μm are known to improve nutrient flow.[250] For some scaffold fabrication techniques, rendering sufficiently accurate pores to obtain specific porosities is difficult, requiring a new approach, such as 3D printing.[252] 3D printing allows for the fabrication of complicated designs with high precision and accuracy. For such designs, a variety of combinations of pore size and porosity can be obtained, allowing for tailoring of degradation rate, mechanical strength, and interconnectivity of the construct. After selecting a set of scaffold designs that are composed of biocompatible materials and have the physiologically appropriate mechanical properties the next step is to evaluate which design optimizes vascularization.

Current methods to measure vascularization use animal models as the gold standard. *In vivo* studies are integral to evaluating the biological response; however, ideally, an *in vivo* study would be implemented at the last stage of development. Identifying the optimal combination of parameters for vascularization earlier in the design process would accelerate the process by reducing the number of designs investigated with each step in the toolbox. Moreover, refinement of the scaffold design prior to the *in vivo* stage is beneficial for implementing the 3Rs of replacement, reduction, and refinement of animal models.[257] Therefore to evaluate vessel ingrowth we suggest the use of an *in silico* model as an integral component of our toolbox. The *in silico* model we recommend has accurately replicated angiogenesis.[256] This *in silico* model allows for the investigation of a wide range of combined scaffold parameters that would be difficult and time consuming recreate the wide range of designs physically. Now that we have identified the steps in our toolbox necessary to examine the wide range of scaffold parameters we applied our methodology to a case study of porous PPF scaffolds.

3.2 Experimental Section: Materials & Methods

3.2.1 Poly(propylene fumarate) synthesis

Poly(propylene fumarate) was synthesized in a two-step process as described previously.[228] Gel permeation chromatography was used to calculate the number average molecular weight (M_n = 866) and polydispersity index (PDI =1.3) of the purified PPF.

3.2.2 Scaffold Design

Scaffolds were composed of repeating units of base rings connected by uniformly distributed c7ylindrical posts (Figure 6.1). These repeating units were stacked to form a porous cylinder (Figure 6.1). This modular design uses a wide range of scaffold parameters such as pore size, post number, post height, base height and wall thickness. From the set of possible designs, twelve were selected as representative scaffolds with three porosities, three pore sizes and two wall thicknesses. These scaffolds were designed using SolidWorks® (Waltham, MA).

3.2.3 Three Dimensional (3D) Fabrication

Four of the twelve designs were 3D-printed using the EnvisionTEC Perfactory® per previously described methods.[1] The resolution was 22.5 μm in the x-y directions and 50 μm in the z direction. Briefly, the polymer resin used to 3D-print the scaffolds was comprised of five components: PPF (38.46 % w/w), diethyl fumarate (DEF) (38.46 %), bis(acyl)phosphine oxide (BAPO) (0.77 % w/w), TiO_2 (0.77 % w/w), and 2-hydroxy-4-methoxybenzophenone, (HMB) (21.54 % w/w). Scaffolds were built at an exposure of 350 mW/dm^2 for 120 s (burn-in) or 60 s per layer. Uncured resin was removed with ethanol and compressed air. Scaffolds were post-cured in a 3D Systems UV-box (Rock Hill, SC) for 12 hours.

3.2.4 Micro Computed Tomography

Micro computed tomography (μCT) was used to nondestructively image and characterize

scaffolds. Scanning was performed on a μCT 100 (SCANCO Medical, Brüttisellen, Switzerland) operated at 70 kvP, 9 μm voxels and 200 mA. The resulting 3D data sets were segmented using thresholds (lower: 35, upper: 188), and gauss sigma (0.8) and support (1) values to separate pores from polymer. Images were compiled and evaluated to calculate pore size, porosity, and wall thickness using Scanco's Image Processing Language (IPL).

3.2.5 Angiogenesis Modeling

Vascularization of scaffold designs was investigated using a previously developed agent-based model[258]. In this model, software agents, representing endothelial cells, are programmed to interact together and with the local environment based on a set of rules, leading to new capillary formation. The rules and specifics were detailed previously.[258] Scaffold structures serve as a steric hindrance to vascular ingrowth.

MATLAB was used to convert scaffold designs into a triangulated mesh and then into a volume matrix. The scaffolds had a final resolution of 1 μm/pixel and were exported as individual volume slices into the model. A representative portion of the scaffold, including a layer of pores and scaffold, was used to reduce computational demands during simulation runs. The scaffolds are modeled as if they were implanted *in vivo,* in contact with skeletal muscle with a uniform distribution of host blood vessels surrounding the scaffold-tissue interface. Each simulation was performed for 400 time steps corresponding to four weeks and repeated 25 independent times for each case.

Multiple parameters were calculated to assess vascularization. Total blood vessel length (TBVL) is the cumulative length of all blood vessels formed. Blood vessel length density (BVLD) is equal to TBVL divided by the number of initial sprouts from host vessels. Average invasion depth (AID) and maximum invasion depth (MID) measure sprout invasion into the scaffold. The ratio of successful sprouts (ROSS) denotes the percentage of initial sprouts which pass the walls into the inner core. Total number of anastomoses (NOA) is how many anastomoses are formed by sprouting blood capillaries.

The simulations were performed using 64-bit versions of Java JDK 1.6.0_10 with Java 3D 1.5.2 and Eclipse Helios version 3.6.2 on a workstation running 64-bit Windows 7 Professional with an Intel Pentium i7 processor and 192GB of RAM. Repast version 2.0.1 was used with parameter sweep feature to perform batch simulation runs.[259, 260] The Java code outputs the 3D position of agents at pre-defined time steps. 3D renderings of scaffolds with blood vessels were produced using open source ImageJ (version 1.46o) visualization software package.

3.2.5 *In Vivo* Study

Animal experiments were performed at Chang Gung Memorial Hospital (Keelung City, Taiwan) with procedures approved by the Institutional Animal Care and Use Committee. A rodent subcutaneous implantation model was used to evaluate vascularization. Four scaffold conditions with 500 µm wall thickness were examined *in vivo* (400 µm and 38 % porosity, 400 µm and 25 % porosity, 800 µm and 50 % porosity, 800 µm and 25 %). Scaffolds were steam sterilized at 121°C for 15 minutes and prepared under sterile conditions. Scaffolds were implanted into subcutaneous pockets created in Sprague-Dawley rats (n=2 per group per time point), under isoflurane anesthesia. Each rat received 4 implants with the implant location determined randomly. At 1 and 3 weeks after implantation the implants harvested with surrounding tissue and then formalin fixed. During implantation, one 800µm pore size, 50% porosity scaffold was damaged so n = 1 at week three.

3.2.6 Histological Analysis

The formalin fixed samples were paraffin embedded and sectioned (5 µm thickness). The tissue orientation resulted in a radial cross section of the scaffold allowing for clear identification of the biomaterial-tissue interface. Sections were stained for hematoxylin and eosin (H&E) and Masson's trichrome for examination of tissue structure and inflammation. Immunostains for CD31 were performed to identify blood vessels as described previously.[261]

3.2.7 Statistics

Statistical analysis was performed using ANOVA and Tukey's multiple pairwise comparison ($p < 0.05$). Values provided are mean ± standard deviation. Please note that only relevant statistical relationships are denoted on figures.

3.3 Experimental Section: Results and Discussion

We applied our toolbox to examine the wide range of scaffold parameters using a case study of porous PPF scaffolds. To utilize this set of tools, we designed, fabricated, characterized, and evaluated porous PPF scaffolds consisting of modular ring-shaped bases. The first step was to use modular design to identify the wide range of scaffold designs that are feasible with defined pore sizes, base heights and number of posts. Of the wide range of variables identified within the range of possible designs twelve scaffold designs were selected, with varying porosities, pore sizes, and wall thicknesses. Eight of the twelve theoretical designs are pictured in Figure 3.1b-3.1i with wall thicknesses of 100 µm (Figure 3.1b - 3.1e) and 500 µm (Figure 3.1f -3.1i). The designs include three different porosities (25 %, 38 %, 50 %), and two pore sizes (400 µm, 800 µm). Figure 1j shows that porosity is increased by varying the height of the posts connecting the modular ring structures. Conversely, modeling the effect of base height on porosities showed that increasing the base height to 500 µm (red), from 100 µm (blue), results in a smaller range of porosities (Figure 3.1j). Figure 3.1k highlights the trend that as the number of posts increases, the range of possible porosities decreases. Conversely, as post height increases, the range of possible porosities increases. A large range of possible porosities and pore sizes is necessary for the wide range of native tissues that regenerative medicine addresses. Of the twelve designs within the range of design specifications, four were chosen for the next steps in the toolbox.

Four of the twelve designs were fabricated using an EnvisionTEC Perfactory® 3 (Perfactory®) from PPF-based polymer resin. This absorbable polymer has been optimized in previous work for 3D printing with high levels of precision.[262] To evaluate the precision and accuracy of the 3D fabricated

designs µCT was implemented as the second step in our toolbox. First µCT was used to nondestructively image the fabricated scaffolds (Figure 3.2a - 3.2d). This µCT data was compared to the design specifications. For each design, the intended pore size, porosity, and wall thickness were compared to their corresponding physical construct parameter (Figure 3.2e). Similar values to the design specification for the porosity were achieved for three of the four scaffolds (Figure 3.2a - 3.2c); however, pore sizes were smaller than the designed values. For the scaffold designs with 400 µm pores, the printed scaffolds had an average pore size 63 % and 70 % of the intended pore sizes. The scaffold design with 38 % porosity, 400 µm pores and 500 µm wall thickness (Figure 3.2d) exhibited the largest deviation from the design, with the porosity at 53 %, pore size at 70 % and wall thickness at 78 % of the design specifications (Figure 3.2e).

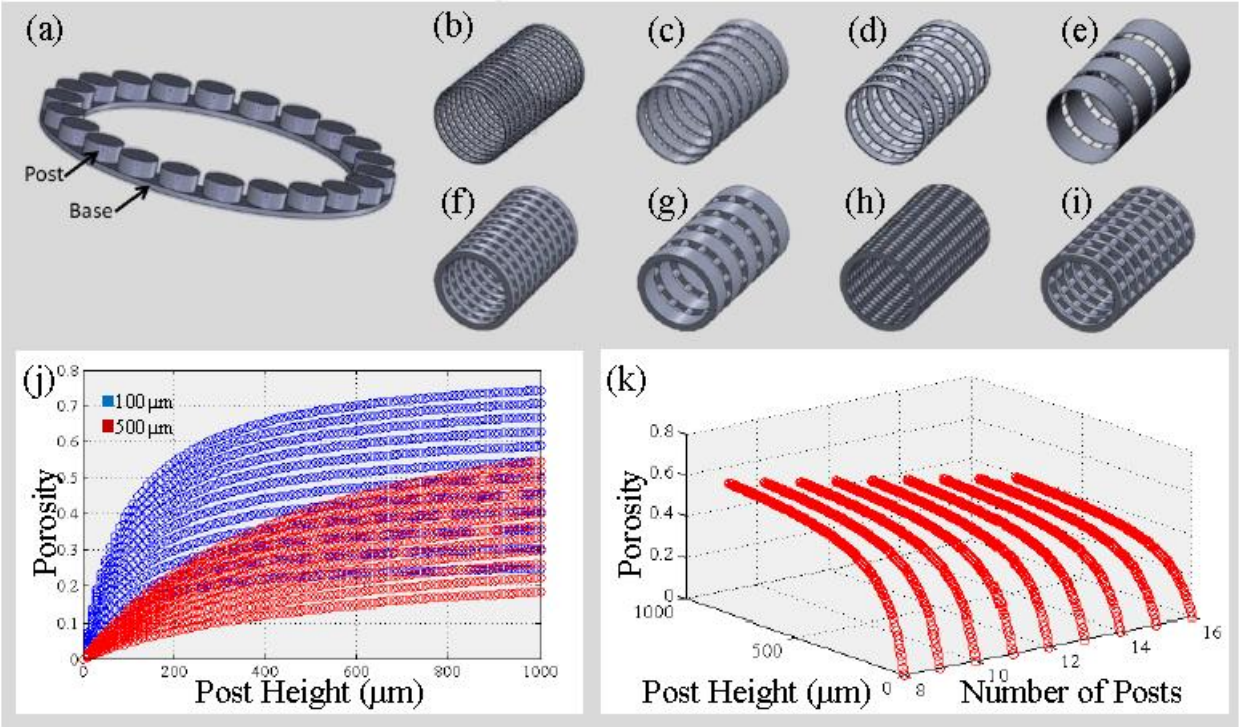

Figure 3.1: Design of Standardized Modular Scaffolds. (a) Repeating Unit of Modular Scaffold Design. Base and post ring structure that is used as the repeating unit to create the scaffold designs. The modular design can be tuned by varying post number, base height and wall thickness to create a range of pore sizes and porosities. (b – e) 100 µm Wall Thickness Scaffolds. (b) 400 µm pore size, 50 % porosity, (c) 800 µm pore size, 25 % porosity, (d) 400 µm pore size, 25 % porosity, and (e) 800 µm pore size, 50 % porosity. (f - i) 500 µm Wall Thickness Scaffolds. (f) 400 µm pore size, 25 % porosity, (g) 800 µm pore size, 25 % porosity, (h) 400 µm pore size, 50 % porosity, and (i) 800 µm pore size, 50 % porosity. (j) Effect of Post height on Porosity. Increasing post height allows for a greater range of porosity. Smaller wall thickness (blue) modular designs allow for a greater range of porosities. (k) Effect of Number of Posts on Post Height and Porosity. As the number of posts increase, the range of possible porosities decreases.

Conversely, the two scaffolds that were most accurately fabricated had 800 µm pores; with porosities that were 88 % and 90 %, pore sizes at 80 % and 70 %, and wall thicknesses of 91 % and 79 % of the design specifications. In comparison with porogen leached scaffold fabrication, which creates pores based on the size distribution of the porogen, the 3D printed pores were printed with a tighter tolerance allowing for greater control of the scaffold parameters.[263, 264] The µCT 3D renderings and quantification of the printed scaffold parameters show promise for the fabrication of complex designs. The greatest design conformance was seen with the wall thickness and the overall porosity; however, the pore size was consistently found to the smaller than the design specification.

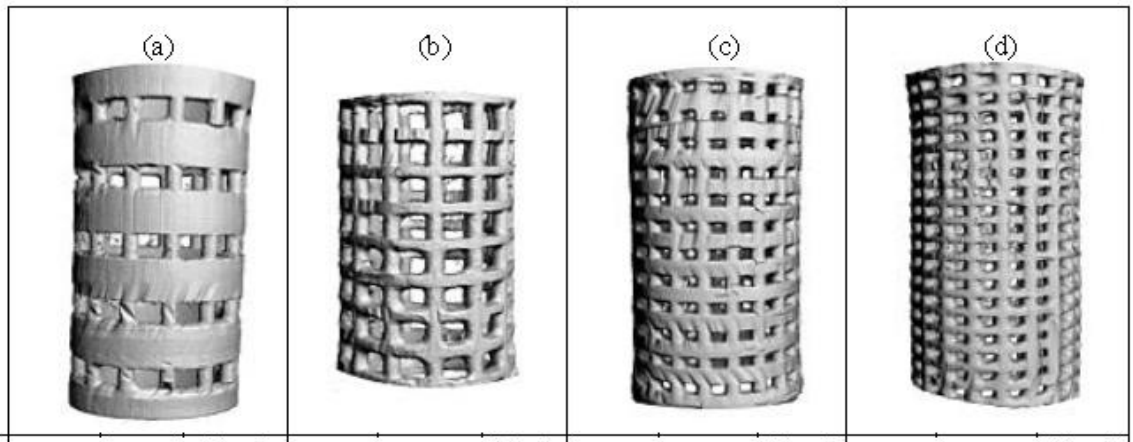

(e)	Design	Actual	% of Design	Design	Actual	% of Design	Design	Actual	% of Design	Design	Actual	% of Design
Pore Size (µm)	800	561± 10	70± 1%	800	636± 118	80± 15%	400	253± 44	63± 11%	400	279± 44	70± 11%
Porosity	25%	22%	88%	50%	45%	90%	25%	19%	76%	38%	20%	53%
Wall Thickness (µm)	500	456± 10	91± 2%	500	39± 11	79± 2%	500	403± 4	81± 1%	500	390± 60	78± 12%

Figure 3.2: µCT Characterization of 3D Printed Scaffolds. (a - d) µCT 3D Renderings of Scaffolds. 3D rendering of scaffold designs. (a) 800 µm pores, 25% porosity, (b) 800 µm pores, 50% porosity, (c) 400 µm pores. 25% porosity, (d) 800 µm pores, 38% porosity. (e) Comparison of 3D Printed Scaffolds with Theoretical Scaffold Design Parameters. Nondestructive analysis of scaffold pore size, porosity and wall thickness was performed using Image Processing Language. Results are compared to the theoretical scaffold design parameters (Design). Printing efficacy was measured by calculating the percent difference between the fabricated scaffold parameters (Actual) compared to the scaffold design parameters (% of Design). 3D printing was most accurate for wall thickness with the closest accuracy at 91% of the design specifications for the 800 µm and 25% porosity scaffold design. Differences between design and fabricated scaffolds were greatest for pore size and porosity. (n = 4)

Overall, the combination of the Perfactory® device and the PPF resin were able to fulfill the desired ranges of porosities and wall thicknesses; however, the pore sizes ranged from 63 % to 80 % of the targeted values (Figure 3.2). The undesired infilling of designed pore spaces and subsequent rounding of the pores, is thought to be due to extraneous photocrosslinking caused by the light scattering effects of the dye, titanium dioxide (TiO_2), and post-curing shrinkage of the polymer.[262] The rounding of the edges is best seen in the scaffold with 38 % porosity and 400 µm pore size (Figure 3.2d). This unintentional curing is referred to as "dark cure" or "over cure".[262] Dark cure is polymerization of polymer due to scattered light in locations where light has not been projected, i.e., the areas we want to

remain dark and uncured. Additionally, high viscosity polymer resins, like PPF, have been shown to negatively impact printing resolution with the undesired filling of pore spaces.[1] Over cure is observed with the crosslinking of the polymer resin beyond the dimensions in the design specification that are perpendicular to the build plate. This highlights some areas of future research for improving the accuracy and reproducibility of 3D printing. Now with the understanding of the dimensions of the fabricated scaffolds we were interested in the potential of angiogenesis of these different designs, or the last step in the toolbox.

We evaluated the potential for vessel ingrowth into the scaffolds using a 3D agent-based model of angiogenesis.[258] This *in silico* model was used, as the last method in our toolbox, to investigate the effect of pore size, porosity, and wall thickness on the rate and depth of vascularization of the scaffolds. Variations of pore size, porosity, and wall thickness exhibited varying levels of vascularization (Figure 3.3). Scaffolds with 200 μm, 400 μm, and 800 μm pore sizes, 25 % and 50 % porosities, and 100 μm and 500 μm wall thicknesses were evaluated for their vascularization potential following implantation *in vivo*. Angiogenesis was assessed using six metrics as described in the methods below (Figure 3.3a). All angiogenesis metrics were found to increase with porosity when other properties (wall thickness, pore size) were held constant.

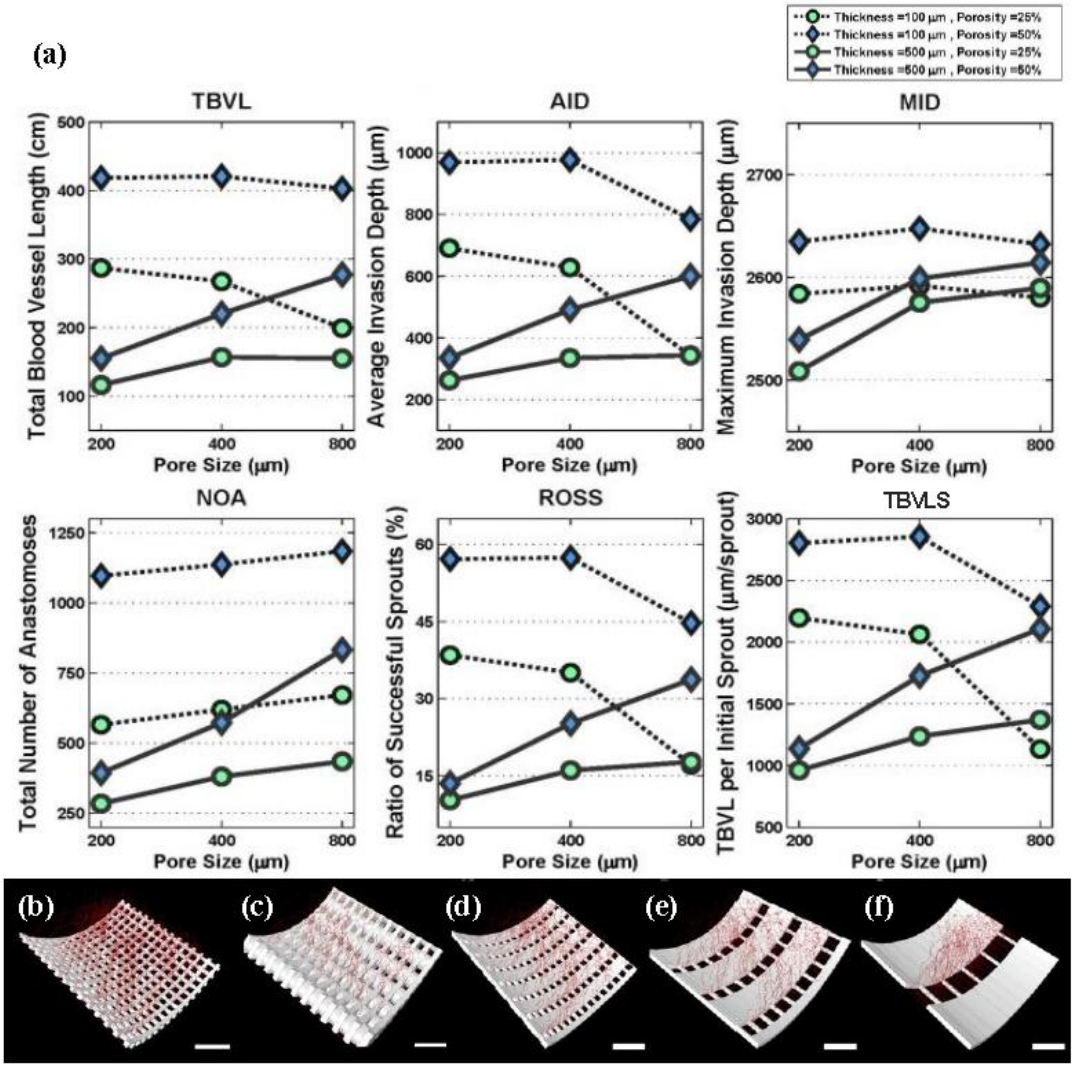

Figure 3.3: In Silico Angiogenesis Modeling Results. (a) Quantitative Results: Angiogenesis of twelve different scaffold designs with two different wall thicknesses and three different pore sizes was evaluated for six different parameters, total blood vessel length (TBVL), average invasion depth (AID), maximum invasion depth (MID), total number of anastomoses (NOA), ratio of successful sprouts (ROSS) and TBVL per initial sprout (TBVLS). Smaller wall thickness, 100 µm, was found to be preferable. At the smaller wall thickness increasing pore size had no impact on ROSS, TBVL or AID. Scaffolds with high porosity (50%), wall thickness of 100 µm and small/medium pore sizes (200 - 400 µm) had the best values for all six vascularization metrics. (b - f) Images of vascularization at 3 weeks. (b - c) Thinner walled scaffolds resulted in greater vascularization, as seen by greater number and length of vessels, correlating with all six parameters in (Figure 3a). Scaffolds shown have 200 µm pore size, 50% porosity, and (b) 100 µm and (c) 500 µm wall thickness. (d - f) As pore size increases vascularization decreases while porosity is held constant. Scaffolds shown have 25% porosity, 100 µm wall thickness and (d) 200 µm, (e) 400 µm and (f) 800 µm pore size. Scale bar represents 100 µm.

We also observed that vascularization decreased with increasing wall thickness. This is clearly seen when comparing the growth of vessels in scaffolds with 100 µm wall thickness in comparison to 500 µm (Figure 3.3b - 3.3c). A greater density and depth of vessels is observed in scaffolds with thinner walls. Interestingly, with 100 µm wall thickness, vascular parameters, such as the maximum invasion depth (MID), ratio of successful sprouts (ROSS), depth of invasion (AID), and total blood vessel length (TBVL), generally decrease with increasing pore size when porosity remains constant. This is highlighted in Figures 3.3d - 3.3f, where the thickness of the scaffold base increases as the pore size is increased to maintain a constant porosity.

One interesting finding is that as pore size increases to 800 µm, wall thickness has less of a detrimental impact on vascularization. This is highlighted in the 800 µm pore size cases, the MID, ROSS, and total blood vessel length per initial sprout (TBVLS) metrics are seen to have similar results for the same size porosity. The effect of very small pore sizes is similar to the effect of very thick scaffolds. In both cases, large surfaces exist in the scaffold which hinder sprout invasion. As a result, when wall thickness is high, increasing the pore size improves the results. However, when wall thickness is low, increasing the pore size has either no effect or a modest negative effect on the ROSS, TBVL and AID (Figure 3.3). As expected, in all cases in this study, increasing porosity has a positive effect on depth and rate of scaffold vascularization. By controlling these scaffold parameters one can influence as well as improve nutrient and waste transport to and from the defect site. In general, agent-based predictions based on the smaller wall thickness of 100 µm showed increased angiogenesis compared to wall thickness of 500 µm (Figure 3.3). In summary, the optimal scaffold designs for vascularization were found to have high overall scaffold porosity (50 %), low thickness (100 µm), and small or medium pore sizes (200 - 400 µm). Along with wall thickness, porosity was shown to play an important role with all six measures of angiogenesis which increase with increasing porosity. These results may be impacted by the difference in surface geometry, where our design facilitates vascular ingrowth into the core, compared to a scaffold that

is a complete cylinder with interconnected pores. These results only take into account the geometric factors influencing angiogenesis, and no biological characteristics so we looked to compare these results *in vivo*.

Vascularization was further investigated *in vivo* by implanting four scaffold designs in a subcutaneous implant model (Figure 3.4). At harvest, the explanted scaffolds appeared intact and were surrounded by a layer of fibrovascular tissue. Histologically, tissue invasion was observed within the scaffold for all conditions. The tissue exhibited a typical inflammatory response with a large density of vessels and significant collagen production. No signs of chronic inflammation, encapsulation, or multinucleated foreign body giant cells were observed. Vessels could be seen growing within the pores of the scaffolds (Figure 3.4c). As seen in Figures 4a and 4b the thin tissue sections include both contributions from the pores and the thick scaffold surfaces that block tissue ingrowth. Vessel density was analyzed quantitatively from CD31 immunostains and similar levels of vessel density were observed in all four scaffolds designs. Similar to the computational predictions vascular networks were observed growing in the pores in all scaffold conditions. However, quantitative analysis of vascular density did not show any differences between conditions (Figure 3.4d) as suggested by the *in silico* model. This suggests the challenges in relating histological findings to 3D structures. The computational model presents an evaluation of the 3D structure that cannot be determined from the essentially two dimensional (2D) tissues sections. Regardless, the results show that the scaffolds enable vascularized tissue ingrowth into the core as suggested by our methods in the toolbox. We suggest that to refine the toolbox to better match physiological outcomes a model of the fabricated scaffold could be evaluated *in silico*; therefore evaluating the scaffolds' true pore size, porosity and wall thickness. Furthermore, the *in silico* data could be compared with *in vivo* results using μCT to better image three dimensionally the vessel penetration of the scaffolds compared to the 2D nature of histology tissue sections.

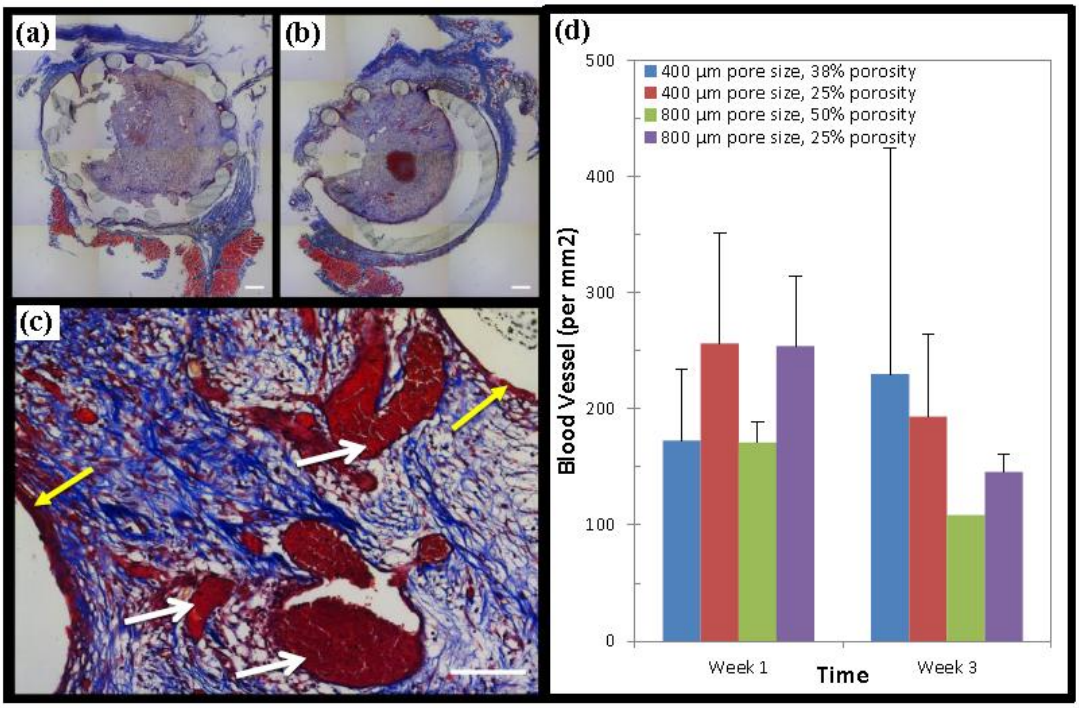

Figure 3.4: *In Vivo* Angiogenesis. (a - c) Histological Analysis of Explanted Scaffolds. (a - b) Massons Trichrome staining showing tissue formation within 500 µm wall thickness scaffolds with (a) 400 µm pore size, 38 % porosity and (b) 800 µm pore size, 25 % porosity. Blood vessels and collagen can be seen between the scaffold posts and within the core of the scaffold. White arrows point to blood vessels. Yellow arrows point to a relatively mild and thin inflammatory response at the interface with the PPF. Blue staining is collagen and shows an overall standard fibrovascular response with collagen formation. Scale bar represents 500 µm. (c) Massons Trichrome staining for pore size of 800 µm, 25 % porosity scaffolds at week 3. Large vessels are seen in the tissue between the posts. Scale bar represents 100 µm. (d) Blood Vessel Density. Vessel density in the tissue growing within the pores of the scaffolds determined from immunohistochemical stains for CD31. There are no statistical differences in vessel density within the pores for these conditions. (n = 2, $p < 0.05$)

3.4 Conclusion

Three dimensional printing allows for the development and use of many complex designs; however, no standard set of tools has been implemented for evaluating the design, fabrication, and implementation of 3D printed scaffolds. Here, we applied our toolbox to predict the best functioning porous scaffold designs for vascularization. Our toolbox was used to investigate the range of possible scaffold parameters using a modular design, to assess nondestructively the accuracy of the 3D printed scaffolds, and to model the potential for vascular tissue ingrowth using an *in silico* model. Since previous studies have investigated the mechanical and biocompatibility properties of porous PPF scaffolds these parameters were not revisited. A modular approach to scaffold design allowed for the specific tailoring of

scaffold parameters such as pore size and overall porosity. After identifying a set of scaffold designs for further study, the scaffolds were printed. Printing efficacy of 3D printing fabrication methods was evaluated using nondestructive μCT imaging. The most accurate fabrication was seen in scaffolds with large pores and small porosities due to decreased incidence of inadvertent rounding in rectangular shaped pores. *In silico* modeling was used to investigate the impact of scaffold parameters on vascularization. An *in vivo* study was used to compare these results and found that all the porous scaffold designs allowed extensive vascularization through the pores and into the core of the scaffold. The use of the toolbox will enable broad improvements in the development and use of 3D printed products for regenerative medicine.

Chapter 4: Structural and Cytotoxicity Evaluation of *In Vitro* Degraded 3D Printed Porous PPF Scaffolds

4.1 Introduction

Understanding changes in structural and mechanical properties, as well as biocompatibility, of absorbable polymer scaffolds during degradation is critical to designing a successful bone tissue repair product. Ideal repair of a bone defect allows for mechanical support while native bone replaces the void. To facilitate rapid repair bone tissue engineering suggests a combination approach of a biomaterial scaffold and a biologically active component. In this study we propose using 3D printed porous poly(propylene fumarate) (PPF) as the biomaterial for the scaffolds. Our scaffolds would provide mechanical stability during degradation while the bioactive material, housed in the lumen, would promote host tissue ingrowth and eventual repair of the bone defect. Another key property of a successful biomaterial is biocompatibility at the implantation site. As PPF is an absorbable polymer, the biocompatibility of PPF depends on both the polymer and its degradation by products. Therefore we investigated the potential for a cytotoxic response to the byproducts of degradation as PPF has already been determined to be noncytotoxic (Chapter 2).

PPF is an aliphatic polyester consisting of a carbon-carbon double bond, flanked by two ester groups that has been determined to be well suited for bone tissue engineering. [52, 219] PPF degrades through the hydrolysis of the ester groups on the repeating unit (Figure 2.1). The byproducts of degradation are fumaric acid and propylene glycol.[226] PPF, and it's degradation byproducts have been shown to be noncytotoxic.[247] Fumaric acid is produced during the citric acid cycle. Therefore *in vivo* it is expected that some of the fumaric acid would naturally be taken up by the cells in the immediate environment. It was established as "practically non-toxic" by the European Commission Report of the Scientific Committee on Animal Nutrition on the Safety of Fumaric Acid. Also, fumaric acid esters have been used for the treatment of severe psoriasis. [265]. The other main degradation byproduct, propylene

glycol is a common food additive.

We hypothesized that the degradation extract of the 3D printed PPF scaffolds will have a low cytotoxic response as its degradation byproducts are nontoxic, and previous research has demonstrated biocompatibility. To test this we proposed a method to evaluate polymer degradation cytotoxicity using a series of extract assays based on the ISO Standard 10993-5, "Tests for In Vitro Cytotoxicity." [95] This is a novel method as the standards for evaluating the cytotoxicity of an absorbable polymer are not well defined for *in vitro* analysis. The scaffolds investigated were 3D printed with a resin containing PPF, diethyl fumarate, vitamin E, and ozybenzone (HMB). Previous studies have evaluated PPF for *in vitro* cytotoxicity and found that it elicits the same cellular response as known noncytotoxic materials (high density poly(ethylene) and blank culture media.[247] The remaining components have also been shown to be noncytotoxic; however, the cytotoxicity of the materials combination as well as during polymer absorption has not been evaluated.[49-51, 88-91, 265] To determine if our scaffolds would fulfill provide the necessary noncytotoxic mechanical support during degradation to treat bone defects, changes in mass, mechanical properties, pore size, porosity, and wall thickness were evaluated over 224 days of degradation.

4.2 Experimental Section: Materials and methods

4.2.1 Poly(propylene fumarate) synthesis

Poly(propylene fumarate) was synthesized in a two-step process as described previously.[228] Briefly, propylene glycol and diethyl fumarate were combined in a 3:1 molar ratio. Zinc chloride and hydroquinone were added in a 0.01:0.002 molar ratio to act as catalyst and radical inhibitor, respectively. The solution was reacted under a flow of nitrogen gas producing ethanol as a byproduct and *bis*(hydroxypropyl) as the intermediate. The second step is a transesterification of the intermediate, performed under a vacuum, to produce PPF with propylene glycol as a byproduct. Gel permeation

chromatography was used to calculate the number average molecular weight (M_n) and polydispersity index (PDI) of the purified PPF. For the solid wall and unaligned pore scaffolds PPF M_n = 1157 Da and PDI = 1.15; for the aligned pore scaffolds M_n = 1078 Da and PDI =1.67

4.2.2 Scaffold Design

Scaffolds were designed based on a modular design described previously (Chapter 6). Briefly, the design consists of a base ring with uniformly distributed posts, this unit is repeated and stacked upon the unit prior until the desired height of the scaffold is reached (Figure 4.2). This cylindrical structure is hollow, designed to house a biologically active (bioactive) component in the lumen. Two of the scaffold designs were porous, one with the pores from each modular unit aligned (aligned). The other porous scaffold was based on the same modular unit; however, each modular unit was rotated when stacked on previous unit. This created a structure where the pores are not stacked one on top of each other, or an unaligned structure (unaligned). The third design was a solid wall design (solid). These scaffolds were designed in SolidWorks® (Waltham, MA).

4.2.3 Three Dimensional (3D) Fabrication and Post Curing

The scaffold designs were 3D-printed using the EnvisionTEC Perfactory® P4 per previously described methods.[1] The resolution was 25 μm in the x-y directions and 50 μm in the z direction. Briefly, the polymer resin used was comprised of: PPF and diethyl fumarate (DEF) in a 1:0.8 ratio along with dyes and initiator. Bis(acyl)phosphine oxide (BAPO) (1%) was used as the initiator and 2-hydroxy-4-methoxybenzophenone, (HMB) (1%) and α-tocopherol (0.01%) were used as dyes. Scaffolds were built at an exposure of 275mW/dm^2 for 120 s (burn-in) or 100 s per layer. Uncured resin was removed with ethanol and compressed air. Scaffolds were post-cured in a 3D Systems UV-box for 2000 flashes. After printing, scaffolds were first rinsed for 15 min in PBS (0.01M) to eliminate any extraneous debris. Then the scaffolds were washed for 30 min in a 50% acetone solution to remove any unreacted resin. Finally

the scaffolds were rinsed 15 min in a PBS solution to remove all traces of acetone. Scaffolds were vacuum dried and their initial mass (M_i) was recorded. Scaffolds were sterilized 15min at 121°C prior to initiating the degradation study.

4.2.4 Sol Fraction

To assess the crosslinking density the sol fraction was measured per the previously described method[52]. Samples of the photocrosslinked film were weighed (W_i) prior to incubation in acetone, the solvent. The samples were then submerged in the solvent for 24 h. After incubation, samples were dried overnight and weighed again (W_d) (n = 3). Sol fraction was calculated using the formula:

$$sol\ fraction = \frac{W_i - W_d}{W_i} x\ 100\%$$

4.2.5 *In Vitro* Degradation

Scaffolds and 20mL of phosphate buffered saline (PBS) (0.01M, pH 7.4) and 0.01M asorbic acid were placed into vials. Ascorbic acid was added to stabilize the scaffold degradation byproducts. Vials were stored at 37°C on a shaker table (75RPM). At each timepoint (days 0, 1, 7, 14, 28, 56, 112, and 224), pH was measured and PBS was replaced. At each timepoint scaffolds were removed from the vials and wet (M_w) weights were recorded. After vacuum drying and dry weight (M_d) was recorded. At each timepoint mass loss, water absorption, pore size, porosity and wall thickness were evaluated (n = 3). Also at each timepoint wet scaffold mechanical properties evaluated using compressive testing (n = 5). Mass loss was calculated using the following formula:

$$Mass\ Loss = \frac{M_i - M_d}{M_i} x\ 100\%$$

Scaffold mean pore size, porosity and wall thickness was evaluated non-destructively using micro computed tomography (μCT) at each timepoint.

4.2.6 Micro Computed Tomography (μCT)

Micro computed tomography (μCT) was used to non-invasively image and characterize changes in scaffolds as previous described (Chapter 6.2.4). Scanning was performed on a μCT 100 (SCANCO Medical, Brüttisellen, Switzerland) operated at 70 kvP, 9 μm voxels and 200 mA. The resulting 3D data sets were segmented using thresholds (lower: 35, upper: 188), and gauss sigma (0.8) and support (1) values to separate pores from polymer. Threshold segmentation values were determined using a peak histogram approach and confirmed visually. Images were compiled and evaluated to calculate pore size, porosity, and wall thickness using Scanco's Image Processing Language (IPL).

4.2.7 Compressive Mechanical Testing

Compressive mechanical testing was performed at each timepoint using an Instron mechanical testing system (33R/4465). At each timepoint scaffolds were removed from PBS and immediately used for wet mechanical testing with the exclusion of day 0 (n = 5). Day 0 testing was performed prior to exposure to PBS. Samples were placed into stainless steel fixtures, which ensured that compression was applied homogeneously. Each fixture had a radius of 7.5mm, an outer ring of 4mm, an inner post of 3mm, and a channel for the sample that was 2mm in width. All tests were performed using a high capacity load cell (5000N). Samples were compressed at a displacement rate of 10 mm/min. Prior to initiating compression, force and displacement were zeroed and then monitored throughout the experiment. Experimental values were recorded every 10 ms.

During testing compression was maintained until a drop of at least 10% in force was measured. Engineering stress and strain were calculated based on cross sectional area and height, respectively, which were then used to compute compressive modulus, 1% offset yield stress, and ultimate, or maximum, compressive stress. Compressive modulus was calculated using Matlab to determine the slope of the linear region of the stress-strain curve. The program evaluated the slope after a preload of 2N. The linear region was then calculated using linear line fit command for the first 10 data points. The program then

continues to add data points in steps of 10 until the $R^2 > 0.97$. The slope of this region is representative of the modulus of the sample. Yield stress was calculated as the intersection of the stress-strain curve with a line, drawn parallel to the initial slope, whose x-axis intercept is shifted 0.01 mm/mm strain.

4.2.8 Cytotoxicity of Degradation Byproducts

PPF scaffolds were degraded in PBS (0.01M and pH=7.4), with 0.01M of ascorbic acid, in a ratio of 6:100 of scaffold to solution based on the ASTM F1635. Extract PBS was removed at days 1, 7, 14, 28, 56, and 112 to evaluate the cytotoxicity of the degradation byproducts. The cellular response to the extract PBS was evaluated using a fibroblast cell line (L929) (ATCC, Manassas, VA) as recommended by the ISO standard 10933-5.[14] Cells were cultured per the manufacturer's specifications with Minimum Essential Medium (MEM) (Life Technologies, Frederick, MD) and 10% horse serum (Life Technologies). Cells were plated and grown to ~80% confluency prior to initiating the assays.

The extract PBS was combined with L929 culture media in three ratios, 1:99, 10:90, and 50:50. The cell culture media was then removed and replaced with the extract and media solution (Figure 4.1). The extract and media solution was incubated at 37°C and 5% CO_2 for 24 h after which the cytotoxicity was evaluated qualitatively with fluorescence microscopy and quantitatively with the XTT cell metabolic activity assay (Roche, Mainheim, Germany). For the cytotoxic control the culture media was removed and cells were incubated with 70% methanol for 30 minutes prior to evaluation of cytotoxicity. Blank culture media was used as a negative control.

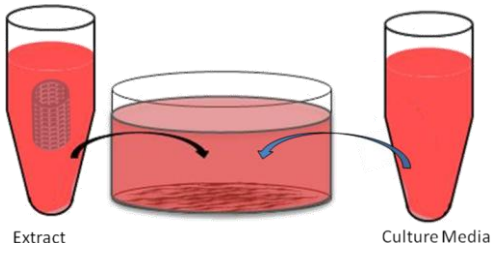

Figure 4.1: Diagram of cytotoxicity test for the degradation byproducts. Culture media was mixed with degradation extract in one of three ratios (1%, 10% or 50% extract) and was used as the culture media for L929 fibroblasts for 24 hours.

4.2.9 XTT Assay

The Cell Proliferation Kit II (XTT) (Roche, Mainheim, Germany) was used to quantitatively evaluate cell metabolic activity. XTT (2,3-bis-(2- methoxy-4-nitro-5-sulfophenyl)-2H-tetrazolium-5-carboxanilide) was used according to the manufacturer's protocols. The electron coupling and XTT labeling reagents were thawed and immediately combined in a 1µl:50µL ratio. Then 250µl of the XTT solution was added to the cell culture wells. Absorbance was measured after 4 hours of incubation at 37°C with a M5 SpectraMax plate reader (Molecular Devices, Sunnyvale, CA). Net absorbance was calculated (A_{492}-A_{650}) for each sample of the biological replicates. Relative cell metabolic activity was normalized to the mean of the blank culture media. Samples were evaluated, the mean cell metabolic activity and standard deviations are reported (n=3).

4.2.10 Fluorescence Imaging

Qualitative evaluation of cell viability was performed using live/dead imaging as described previously[233]. Live/dead solution was prepared (4µM of calcein AM and 2µM of ethidium homodimer in 0.01M PBS) (Invitrogen, Carlsbad, CA). Prior to the addition of the live/dead stain, cells were washed with PBS to remove any remaining culture media and FBS. Cells were incubated with the live/dead solution in dark conditions for 30 minutes prior to imaging. Images were obtained with a fluorescence microscope (Axiovert 40CFL, filter set 23, Zeiss, Thornwood, NY) fitted with a digital camera (SPOT Insight 1120, or SPOT Idea 2920, Diagnostics Instruments, Sterling Heights, MI).

4.2.11 Statistics

Statistical analysis was performed using ANOVA and Tukey's multiple pairwise comparison ($p<0.05$). All tests were performed in triplicate (n=3) unless otherwise specified. Values provided are mean ± standard deviation. Please note that only relevant statistical relationships are denoted on figures.

4.3 Experimental Section: Results

Three scaffold designs, aligned pore, unaligned pore and solid wall, were created and fabricated using 3D printing. Scaffolds were then degraded in 0.01M PBS with 0.01 ascorbic acid at 37°C on a 75 RPM shaker table. Scaffold degradation was seen during the 224 day study through increasing mass loss, decreasing pH as well as changes in scaffold pore size, porosity and mechanical properties. Cytotoxicity of the degradation byproducts was evaluated and found to not elicit a negative cellular response.

Scaffolds were 3D printed with a high degree of accuracy compared to the design specifications (Figure 4.2). The aligned and unaligned porous scaffolds had an effective average porosity of 52% and 53%, respectively, close to the designed porosity of 50%. The scaffold mean wall thickness was fabricated at 532 μm and 558 μm for the aligned and unaligned scaffolds, respectively, compared to the 500 μm design specification. In comparison, the wall thickness for the solid wall scaffolds was fabricated

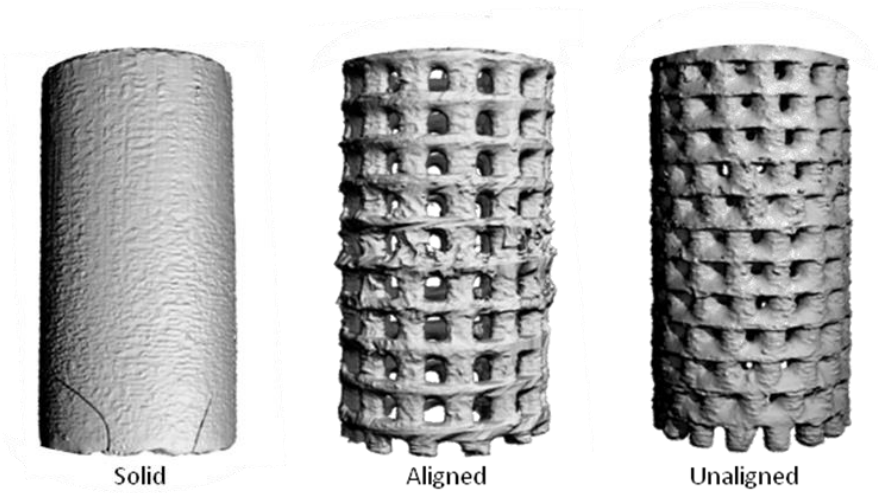

	Theoretical	Effective	Theoretical	Effective	Theoretical	Effective
Porosity (%)	n/a	n/a	50%	52 ± 9%	50%	53 ± 3%
Pore Size (μm)	n/a	n/a	500	619 ± 30	500	569 ± 45
Wall Thickness (μm)	500	842 ± 23	500	532 ± 65	500	558 ± 46

Figure 4.2: μCT 3D rendering and evaluation of scaffold porosity, pore size and wall thickness. All three scaffold designs, solid wall, aligned pore and unaligned pore scaffolds were successfully fabricated using 3D printing. Most parameters of the porous scaffold, aligned and unaligned pore, were fabricated similar to the design specifications. However, the wall thickness of the solid wall scaffolds was found to be larger than the wall thickness of either of the porous scaffolds (n=10).

at 842 µm, much larger than the 500 µm design specification. The printed pores were unexpectedly slightly larger than the desired 500 µm size, with an average pore size of 619 µm, aligned, and 569 µm, unaligned, scaffolds.

Sol fraction was performed to determine if the different scaffold designs had any impact on the amount of crosslinked network (Table 4.2). The sol fraction for all three groups was found to be statistically similar.

Table 4.1: Sol Fraction of Scaffolds

Scaffold Design	Sol Fraction
Solid	12.6 ± 1.7%
Aligned	13.3 ± 8.4%
Unaligned	9.6 ± 3.3%

All three scaffold designs showed degradation during the 224 day study as seen through increases in mass loss and decreasing pH (Figure 4.3). Mass loss increased throughout the study, with the biggest increase in mass loss seen in the first 28 days. After 224 days, the solid wall scaffolds had lost 17 ± 7% of the mass compared to 12 ± 1% mass loss of the aligned scaffolds and 17 ± 2% of the unaligned scaffolds. At each timepoint the solid wall scaffolds had the same or greater percentage of mass loss compared to the porous scaffolds. As one of the degradation products of PPF is fumaric acid we expected to see a decrease in pH as the scaffolds degraded. The lowest pH was seen at day 224, with a range of values from 5.62 ± 0.29 (unaligned), 6.05 ± 0.55 (solid) to 6.21 ± 0.40 (aligned).

(A)

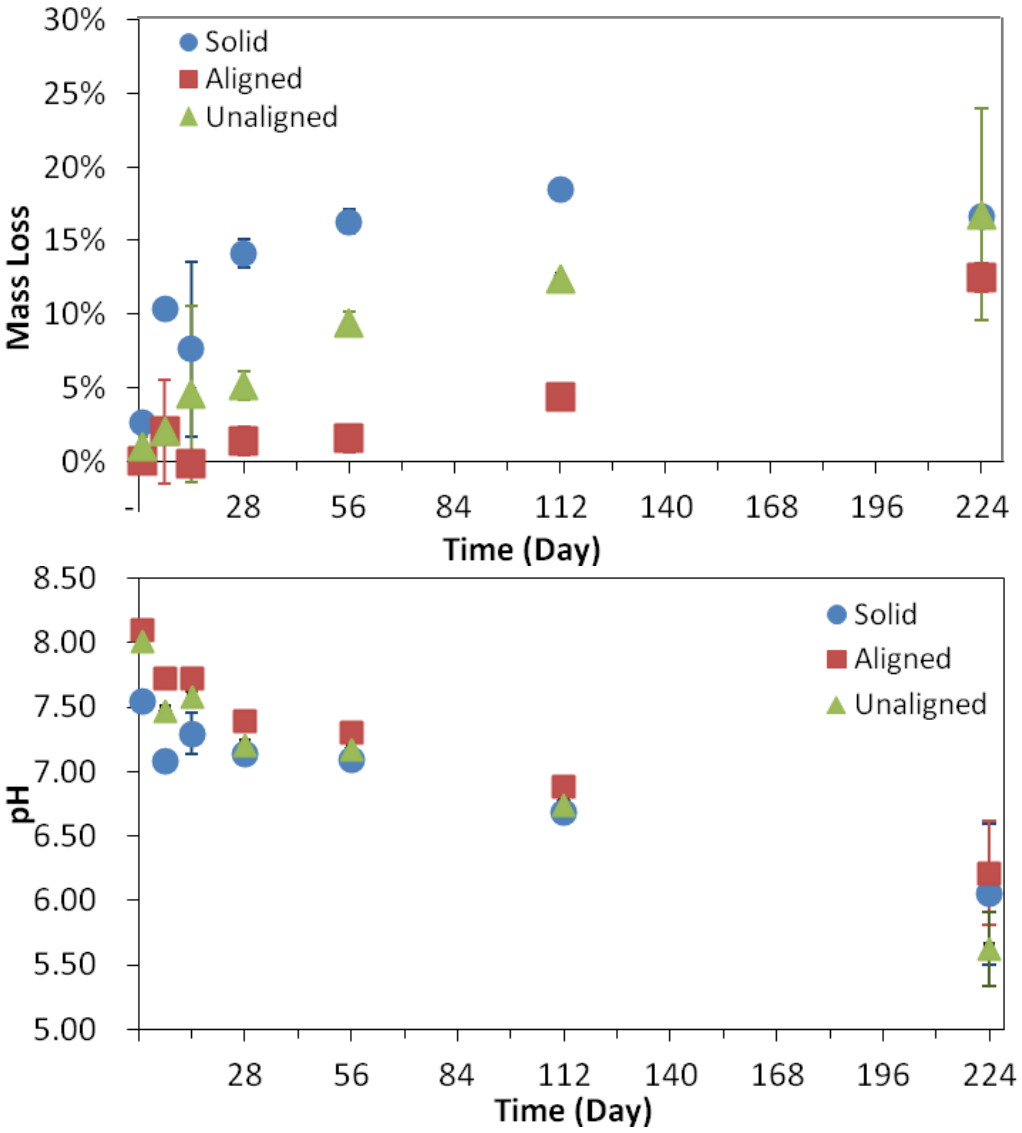

Figure 4.3: Mass loss (A) and pH change (B). Mass loss increases through the 224 day study, indicating that degradation is occurring. Also indicative of degradation is the change in pH, which decreases over the study. The decrease in pH is due to the formation of fumaric acid, one of the degradation byproducts of PPF. The mean and standard deviation are reported, some standard deviations are too small for the error bars to appear (n = 3).

As degradation was shown to be occurring through increasing mass loss and decreasing pH, micro computed tomography (μCT) was used to elucidate how the scaffolds were degrading. μCT was used to evaluate the changes in scaffold pore size, porosity and wall thickness as previously described.[266] Image segmentation of the polymer from the free space was set using a peak histogram

approach. To understand the tolerance of these threshold values data from three threshold sets, [20, 188], [35, 188], and [35, 1000] were used to elucidate the potential impact of alternative threshold values (Table 4.2).

Table 4.2: Impact of Change of Threshold Values on µCT Evaluation of Pore Size, Porosity and Wall Thickness

Threshold	Pore Size (µm)	Change from [35, 188]	Wall Thickness (µm)	Change From [35, 188]	Porosity	Change from [35, 188]
[20, 188]	588.6	4%	537.4	-6%	54%	4%
[35, 188]	612.6	-	508.9	-	56%	-
[35, 1000]	620.8	-1%	511.1	0%	56%	1%

Scaffold porosity was shown to slightly increase throughout the study, while the mean pore size remained statistically the same for the porous scaffolds (Figure 4.4). The average porosity increased from 52 ± 9% and 53 ±3% at day 0 to 64 ± 2% and 57 ± 4% at day 224, for the aligned and unaligned scaffolds, respectively (Figure 4.4A). Average pore size was 619 ± 30 µm and 569 ± 45 µm at day 0 compared to 634 ± 25 µm and 573 ± 13 µm at day 224 for the aligned and unaligned scaffolds, respectively (Figure 4.4B). A trend in wall thickness shows a decrease in size as the study progressed for the porous scaffolds (Figure 4.3C). The solid wall scaffolds also showed a decrease in wall thickness with the wall thickness at day 0 being statistically larger than all other timepoints (Figure 4.4C).

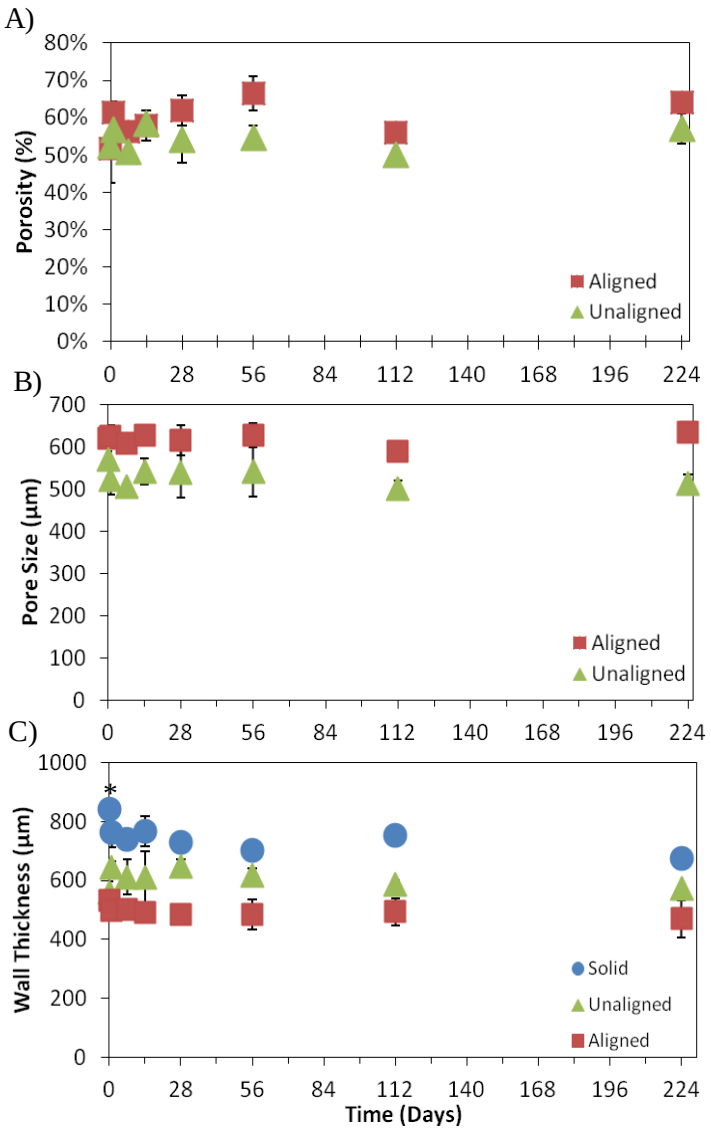

Figure 4.4: Porosity (A), pore size (B) and wall thickness (C). µCT was used to calculate the porosity, pore size and wall thickness of the scaffolds during the study. Porosity (A) is seen to increase slightly from day 0 to day 224, while mean pore size remains constant (B). Similarly, there is no statistical difference in wall thickness for the aligned or unaligned scaffolds. The solid wall scaffolds wall thickness decreases over the study, with a statistically larger wall thickness on day 0 compared to all other timepoints. The mean and standard deviation are reported, some standard deviations are too small for the error bars to appear (n=3). * denotes $p<0.05$ from all other timepoints within the same group.

To investigate how the porosity was increasing while average pore size remained constant a histogram of pore sizes was evaluated for each of the porous scaffolds. Figure 4.5 is an example of the

histograms of pore sizes at four different times during the study, day 1, day 28, day 56 and day 224, for the aligned pore scaffolds. The green box highlights that as the scaffolds degrade we see the emergence of a population of small pores, less than 150 µm, which we refer to as surface pores and micropores.

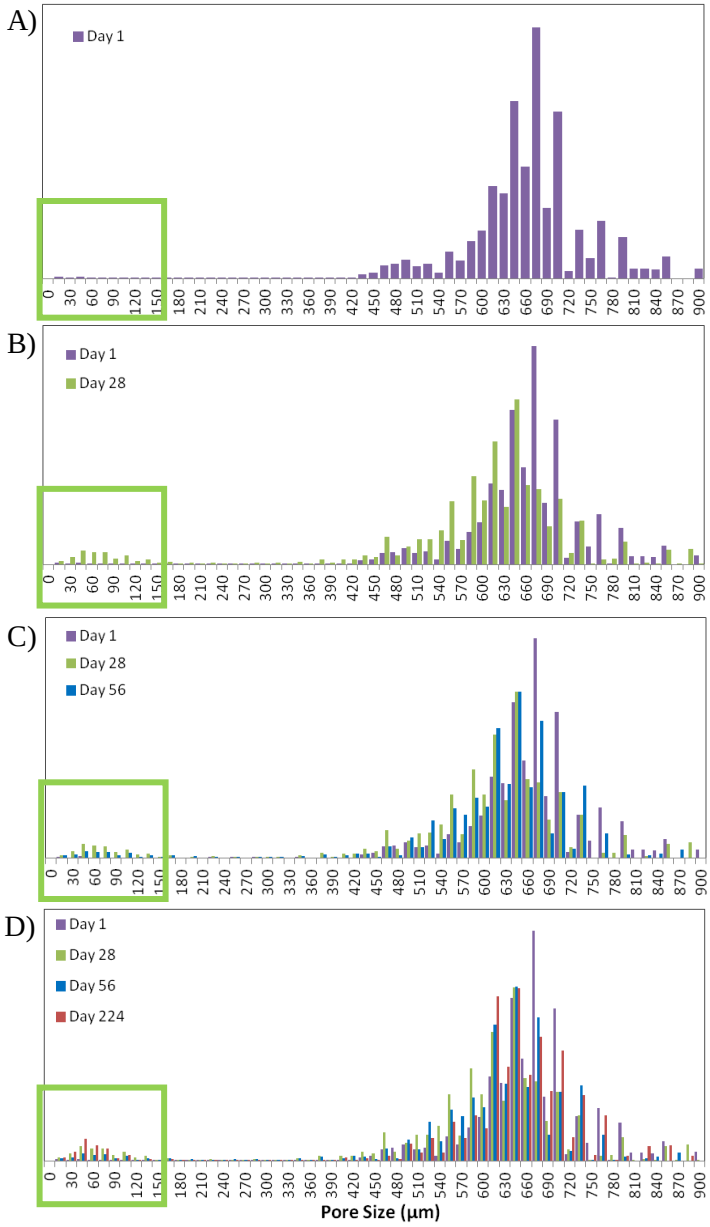

Figure 4.5: Histogram of aligned pore scaffold pore sizes during degradation. (A) Day 1, histogram of pore sizes, there are very few pores < 150 µm (population highlighted in the green box). (B) Day 28, a small population of pores <150 µm begin to emerge. (C) Day 56, the trend continues with additional small pores, along with some larger small pores, showing the propagation of surface pores. (D) Day 224, the population of small pores continues to grow as scaffold degradation occurs.

μCT was used to produce 3D renderings at each timepoint of the study to visualize the degrading scaffolds(Figure 4.6). Figures 4.6A – 4.6D are representative samples of the aligned scaffolds as it degraded, these scaffolds were also used to produce the histograms for Figure 4.5. As the scaffolds degrade we can see both the emergence of surface pores but also an increase in surface roughness. This is highlighted in the change in the surface of the solid wall scaffolds as they degrade (Figure 4.6C). In comparison, the aligned pore scaffolds have the greatest number and depth of surface pores of the three scaffold designs.

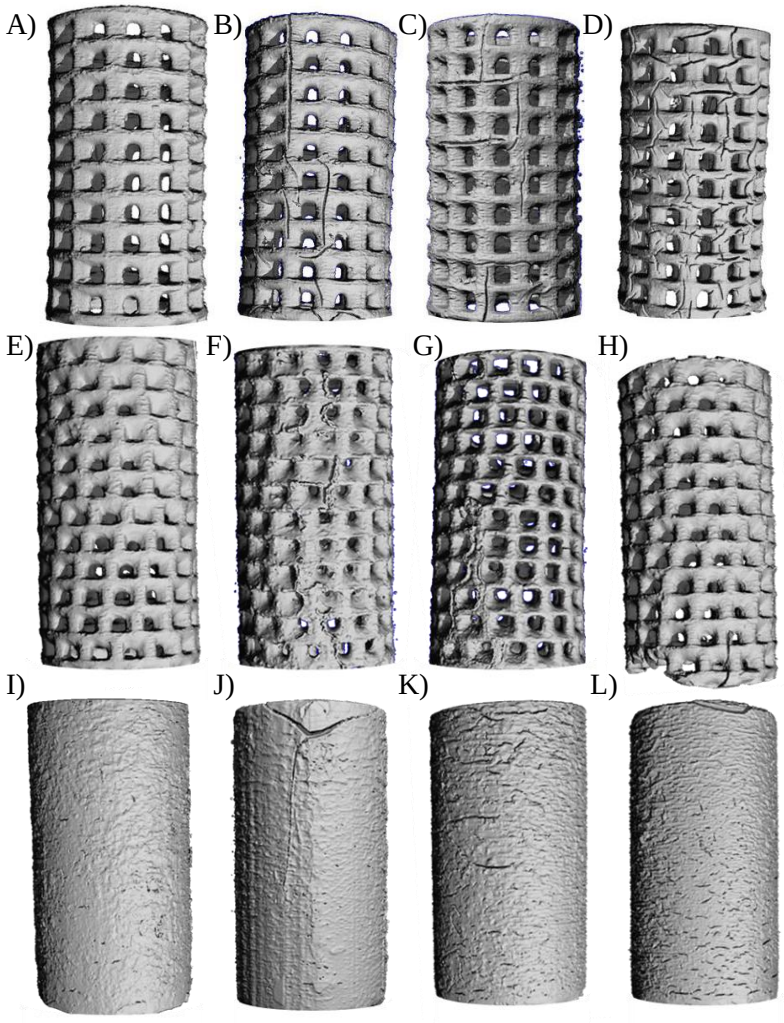

Figure 4.6: μCT 3D Rendering of Scaffolds During Degradation. (A-D) Aligned scaffolds at day 1 (A), 28 (B), 56 (C) and 224 (D). Surface pore formation can be seen with increasing number and length as the study progressed. (E-H) Unaligned scaffolds at day 1 (E), 28 (F), 56 (G), and 224 (H). Small number of surface pores and increase in surface roughening can be seen over the course of the study. (I-L) Solid wall scaffolds at day 1 (I), 28 (J), 56 (K) and 224 (L). Degradation can be seen with the formation of smaller surface pores as well as increased surface roughening at day 224 compared to the previous timepoints during the study.

Also seen during degradation was the emergence of a population of micropores which could be seen on the μCT pore map (Figure 4.7B, Figure 4.7D). As seen in the figure, the smallest pores, or micropores are seen in dark blue. Also seen in dark blue are the surface pores Figure 4.7B. Fewer surface pore formation was seen on the unaligned scaffolds compared to the aligned pores. The dark blue pixels represent the smallest pores on the pore map. As seen in Figure 4.7A and 4.7B the majority of dark blue pixels are formed by surface pores. Where as in the unaligned pore scaffolds, the majority of the dark blue pixels are in the form of micropores as seen in Figures 4.7C and 4.7D.

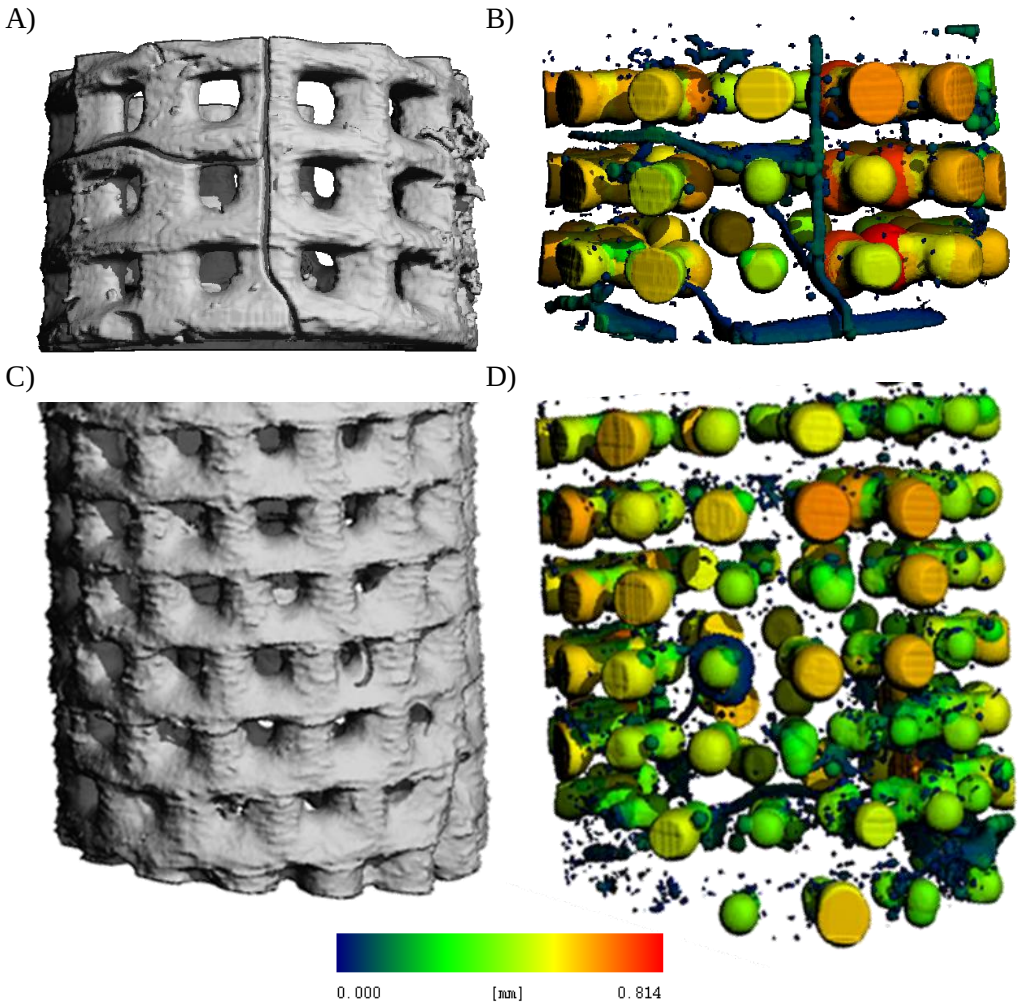

Figure 4.7: μCT 3D Renderings and Pore Maps. (A) Bottom section of aligned pore scaffold 3D rendering (B) Pore map of (A) used to visualize pores in scaffold. (C) Bottom section of unaligned pore scaffold 3D rendering. (D) Pore map of (D). Dark blue pores are present in the aligned scaffold mainly as surface pores where as in the unaligned pore scaffold the dark blue pores are seen as micro pores throughout the scaffold and are not visible on the surface.

To investigate the impact of scaffold degradation on mechanical properties compressive mechanical testing was performed (Figure 4.8). The maximum compressive load was found to not be statistically different from other another at any timepoint during the study for the porous scaffolds (Figure 4.8A). Similarly, the yield for the porous scaffolds was found to be statistically the same over the degradation study (Figure 4.8B). The solid wall scaffolds were found to have statistical

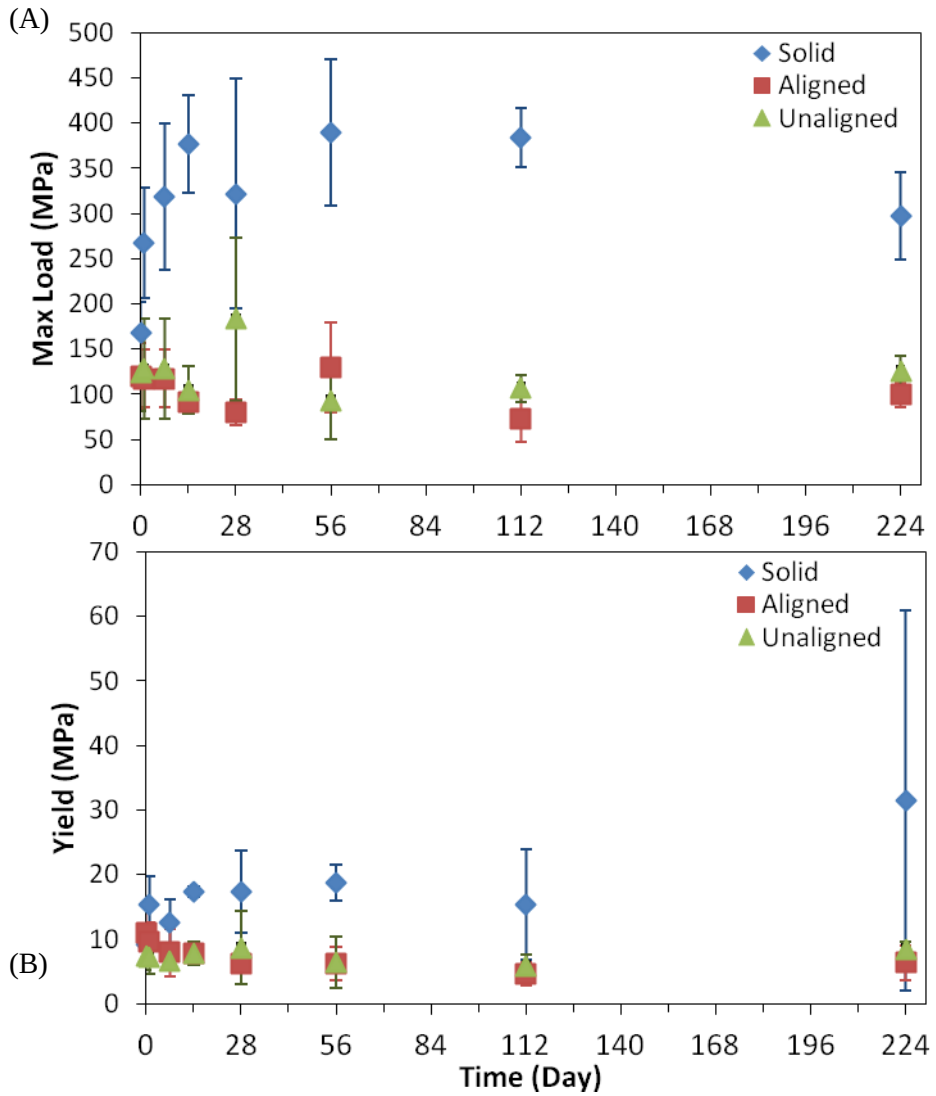

Figure 4.8: Wet Compressive Mechanical Testing Maximum Load (A) and Yield (B) during degradation. Porous scaffolds do not demonstrate any statistical differences in mechanical properties during the study. Solid wall scaffolds were seen to have a statistically higher yield at day 224 ($p<0.05$, n =5 per timepoint) and a statistically lower maximum compressive load when dry, at day 0 ($p<0.05$, n = 5 per timepoint).

differences in yield and maximum compressive during degradation. The yield was found to increase over the study with a statistically higher yield at day 224; whereas, the maximum compressive load was found to be statistically higher at day 0 compared to all other timepoints. Also evaluated was the wet compressive modulus. For both porous scaffolds the modulus at day 224 was not statistically different from the modulus at day 0. However at days 56 and 112, the aligned pore scaffolds had modulus statistically lower than the modulus at day 0 (Figure 4.9).

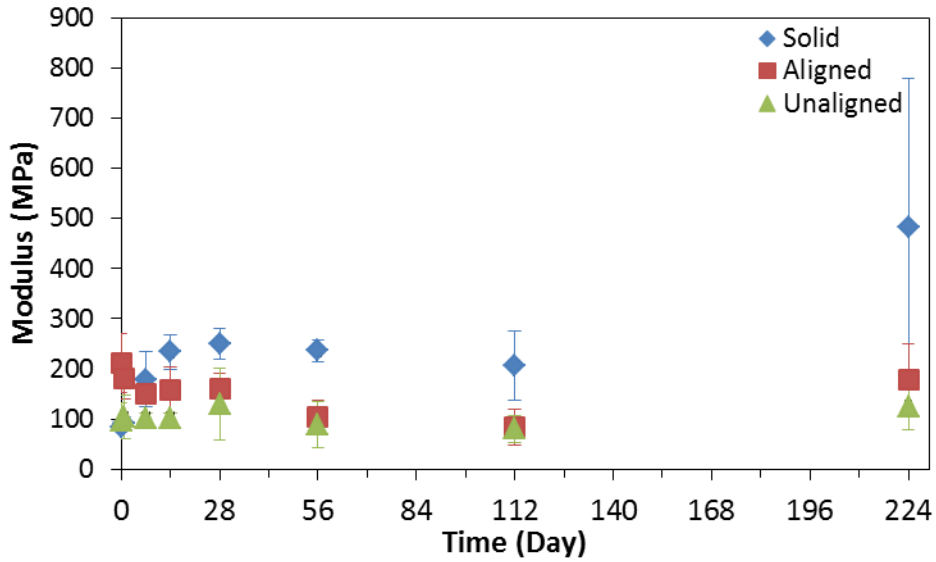

Figure 4.9: Wet Compressive Mechanical Testing. Modulus of solid, aligned and unaligned scaffolds over the 224 day study. For the aligned scaffolds day 56 and 112 had statistically lower moduli than the day 0 timepoint; however, by day 224 the moduli returned to statistically similar to day 0. For the unaligned scaffold there was no statistical difference between timepoints.

Cytotoxicity of the degradation byproducts was performed for timepoints at day 1, 7, 28, 56 and 112. Fibroblast cells (L929) were incubated with the extract PBS and cell culture media in three different ratios. The three ratios evaluated are C1 (1% PBS, 99% cell culture media), C2 (10% PBS, 90% culture media) and C3 (50% PBS, 50% cell culture media). Cell metabolic activity levels after 24 h of incubation was calculated using XTT. The three different concentrations of degradation PBS to cell culture media, C1, C2 and C3 were found to be statistically different from the positive control 70% methanol (Figure 7.11). At day 14, C1 and C3 were found to be statistically different, as well as on day 56, the blank and C3 were found to be statistically different. In all timepoints but day 14 the cell metabolic activity levels

were statistically similar between all concentrations of extract and culture media (Figure 4.10).

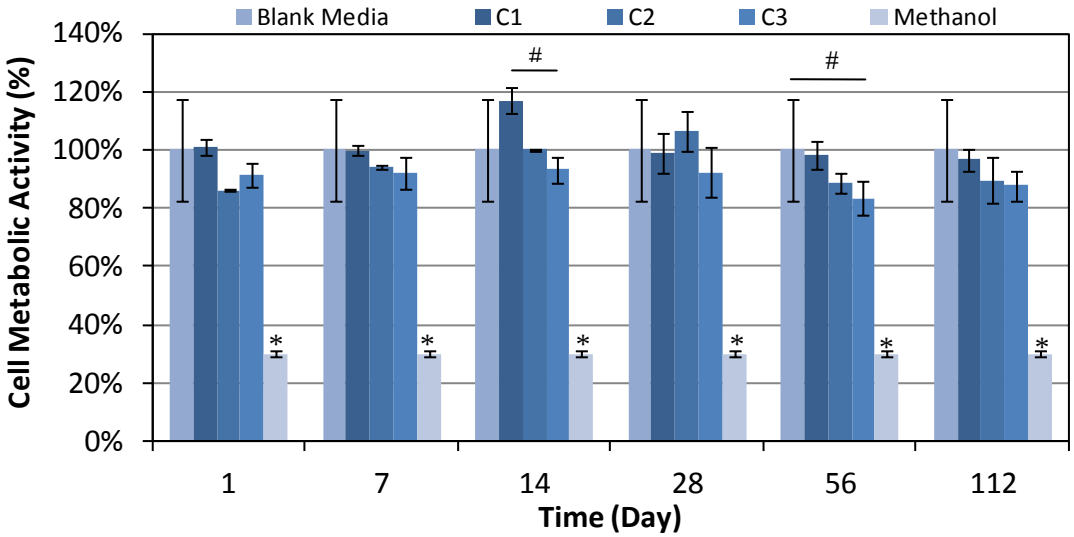

Figure 4.10: Cell Metabolic Activity Levels. Fibroblast cells (L929) were cultured with a mixture of degradation extract and cell culture media in one of three ratios of extract: media. C1: 1% extract: 99% media, C2 10% extract: 90% media, or C3 50% extract: 50% media. Cell metabolic levels were compared with metabolic activities from cells cultured with blank media, or a toxic control, 70% methanol. * denotes statistical difference within the timepoint (day) ($p<0.05$). # denotes statistical difference ($p<0.05$) (n=3)

Fluorescence imaging was used to qualitatively verify the cell viability. For all timepoints, no significant morphological changes were observed in cell populations that were incubated with the three different ratios of extract and culture media (Figure 4.11A-4.11F) compared to the cells incubated with blank culture media (Figure 4.11G). Cells exposed to 70% methanol appeared red indicating a significant decrease in viability of the entire population per cell type (Figures 4.11H).

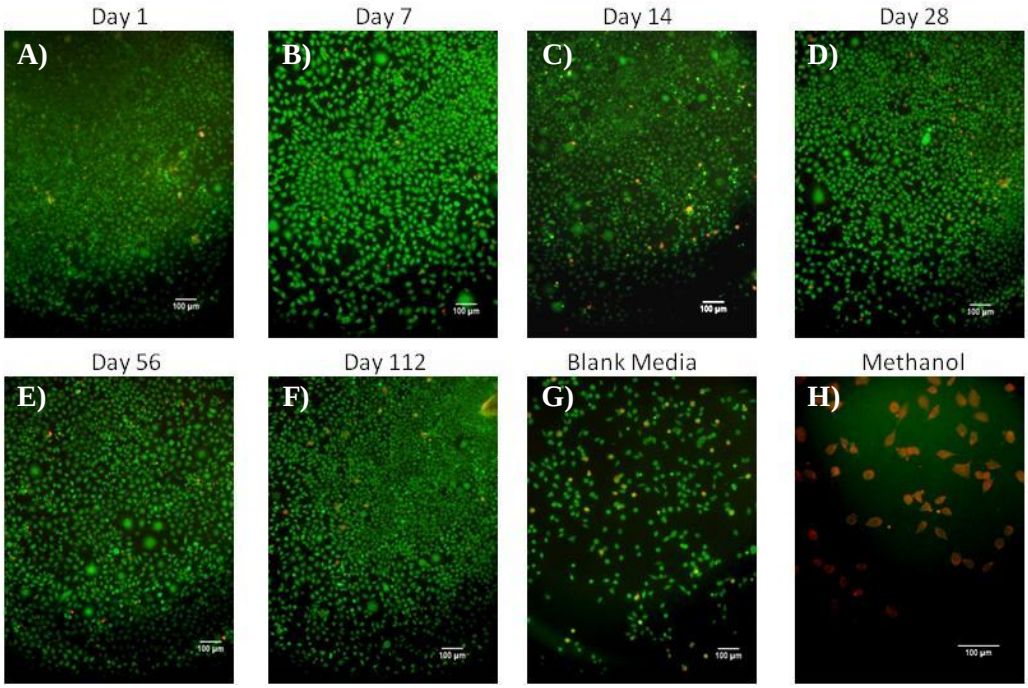

Figure 4.11: Cytotoxicity of Degradation Byproducts. Fluorescent images of L929 fibroblast cells after 24 h of incubation with media and degradation extract, where calcein AM (green) represents live cells, and ethidium homodimer (red) represents dead cells. Images are of those cells cultured with 50% extract and 50% culture media (C3 concentration). No significant changes in morphology are present when compared to the blank media control. Cells were incubated with 70% methanol as the toxic control. Scale bars represent 100 µm.

4.4 Experimental Section: Discussions

Three scaffold designs, aligned pore, unaligned pore and solid wall, were successfully fabricated using 3D printing. A 224 day, or 32 week, degradation experiment was then performed to evaluate how these scaffolds degrade and the impact on the scaffold's mechanical properties. Also investigated was the potential cellular response to primarily the degradation byproducts, fumaric acid and propylene glycol. The motivation was to determine which scaffold design would provide long term mechanical stability

during degradation without eliciting a cytotoxic response. This long term mechanical stability would allow for the scaffold to function as a delivery vehicle for a bioactive material that is loaded into the lumen of the porous-walled scaffold. This scaffold would ideally provide the mechanical support to a bone defect while the bioactive material, such as stem cells encapsulated in a hydrogel, would facilitate new bone and vessel in growth into the defect.

Previous studies have evaluated the use of PPF-based polymer networks to treat bone defects. PPF has been well characterized for bone tissue engineering as it's mechanical properties fall within the range of bone.[226] Other modifications to PPF, such as additional co-polymers and additives have been investigated to enhance the mechanical properties of this already strong polymer.[52, 222] Our previous research investigated the use of a PPF, DEF based polymer resin.[266] The addition of DEF to PPF creates a stronger crosslinked polymer network with higher compressive yield and modulus.[52] However, this PPF and DEF based resin previously caused extraneous crosslinking when used in a 3D printing system so additional dyes and inhibitors were investigated to improve the accuracy of the fabricated scaffold to the design specifications (Chapter 3). The previous PPF based resins was modified with the replacement of TiO_2 with HMB and vitamin E. This polymer resin provided a reduction in extraneous crosslinking (see Chapter 3.1) and improved the accuracy of the 3D printing (Figure 4.2). Previously the extraneous crosslinking led to smaller pore sizes and porosities compared to the design specifications; conversely our scaffolds had larger pores and greater porosities than the design (Figure 4.2).

Two of the designs were porous, with either aligned or unaligned pores, were formed using a modular design (Chapter 3.1, Figure 3.1). The modular design is based on a repeating unit comprised of a ring, or the base, with cylindrical posts extending from it. The pores are formed as squares and were designed to be 500 μm. 500 μm was chosen since previous fabrication had a reduction in pore size of 150 – 250 μm from the design specifications. Therefore we wanted pores between 250 – 500 μm. Originally the optimal pore size was believed to be approximately 100 μm, due to cell size; however, now many

studies have shown that pore sizes of 100 – 350 μm promote greater cell migration and vascularization.[13, 267] Additionally, previous studies have shown that for scaffolds with pores larger than 270 μm, it is as if there is no scaffold to hinder the vascularization process.[256] Studies have also shown that interconnected pores ranging from 300 - 500 μm may improve nutrient flow.[250] Porous scaffold designs would allow for nutrient and mass transfer from the native tissue to the lumen of the scaffold; however, it was unknown how these scaffolds functioned during degradation, which design would be best able to provide long term mechanical stability to allow for bone repair while degrading.

Sol fraction was calculated to determine if scaffold design would impact degree of crosslinking. The scaffolds were found to have sol fractions of 12.6 ± 1.7% (solid), 13.3 ± 8.4% (aligned), and 9.6 ± 3.3% (unaligned) (Table 4.1). Sol fraction was found to be statistically similar among the three groups demonstrating that the fabrication methods were consistent between the different designs.

Degradation was observed through mass loss and change in extract pH (Figure 4.3). Previous studies have shown that porous PPF scaffolds see a mass loss of 18 – 30% over a 32 week period. [226] During the 224 day, or 32 week, study the scaffolds lost 12 ± 1 % (aligned), 17 ± 2 % (unaligned) or 17 ± 7 % (solid wall) of their initial mass (Figure 4.3). These mass loss values are similar, although smaller, to those in previous *in vitro* PPF degradation studies.[226] The mass loss may have been smaller since these scaffolds had a hollow lumen and would have a reduced surface area exposed compared to a porous cylinder scaffold. These results were within the expected ranges of mass loss and indicated that degradation was occurring.

To better understand how degradation was occurring, μCT was used to evaluate changes in scaffold wall thickness, porosity and pore size (Figure 4.4). Interestingly, there were no statistically significant changes in mean pore size or wall thickness; however, there was a significant increase in porosity from the initial printing (Day 0) to Day 224 (Figure 4.3). Visually, surface pore formation could be seen throughout the timepoints, with increasing number and length as the degradation study progressed in the μCT 3D renderings (Figure 4.6). This was especially prevalent with the aligned pore scaffold group

(Figure 4.6A-4.6D) compared to the unaligned (Figure 4.6E- 4.6H). The unaligned pore scaffolds did have an increase in the <150um pore population as the study progressed but were mainly formed as micro pores (Figure 4.7). Other degradation could be seen in the increased surface roughening as seen in the solid wall scaffolds (Figure 4.6I – 4.6L). As these pores are smaller than the printed pores, the increase in number and frequency would be expected to impact the mean pore size, which is expected to lead to an average pore size that remains constant while the scaffolds are degrading. To clarify the changes in pore size during degradation a histogram of pore sizes for the scaffolds at each timepoint was compiled (Figure 4.5). A population of micropores and surface pores began to emerge along with the visual emergence of these changes of the scaffold during the degradation timepoints. The histograms are those for each of the aligned scaffolds in Figure 4.6A- 4.6D. Interestingly, neither the emergence of surface pores, nor the micropores were found to have an impact on the mechanical properties over the 224 day degradation study (Figure 4.8). These results for the maximum compressive load and the yield were found to be statistically the same throughout the study (Figure 4.9). Throughout the degradation study the porous scaffolds demonstrated compressive moduli larger than average trabecular bone.[226] This is a key finding, as in order to treat bone defects the scaffolds must provide long term mechanical support during degradation. This was confirmed; however, just as integral to successful defect repair is the cytotoxicity of the scaffold used to treat the defect.

As changes in mechanical and structural properties are integral to understanding the incorporation of the scaffold in a bone defect, also integral for successful integration is scaffold and host tissue compatibility. To this end, it is critical to ensure that byproducts of scaffold degradation did not elicit a cytotoxic response. Currently few standards (ASTM F1635, ASTM F2902, ASTM F1983) evaluate cytotoxicity of absorbing polymers.[268-270] There are few standards that have set forth testing guidelines for *in vitro* analysis although it is pertinent to any implantable, absorbable material, such as the many that are used in tissue engineering. To address this lack, we developed a novel method to evaluate cytotoxicity of degradation byproducts over an extended time frame. This method is based it off two

standards, the ISO standard 10993-5 for extract testing, and the ASTM standard F1635.

As PPF hydrolytically degrades it produced propylene glycol and fumaric acid [271]. This is important as one indication of degradation of polyesters is a decrease in pH as seen in the study (Figure 4.2). However this decrease in pH did not impact cell viability even at the lowest pH ranges evaluated at day 112. Cell metabolic activity levels and live dead fluorescent imaging confirmed that as PPF degrades it does not elicit a cytotoxic response (Figure 4.10, Figure 4.11). The cell metabolic activity levels for all three concentrations of degradation extract and cell culture media were found to be statistically different from the dead control, 70% methanol. Additionally, in all timepoints but day 56, the three concentrations were statistically similar to the blank media control. On day 56, C3, the highest extract exposure condition was found to be statistically different from the blank media control; however, it still was statistically different from the positive control. In all timepoints, but day 14, the three concentrations had statistically similar cell metabolic activity levels. At day 14 the middle concentration (C2) had a statistically lower cell metabolic activity level than C3. All of the most concentrated exposure groups (C3) demonstrated cell metabolic activity levels similar to the blank culture media. These results were confirmed with fluorescent imaging, images of cell viability after 24 h of exposure to C3 are shown in Figure 4.11. No changes in cell morphology or number were seen after 24 h of exposure to the degradation extract and cell culture media solutions. Overall, our study demonstrated that the degradation byproducts did not elicit a cytotoxic response and had the same cytotoxic response as a known non-cytotoxic solution, cell culture media, when cultured with fibroblasts.

4.5 Conclusion

PPF porous scaffold degrade slowly and provide the necessary mechanical properties for the treatment of cancellous bone defects. This slow degradation and stable mechanical properties would allow for the delivery of a bioactive material, to enhance the treatment of bone defects. Degradation is seen through both bulk mass loss and the formation of surface pores and micropores. These surface pores and

micropores are best seen nondestructively with μCT evaluation. Increased surface roughing, caused by surface degradation, was also observed during the 224 degradation study. The degradation byproducts from the hydrolysis of the polymer network, and forming pores, were shown to not elicit a negative cellular response when cultured with fibroblasts. These results indicate that porous PPF scaffolds, whether with aligned or unaligned scaffolds, would be suitable for bone tissue engineering.

Chapter 5: Hydroxyapatite Doped Alginate Beads as Scaffolds for the Osteoblastic Differentiation of Mesenchymal Stem Cells

5.1 Introduction

Bone tissue engineering has developed a variety of promising approaches to improve the healing efficiency of bone defects and fractures. Numerous studies have used a cell-loaded scaffold approach in which a scaffold having similar mechanical properties of bone is implanted into a defect and carries a population of cells capable of differentiating into bone. Hydroxyapatite (HA), a form of calcium phosphate, is frequently used as a component in these cell-loaded scaffolds. Current research has identified the tubular perfusion system (TPS) bioreactor as enhancing late-stage osteoblastic differentiation of human mesenchymal stem cells (hMSCs) when encapsulated in alginate beads. This work investigates the formation of small alginate beads doped with hydroxyapatite, and their impact on osteoblastic differentiation of hMSCs that are encapsulated within the hydroxyapatite - alginate matrix under dynamic culture conditions using the tubular perfusion system (TPS) bioreactor.

The TPS bioreactor may be used to enhance osteoblastic differentiation prior to implanting a scaffold for bone tissue engineering. The TPS is a novel elegant bioreactor that provides for the long term culture of hMSCs when encapsulated in alginate beads.[78] Previous studies have identified the use of the TPS as a novel design that is easy to sterilize and assemble. The TPS bioreactor consists of growth chambers, where cell-laden polysaccharide alginate beads are cultured, a media reservoir, and a tubing circuit. The polysaccharide alginate used in the TPS bioreactor is crosslinked using calcium chloride. I*n vivo* the alginate network is expected to slowly degrade due to the slow exchange of the calcium ions in the physiological environment.[272] Also, alginate beads have been shown to be biocompatible, facilitate three dimensional transfer of nutrients and signaling molecules, and serve as protection from the host immune response [50].

Studies using the TPS bioreactor have focused elucidating its role in the osteoblastic

differentiation of hMSCs for the treatment of bone defects.[78-81]The TPS bioreactor has been shown to enhance late osteoblastic differentiation *in vitro*. Previous work with the TPS bioreactor identified the use of smaller diameter beads having an increased rate of proliferation (2.0mm) but a decreased rate of osteoblastic differentiation compared to larger diameter beads (4.0mm).[273] This work looks to fabricate small diameter alginate beads containing HA to enhance osteoblastic differentiation. One advantage of HA stems from its similarities in composition and structure to native bone.[40] HA is a commonly used material with degradable polymers as it provides desirable surface roughness and the ability to adhere directly to the bone.[46] The addition of HA has also been used to increase material stiffness, which in turn may improve osteoblastic differentiation.[83] The objective of this work was to develop a method to reproducibly fabricate small diameter hydroxyapatite-doped alginate beads and demonstrate increased osteoblastic differentiation of hMSCs encapsulated in these beads during dynamic culture.

5.2 Materials and Methods

5.2.1 Human Mesenchymal Stem Cell Culture

Human mesenchymal stem cells (hMSCs) were used throughout the study. The hMSCs (passage < 6) from a single donor (Lonza, Walkersville, MD) were cultured, as previously described and per the manufacturer's protocol, with hMSC media, consisting of Dulbecco's Modified Eagle Medium (DMEM) (Life Technologies), supplemented with 10% fetal bovine serum (Life Technologies), 1.0% v/v penicillin/streptomycin (Life Technologies), 0.1 mM non-essential amino acids (Life Technologies).[231, 232, 274] Cell culture took place on tissue culture polystyrene flasks (Corning) under 5% CO_2 at 37°C, with media changes every four days. Upon the start of the cell-based studies, hMSC media was switched to osteogenic media, hMSC media supplemented with 100 nM dexamethasone (Sigma, St. Louis, MO), 10 mM β-glycerophosphate, and 173 μM ascorbic acid. Dynamic culture was carried out in the TPS bioreactor system, while the static controls were cultured in 6-well plates. Comparison of HA:alginate

beads of different compositions was carried out over 7 days under static culture conditions. Comparison between dynamic and static cultures was carried out for 21 days.

5.2.2 Preparation of Alginate Beads and hMSC Encapsulation

2.0% w/v solutions of alginate were prepared by dissolving alginic acid sodium salt from brown algae in 0.15M NaCl and 0.025M HEPES in deionized water. The alginate solution was then sterilized via autoclave under a 15-minute liquid sterilization cycle. Alginate solutions were then aseptically filtered through a 0.8µm syringe filter to ensure solution homogeneity. For non-cell containing beads, alginate solutions were dropped into a stirred solution of 0.1 M $CaCl_2$ using a syringe pump (Harvard Apparatus) at a rate of 6.6 ml/minute using a 10 ml syringe and a 25 gauge needle (Becton Dickinson) suspended approximately 4.5 cm above the surface of the $CaCl_2$ solution. Alginate beads immediately began cross-linking in solution and were allowed to crosslink for 15 to 30 minutes to ensure full cross-linking. Hydroxyapatite beads were created using the above method by suspending HA microparticles (Berkeley Advanced Biomaterials) in the 2% w/v filtered alginate solution. HA was sterilized by ultraviolet light in a biosafety cabinet for at least 12 hours. HA ratios were determined based on %w/v with respect to the solution. For example: a 50:50 HA:alginate ratio solution would consist of 2 g alginic acid sodium salt dissolved in the above solution, followed by the addition of 2 g hydroxyapatite by vortexing. HA:alginate beads were prepared using the same method as pure alginate beads.

hMSCs were removed from culture using Trypsin/EDTA and pelleted at 500 x g for 5 minutes. The cell pellet was resuspended in alginate or HA:alginate solutions at a density of 1x106 cells/mL. After suspension of the pellet in alginate, beads were formed using the methods described above, washed in hMSC media for a minimum of 15 minutes before initiating culture conditions.

5.2.3 TPS Bioreactor Setup

The TPS bioreactor was setup as described previously.[275] Briefly, growth chambers were

attached to media reservoirs using a series of platinum cured silicone and Pharmed BPT tubing (Cole Parmer, Vernon Hills, NJ). Growth chambers were made from larger diameter platinum cured silicone tubing; 6.4 mm inner diameter and 11.2 mm outer diameter and approximately 13 cm in length. Platinum cured silicone tubing is steam sterilizable and allows for oxygen and carbon dioxide (CO2) gas exchange. Pharmed BPT tubing with high mechanical durability was used to interface with the pump head. The tubing circuit system was assembled outside of the biological safety cabinet (BSC) and was sterilized via autoclave for 30 minutes at 121°C. Once sterilized the system was assembled aseptically in the BSC. Alginate and HA:alginate beads were loaded in the growth chambers and pulsatile media was perfused using an L/S Multichannel Pump System (Cole Parmer) at 1mL/minute for the alginate dynamic group and one HA:alginate dynamic group. A second group of HA:alginate beads were cultured in a separate pump at a 2mL/minute pulsatile flow. Polyproplyene mesh #50 (Ted Pella, Redding, CA) was used to retain the alginate beads within the growth chamber. The TPS was housed in an incubator maintained at 37°C and 5% CO_2 for the duration of the study.

5.2.4 hMSC Isolation from Alginate Beads

To isolate hMSCs from alginate beads, beads were incubated in 0.1M ethylenediaminetetraacetic acid (EDTA) for 15 minutes at 25°C. After 15 minutes hMSCs were centrifuged at 500 xg for 5 minutes to form a pellet and resuspended in PBS. Cells were then pelleted and washed once with PBS to remove any remaining EDTA and culture media. A final pelleting provided the cell pellets for assays.

5.2.5 Mass Loss and Water Absorption

Non-cell containing beads at each HA:alginate ratio and an alginate control were massed after 48 hours of suspension in hMSC media. Beads were massed immediately after removal from media then dried in a vacuum oven for 4 days prior to final massing. This difference in mass was used to calculate the water content of the beads. The difference in mass between the day 0 and the time point was used to

determine mass loss.

5.2.6 Swelling of Alginate and HA Alginate Beads and Microscopy

In order to determine how much beads will swell over time in media, a swelling study was conducted on the beads. The amount of swelling indicates the volume of space inside the beads available for cell proliferation. Beads at each ratio were placed in 6 well culture plates in media for 28 days. Media was added every 4 days to maintain the initial media volume. At each time point, bead diameter was measured in suspension using a light microscope at 2.5x objective. Diameter was measured using a 3 point circle approximation via SPOT imaging software. Calibration was obtained using a hemocytometer and determined to be 278 pixels = 1 mm. A histogram frequency distribution of bead diameters was obtained for each ratio of HA:alginate beads (n = 25). Bin size = 43.95 μm.

5.2.7 Scanning Electron Microscopy

Characteristics of hydroxyapatite microparticles were verified using a scanning electron microscope (SEM) (JEOL JSPM-4500A, courtesy Maryland MRSEC). UV sterilized and unsterile samples were mounted onto the specimen mounts. Samples were visualized at 3.0 kV under various magnifications. Imaging was performed at the UMD NISP center.

5.2.8 Fluorescence Imaging

Live/dead imaging was performed to qualitatively evaluate cytotoxicity as described previously.[276] A live/dead solution was prepared with 4 μM of calcein AM (Invitrogen, Carlsbad, CA) and 2 μM of ethidium homodimer (Invitrogen, Carlsbad, CA) in PBS. Prior to the addition of the live/dead stain, cells were washed with PBS to remove any remaining culture media or methanol. Cells were incubated with the live/dead solution in dark conditions for 45 minutes prior to imaging. For the cytotoxic control, cells were incubated with 70% methanol for 30 minutes prior to the addition of the live/dead solution. Images were obtained with a fluorescence microscope at 2.5x objective (Axiovert

40CFL, filter set 23, Zeiss, Thornwood, NY) fitted with a digital camera (SPOT Insight 1120, or SPOT Idea 2920, Diagnostics Instruments, Sterling Heights, MI) and with an inverted TE2000-E microscope (Nikon, Melville, NY) outfitted with a CoolSnap HQ2 (Photometrics, Tucson, AZ) digital camera.

5.2.9 Alkaline Phosphatase Expression

The intracellular ALP protein level was assayed using a p-nitrophenyl phosphate liquid substrate system (pNPP) (Sigma-Aldrich, St. Louis, MO). Chromogenic substrate, p-nitrophenyl phosphate is then used to quantify phosphatase enzymes. ALP activity can be detected using a standard spectrophotometer by the distinct color shift from colorless to a yellow shade following reaction of NaOH with pNPP to form p-Nitrophenol. Cells were isolated from alginate beads as described above and Mammalian Protein Extraction Reagent (M-PER) (Thermo Fisher, Pittsburgh PA) was used to lyse cells. The lysate was then centrifuged at 14000 x g for 15 minutes and 75 µL of supernatant was diluted to a total volume of 310 µL with PBS. The solution was placed in a clear-bottom 96-well plate, mixed with pNPP, and incubated for 30 minutes in the dark. After the reaction was stopped using 2 M NaOH the absorbance of the reacted substrate is detected at 405 nm using a microplate reader. A standard curve using 4-nitrophenol was used as a reference to quantify the concentration of the consumed pNPP substrate. The calculated alkaline phosphatase (ALP) protein levels were normalized with DNA content, measured using a PicoGreen® kit.

5.2.10 DNA Quantification for Proliferation

Cells were isolated from the alginate beads with the addition of 0.1 EDTA for 15 minutes. Cell pellets were then used for DNA isolation with DNeasy Tissue Kit (Qiagen, Valencia CA) following standard protocols. PicoGreen®, a fluorescent nucleic acid stain for quantitating double-stranded DNA, was used to quantify the amount of DNA present in each group. A serial dilution, negative control and the DNA from each of the treatment groups were plated on a 96-well black fluorescent plate and incubated at room temperature for 2-5 minutes. The fluorescence was excited at 480nm and emission was read at

520nm using a microplate reader. DNA concentrations were calculated based on the standard curve of λ DNA provided in the PicoGreen® kit.

5.2.11 Quantitative Reverse Transcriptase Polymerase Chain Reaction (qRT-PCR)

A phenol-chloroform extraction technique was used to isolate RNA from the cell pellets. Briefly, Trizol reagent, solution of phenol and guanidine isothiocyanate, (Life Technologies) was used to resuspend the cell pellets and incubated at room temperature for 5 minutes. Chloroform (Sigma) was added to 16% v/v into the Trizol suspension, shaken vigorously, and the solution was centrifuged at 4°C, 12000 x g for 18 minutes to separate the phases of extracted products. The clear upper aqueous phase contained the RNA. 200µL of the supernatant was vortexed with an equal volume of 70% ethanol, and the resulting solution was used in RNA extraction. RNA extraction was performed using RNeasy Mini Plus Kit (Qiagen, Germantown, MD) per manufacturer's protocols. RNA was then translated into cDNA using cDNA Archive Kit (Applied Biosystems, Foster City, CA). cDNA was then combined with Universal Master Mix (Applied Biosystems) and oligonucleotide primers and Taqman Probes (Applied Biosystems). The table below (Table 5.1) shows the Taqman Applied Biosystems assay IDs for primers and probes for the genes of interest as the sequences are proprietary. The reaction was conducted on a 7900HT Fast Real-Time PCR System Prism 7000 sequence detector (Applied Biosystems). The thermal profile was 2 min at 50 °C, 10 min at 95 °C, 15 s at 95 °C (40 cycles), and 1 min at 60 °C. Relative gene expression changes were calculated using the ΔΔCt method as previously described.[219] GAPDH was used as the endogenous control gene. Fold changes in gene expression are observed and reported as mean values with standard deviations (n = 3).

Table 5.1: Applied Biosystems Taqman Assay IDs for ALP, BMP-2, GAPDH, OCN and OPN

Protein	Assay ID
ALP	Hs00758162_m1
BMP-2	Hs00154192_m1
GAPDH	Hs00960641_m1
OCN	Hs01587813_g1
OPN	Hs00960641_m1

5.2.11 Histology

Alginate and HA:alginate beads were histologically stained for visual verification of matrix deposition. Beads were fixed in 4% paraformaldehyde for 2 – 4 h followed with an overnight soak in 0.1M sodium cacodylate trihydrate and 10mM $CaCl_2$ buffer. Beads were then dehydrated and prepared for paraffin embedding using a tissue processor, TP1000 (Leica Biosystems, Buffalo Grove, IL). The TP1000 prepared the samples using a series of ethanol washes to dehydrate the sample then the samples are washed with Citrisolv (Fisher Scientific) and then soaked in melted paraffin. Beads were then embedded in paraffin and sectioned to 5 μm. Sections were then placed on glass slides (SuperFrost, Fisher Scientific), air dried overnight, warmed on a slide warmer for 10 minutes until the paraffin became translucent, and oven dried for > 1 h at 37°C. Samples were deparaffinized using citrisolv and rehydrated in ethanol. Samples were then evaluated for calcium deposition using Von Kossa staining as described below.

5.2.12 Von Kossa Staining

Von Kossa staining was used to visualize calcium deposition with nuclear fast red as a counterstain to identify cell nuclei. Sections were washed 3 times with distilled water, incubated with 5% silver nitrate solution under ultraviolet light for 20 minutes and then washed with distilled water. Unreacted silver was removed with a 5-minute soak in 5% sodium thiosulfate. Slides were placed in 0.1%

nuclear fast red- 5% aluminum sulfate solution for 5 minutes and rinsed with distilled water. Samples were then dehydrated and cleared using citrasolv. Silver nitrate stains for calcium salts resulting in black or brownish-black deposits, and nuclear fast red stains cell nuclei red and the cell cytoplasm pink.

5.2.14 Statistics

Statistical analysis was performed using ANOVA and Tukey's multiple pairwise comparison ($p<0.05$). All tests were performed in triplicate (n=3) unless otherwise specified. Values provided are mean ± standard deviation. Please note that only relevant statistical relationships are denoted on figures.

5.3 Experimental Section: Results

5.3.1Characteristics of Hydroxyapatite Microparticles

Hydroxyapatite was visualized using SEM. There was no difference in morphology between the non-sterile and UV-sterilized group. Microparticle diameters ranged from 3.55µm to 46.7µm, with an average diameter of 20.6 ± 9.35 µm (n = 30). Figure 5.1 shows the nanoscale surface morphology of the particles, a representative particle, and a distribution of particles.

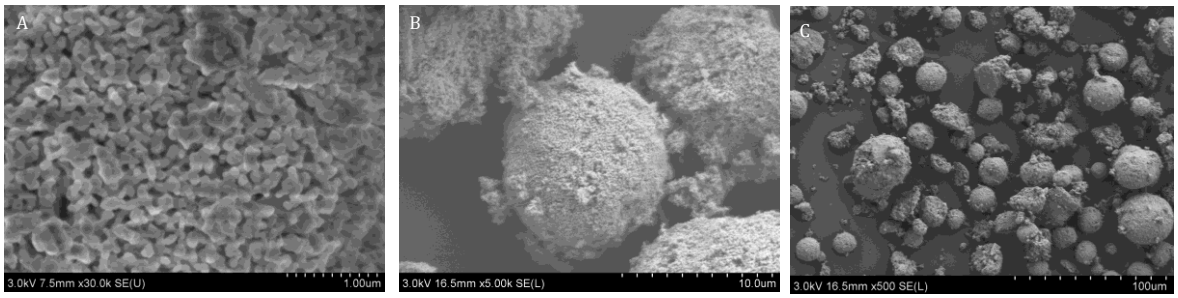

Figure 5.1: Scanning Electron Micrograph of Hydroxyapatite Microparticles. Hydroxyapatite microparticles were visualized via SEM. (A) Close examination of the microparticle surface shows a rough, porous environment. (B) Microparticle of approximately 7µm, porous environment. (C) microparticle sizes and morphologies

5.3.2 Characteristics of Alginate and HA/Alginate Beads

Different ratios of HA:alginate beads were characterized by light microscopy. Ratios of 05:95, 25:75, and 50:50 w/w hydroxyapatite:alginate were fabricated based on previous studies.[52]All bead

types had similar spherical morphologies. 50:50 beads had an average diameter of 2366.4 ± 32.8 µm. 25:75 beads had an average diameter of 2440.04 ± 62.2 µm. 05:95 beads had an average diameter of 2450.0 ± 82.4 µm. Figure 5 shows representative light microscope images of the different bead ratios. Qualitatively, hydroxyapatite particles appear to be evenly distributed throughout the alginate beads.

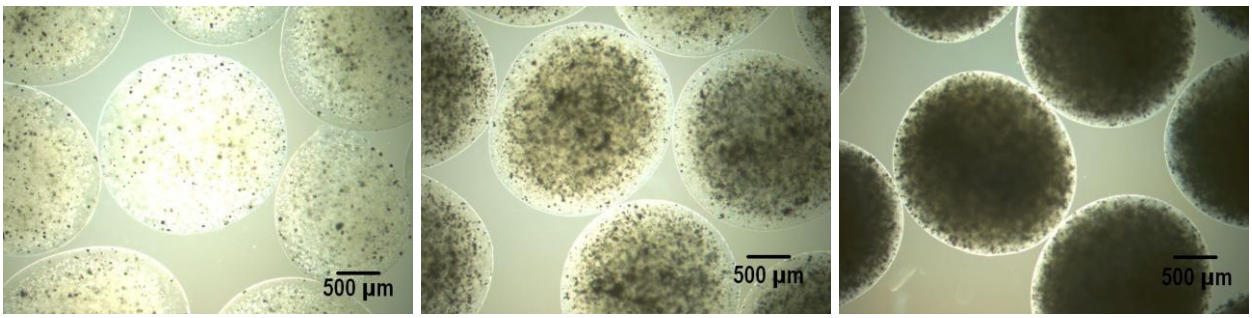

Figure 5.2: Light Microscope Images of HA:alginate Beads. Beads were visualized with a light microscope at 2.5x. (A) Image of 05:95 beads, (B) 25:75 beads, and (C) 50:50 beads. Scale bar represents 500 µm.

Alginate beads of each ratio were evaluated for swelling of the beads over a 28 day timeframe. Diameters of the beads were measured every 7 days for 28 days. A distribution of bead diameters was obtained on day 21 of the swelling study. Figure 5.3 shows a histogram of the results. Diameter of alginate beads decreased with increasing ratios of hydroxyapatite to alginate. The 50:50 ratio had an average diameter, which was significantly smaller than the both of the other HA doped beads ($p < 0.05$). The average diameter increase of the beads was 0.29 ± 0.031 mm, indicating a volume increase of 2.61 µL. There was no significant difference in the amount each group of beads swelled.

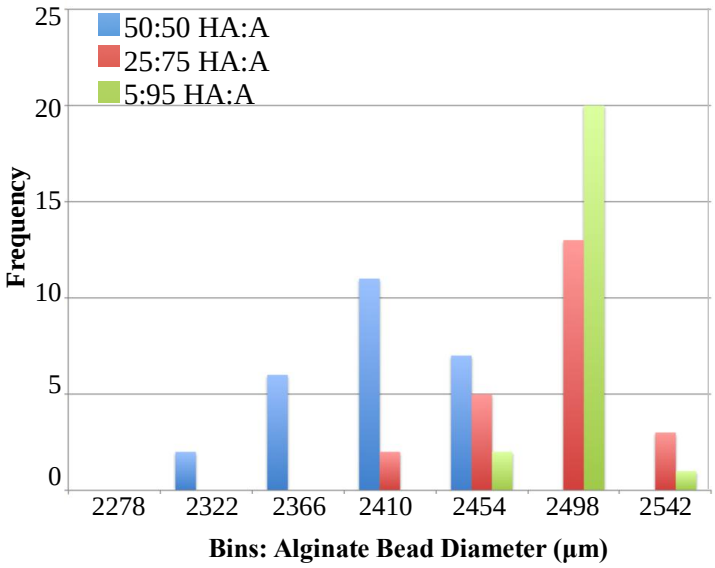

Figure 5.3: Histogram of HA:Alginate Beads After Swelling. Bead diameter were measured after 21 days of swelling using a 3-point circle on imaging software with a light microscope and digital camera attachment. Bin size was chosen based upon the average maximum and minimum bead sizes across the three groups. Histogram shows frequency versus bin number. Frequency was based on the number of samples less than the bin number. For example there were no beads with diameters less than 2278 µm so the frequency for that bin is zero.

5.3.4 Osteoblastic Differentiation for HA:Alginate Ratios

A 7 day cell culture study was carried out to determine the optimal HA:alginate ratio for osteoblastic differentiation. HMSCs were encapsulated in each ratio of HA:alginate beads and cultured under static osteogenic conditions for 7 days. Groups were assayed for ALP expression, DNA concentration, and gene expression at days 1, 4, and 7. The 50:50 ratio had the highest normalized ALP protein expression. Normalized ALP results are shown in Figure 5.4. Average DNA content was lowest for the 50:50 ratio at every time point. ALP protein expression and DNA quantification assays were not carried out on Day 4. ALP content was greatest for the 50:50 ratio at each time point.

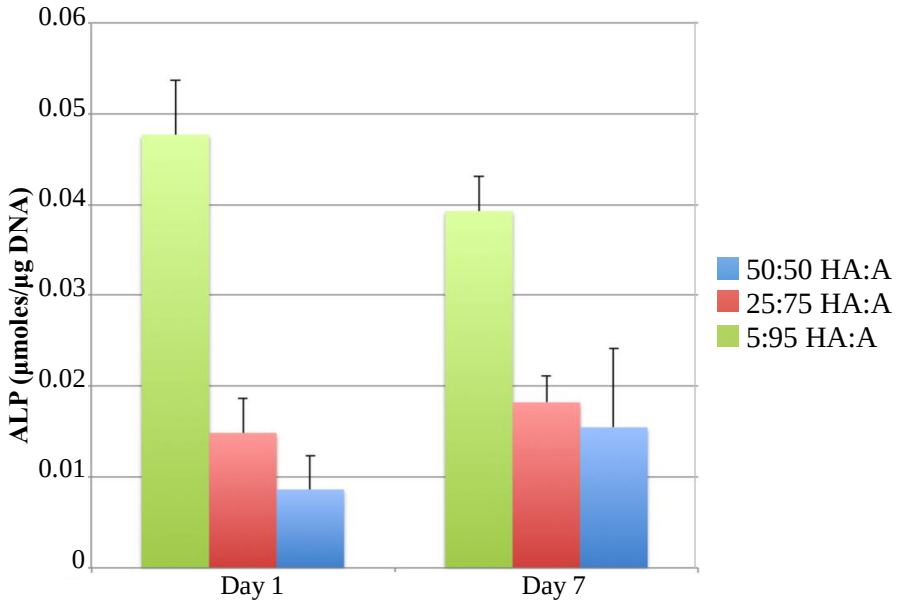

Figure 5.4: Normalized ALP Expression in HA Alginate Beads ALP expression of hMSCs was measured using the PNPP assay and normalized to DNA quantification using PicoGreen®.

Gene expression levels of osteoblastic genes were obtained using qRT-PCR. The 50:50 ratio showed the largest fold change for ALP and BMP-2 expression at day 7. Figure 5.5 shows the gene expression fold changes for ALP and BMP-2.

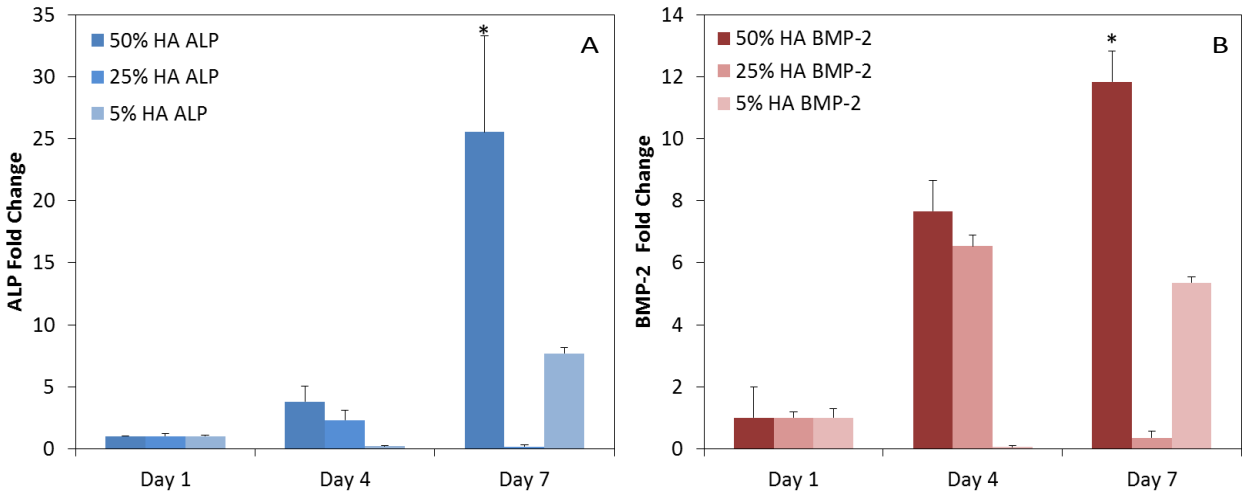

Figure 5.5: Osteoblastic Gene Expression of Various HA:Alginate Ratios. Gene expression of hMSCs in HA:alginate beads at three different ratios at days 1, 4, and 7. There was a significant difference (indicated by *) between the 50:50 alginate group and both of the other HA ratios at day 7 only for ALP fold change (A). There was also a significant difference between the 50:50 ratio and the other two ratios for BMP-2 at day 7 (B) ($p < 0.05$).

5.3.5 HA:Alginate Beads and Alginate Beads in Static and Dynamic Culture

A 21 day cell culture study was carried out to study the effects of HA doping on hMSC differentiation in alginate beads. HA doped beads at the 50:50 HA:alginate ratio and pure alginate beads were cultured at 1mL/minute. A second bioreactor was set up to culture HA doped beads at 2mL/minute to evaluate the effects of increased shear on HA doped beads. Static alginate beads were used as a control. Von Kossa and live/dead fluorescent imaging was evaluated for each group. Live/Dead qualitative fluorescent imaging was performed at days 1 and 20. Figure 5.6 shows the Live/Dead images for each group. All groups showed similar morphology and similar brightness representing live cells. On day 20, some staining was prevented due to the mineralization of the beads. Figure 5.7 shows an example of the mineralized beads from day 20 from the 2mL/minute HA doped group.

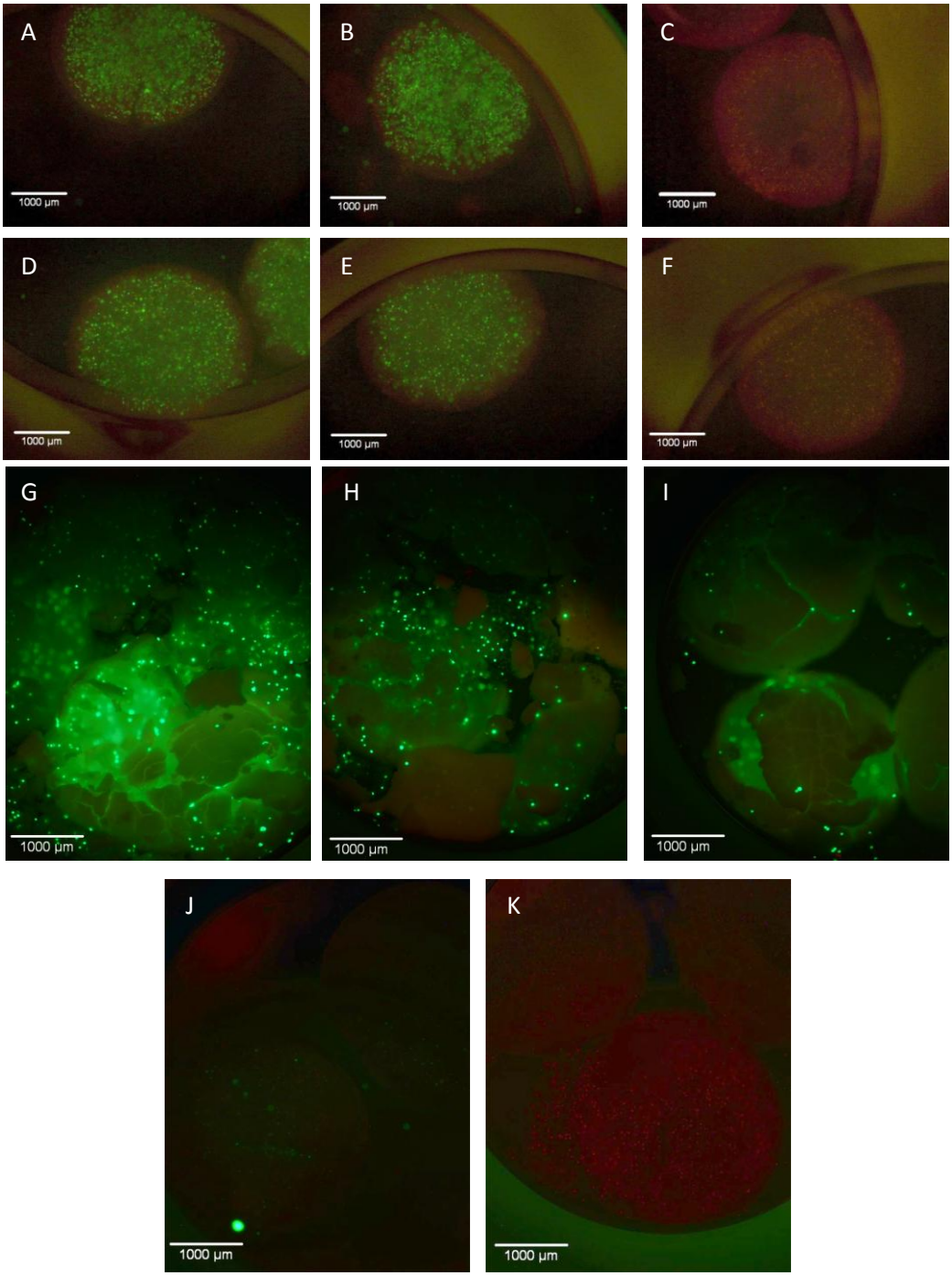

Figure 5.6: Fluorescence Imaging of HA Doped Beads. Live/Dead stain was used to stain each group. On Day 1 the (A) Static control and (B) alginate dynamic beads were visibly bright green and qualitatively alive compared to the (C) plain alginate dead control. (D) 1mL/minute and (E) 2mL/minute HA doped beads showed similar brightness and were qualitatively alive compared to the (F) HA doped dead. On Day 20, all beads showed significant mineralization, which may have prevented complete staining. (G) Day 20 alginate dynamic beads were qualitatively alive and staining was visible because the bead was broken prior to staining. (H) Shows the HA doped 1 ml/minute dynamic group and (I) shows the HA doped 2 ml/minute dynamic group. Both groups show green fluorescence and the stain-blocking effect of the mineralized shell (J) shows the static control, which had the most uniform mineralization and no breaks in the bead, therefore, little stain was taken up. (I) shows the dead control, which was fixed with methanol.

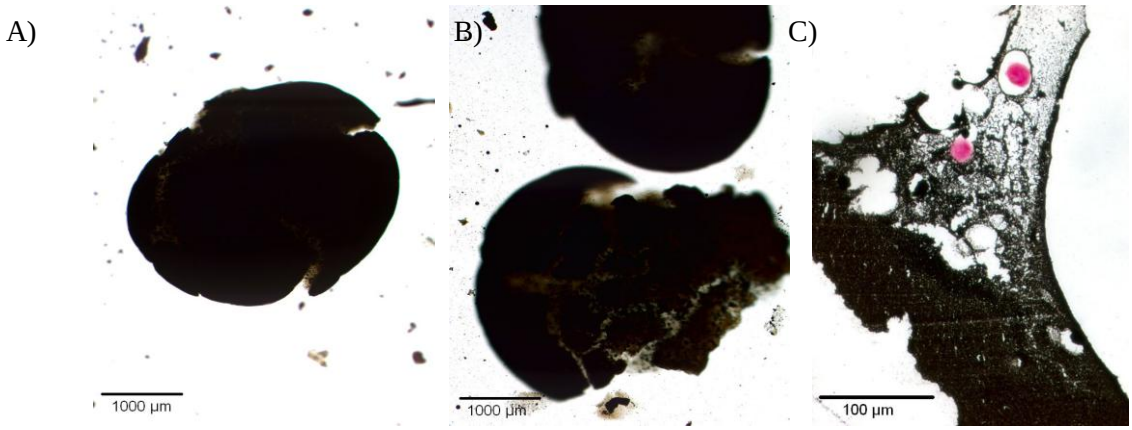

Figure 5.7: Mineralization of HA-Doped Alginate Beads. Mineralization of HA:alginate beads at day 20 of 2 ml/min dynamic culture conditions is extensive. (A, B) show the mineralization seen with light microscopy at 2.5x objective. Scale bar represents 1000 µm (C) Von Kossa staining shows mineralization (black) surrounding cell (pink), as well as some potential cell-HA interaction where the black dots are adjacent to the cell bodies. Scale bar represents 100 µm.

Von Kossa staining was carried was used to evaluate the osteoblastic differentiation of hMSCs, visualized as the production of mineralization within the ECM of the cells as shown in Figure 5.8. The HA doped beads showed the greatest production of mineralization. Both HA groups seemed to induce osteoblastic differentiation quicker than the either of the alginate groups. There did not seem to be a significant difference in mineralization production between the HA groups. However, all of the dynamic groups seemed to induce differentiation quicker than the static group. The morphology of the beads was most consistent across the time points for the static group, while the dynamic groups seemed to break apart over time in the bioreactor, losing their spherical morphology. Day 1 of the HA doped groups showed more staining than the alginate groups, however this is most likely staining from the HA particles within the bead. Interestingly, as shown in the 40x objective image of the HA 2mL/minute group, there does seem to be cellular interaction with the HA (Figure 5.7). At day 7, both HA groups showed much more mineralization than either of the alginate groups. At day 20, mineralization in the HA doped beads was much denser, as characterized by the black stain, than the static control.

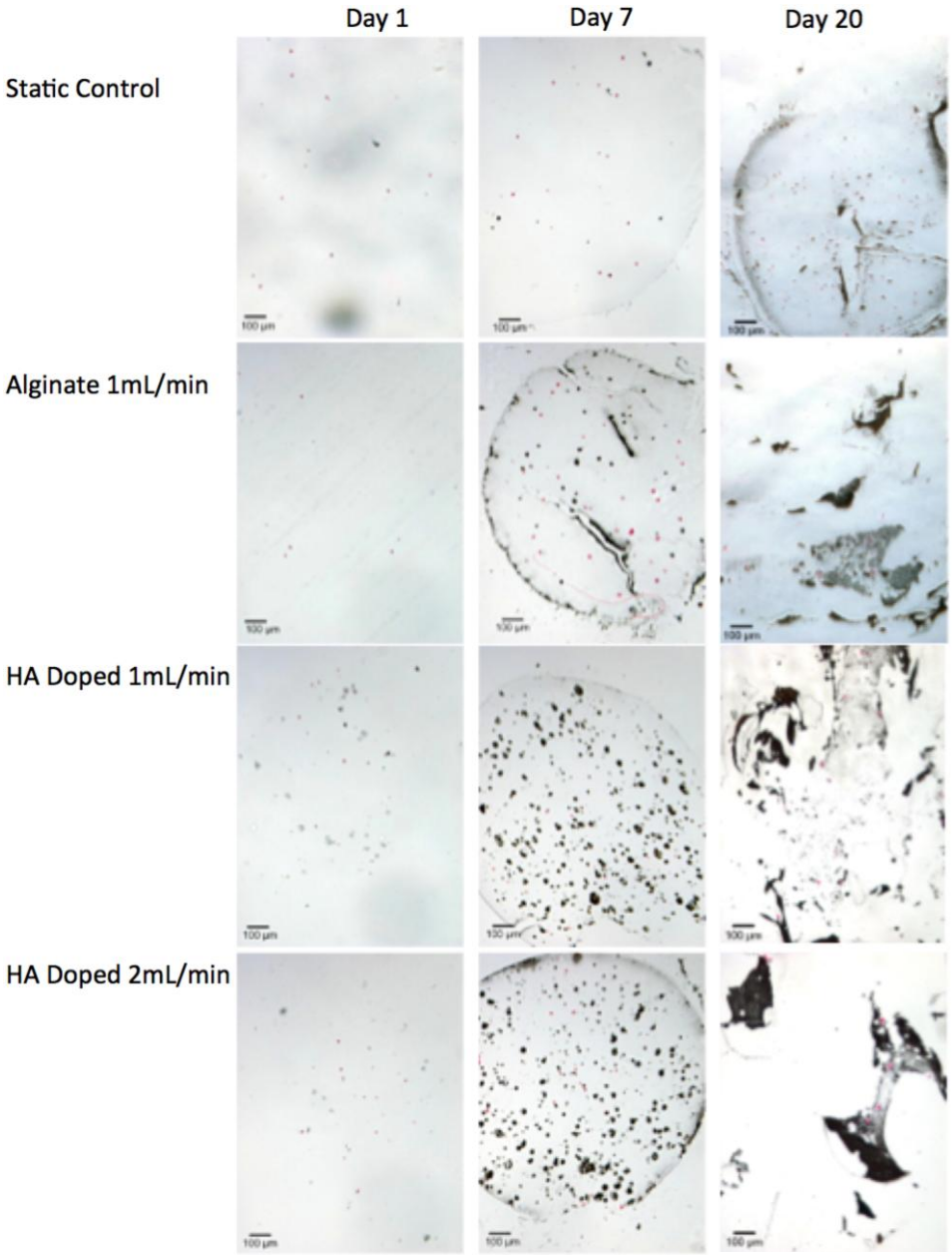

Figure 5.8: Mineralization of HA Doped Alginate Beads. Von Kossa staining showed increase mineralization in the HA-doped alginate beads. Mineralization increased from day 1 to day 20 in all groups, with the most increase shown in the HA doped beads. There was evident mineralization at day 7 in all groups as shown by the black staining. Pink stain shows cell nuclei, and there was also an increase in cell number from day 1 to day 7. Scale bars are 100µm.

5.4 Experimental Section: Discussion

This study showed that the surface of the hydroxyapatite microspheres was rough and porous (Figure 5.1). Dispersion of HA particles within alginate beads at various ratios was uniform, and beads were formed within a narrow distribution at each ratio, with the 50:50 ratio being significantly smaller than both of the other ratios. After 4 weeks of swelling, each swelled by an average of 2.61 μL. Each HA:alginate ratio contained 5.67 ± 0.16 μL of water. In a 7-day static culture comparison of each HA:alginate ratio, the 50:50 ratio showed the highest levels of normalized ALP expression. The fold changes for ALP and BMP-2 expression were significantly higher for the 50:50 ratio than either of the other ratios. Based upon these results, the 50:50 ratio was chosen for the 21-day dynamic study for comparison with alginate groups. By characterizing the HA doped alginate beads, this study demonstrated the feasibility and reliability of the fabrication methods for the creation of HA doped alginate beads as scaffolds for osteoblastic cell delivery.

Characterization of the hydroxyapatite microparticles showed the surface roughness of the spheres and the porosity of the HA. These characteristics may provide for a cell attachment site. Additionally, the nanoenvironment of the HA particles may provide interaction sites for cell excreted proteins and may act in a signaling manner to the hMSCs. There did not seem to be a significant difference in the free space of each bead. This is contrary to the expectation that, given the reduced size and increased density of the 50:50 ratio, there would not be similar amount of available space for cell proliferation.

The 7 day static comparison of HA doping ratios allowed for the selection of an optimal doping ratio and suggested that HA induces osteoblastic protein and gene expression in a dose dependent manner. However, the 50:50 also had the lowest DNA amount, this may indicate that cellular proliferation stops earlier in the higher HA ratio. DNA content stayed constant at day 7 and went down for the 25:75 and 50:50 ratios at day 14, while increasing for the 05:95 ratio. Gene expression of early osteoblastic

differentiation markers was greatest for the highest HA:alginate ratio. Both ALP and BMP-2 expression increased significantly in the 50:50 ratio at day 7. ALP expression increased over 25 fold in the 50:50 beads, and BMP-2 expression increased approximately 12 fold. The static culture condition allowed for the selection of the 50:50 ratio as the optimal ratio for increasing the rate of osteoblastic differentiation. Therefore this ratio was chosen to investigate as to the impact of HA under 21 day dynamic culture conditions.

The 21 day study showed that the HA doped groups outperform the alginate only groups when it comes to osteoblastic differentiation. Live/dead fluorescence imaging showed no significant reduction in viability in any group, although interpretation of the live/dead results was difficult due to the mineralization of the beads. All bead groups seemed to allow for cell viability at day 1, and at day 20 it was difficult to evaluate the viability of each group due to the mineralization of the beads, however, there was apparent viability in every group except for the static group, which may indicate that the mineralization of the static bead was more uniform than the dynamic beads, and that the outer layer of the alginate bead was intact. Light microscopy of the HA 2ml/minute beads showed a dense layer of mineralization surrounding the bead. Von Kossa staining showed that the HA doped groups produced mineralization at a quicker rate than the alginate groups at day 7 and at day 20 as well.

The von Kossa staining showed that the HA doped groups produce mineralization more rapidly than either of the alginate groups. There does not seem to be a large difference between the two HA groups which may indicate that the impact of HA doping is greater than the impact of shear on the differentiation of osteoblasts. However, this lack of difference may stem from too small of a difference in flow rates or too short of a comparison. Consistent with previous studies, the alginate 1mL/minute group outperformed the static control in terms of mineralization. From day 7 forward, it is evident that HA doping leads to increased mineralization and much denser mineralization, as evidenced by comparison of the staining. This density difference is especially apparent at 40x objective. Interestingly, in each case, the most mineralization seemed to localize to the edge of the alginate beads. It is unclear from this study why

mineralization localizes at the edge of the beads, although mass transport of nutrients, minerals, and oxygen at closer to the surface of the bead may allow for enhanced production of mineralization.

This study has shown that HA doping of alginate beads promotes osteoblastic differentiation in both static and dynamic culture. Although previous studies have demonstrated both the *in vivo* and *in vitro* osteoinductive properties of HA as both a scaffold and a dopant, they have not shown the effects of HA doping in alginate beads within a perfusion bioreactor. These findings are consistent with previous findings demonstrating the improved differentiation of hMSCs into osteoblasts in the presence of HA. The 50:50 ratio of HA to alginate exhibited the best osteogenic properties of the three ratios. Despite lower water content and lower DNA content, hMSCs within the 50:50 ratio produced the greatest amount of ALP in the 7-day static comparison study. Consistently, the 50:50 ratio also showed the greatest fold changes in both ALP and BMP-2 at day 7 compared to the other ratios. This suggests that HA doping may have a dose dependent effect on osteoblastic differentiation, although this would most likely be limited by the available space for cell proliferation within any scaffold. The finding that the 50:50 ratio performed better is supported by previous findings suggesting that HA improves cell adhesion.[52] Better cell anchoring within the alginate scaffolds could lead to more rapid osteoblastic differentiation and signaling. This study also demonstrates that HA can be easily incorporated into alginate based constructs as a dopant in readily controllable manner. Also results from the 7 and 21 day studies indicate that the HA doped alginate beads promote quicker differentiation of hMSCs into osteoblasts.

5.5 Conclusion

This study found that HA doping of alginate beads promotes osteoblastic differentiation *in vitro* in a dynamic TPS culture system. This induction improves the rate of differentiation further over that of dynamic culture of alginate beads. Further, an optimal differentiation-inducing ratio was determined. This approach may serve to shorten the culturing time of bone tissue engineering scaffolds, and ultimately reduce the time and cost required to create implantable, cell-loaded, bone tissue engineering scaffolds for use in large bone defects and bone grafts.

Chapter 6: Summary & Future Directions

6.1 Summary

The overall goal of this work was to develop functional biodegradable bone tissue engineering strategy. This work demonstrated that porous PPF scaffolds could be designed and fabricated to function as a carrier of precultured hMSC encapsulated in HA-doped alginate beads. Previous research has investigated the interaction of cells and PPF, *in vivo* and *in vitro*; however, no study looked specifically at the cytotoxicity of PPF through the three different exposure methods provided by the ISO standard 10993-5 as described in chapter 1. Therefore we show in chapter 2 that highly crosslinked PPF, with the soluble components removed, is noncytotoxic. Specifically, we demonstrate that highly crosslinked PPF elicits the same cellular response as a known noncytotoxic material (HDPE). We also showed that PPF films that are not highly crosslinked, may elicit a cellular response that is similar to other cytotoxic materials. This is important as it highlights the need to ensure that when utilizing PPF as a biomaterial, it is fully crosslinked and washed thoroughly to remove all soluble components before interacting with cells. Therefore, if PPF is highly crosslinked and the soluble components are removed we believe that it is suitable for use in tissue engineering applications. After establishing that PPF is suitable for use as a component *in vivo* we then investigated the design and fabrication of PPF-based scaffolds as described in Chapter 3.

Once we established that PPF did not elicit a cellular response, we looked to use it as the base of our resin to fabricate porous scaffolds. In chapter 3 we outline the design, fabrication and characterization of porous 3D printed PPF scaffolds. We developed a toolbox that could be used to evaluate 3D printed scaffolds. This toolbox may be used to identify scaffold designs for enhanced host integration. First modular design was used to investigate the wide range of scaffold parameters feasible with 3D printing. Then twelve scaffold designs were used to evaluate for their potential for vascularization when implanted *in vivo*. Vascularization evaluation was performed both quantitatively using an *in silico* model and

qualitatively with a nude rat study. These results provided a case study for a novel method to evaluate 3D printed scaffolds for tissue engineering. We proposed the application of this set of methods, or toolbox, to help design scaffolds to identify scaffold parameters that would be promising for improved vascularization when implanted *in vivo*.

Once we designed the scaffolds, we needed to ensure that they would function in the desired manner when implanted *in vivo*. To accomplish this we performed a degradation study of porous PPF scaffolds. This work is described in Chapter 4. We needed to determine if these 3D printed scaffolds would degrade as expected, allowing for the long term, noncytotoxic, mechanical stability of the defect site during degradation. As the PPF-based polymer scaffold degrades it produces byproducts. We investigated both the cellular response to the degradation byproducts as well as the structural and mechanical changes in the scaffold during degradation. We found that porous PPF scaffolds did not elicit a cytotoxic response during degradation. This is an important finding, as the degradation of PPF was found to lower the local pH by the release of fumaric acid. However, we believe that our results represent the greatest exposure of the degradation products since the body would be expected to remove these components faster than the timepoints evaluated. For example, all of the degradation that occurs between days 56 and 112 would not be exposed to the cellular environment all at one time but spread throughout the degradation process. Therefore these byproducts could be consumed over the 56 day period. Also in chapter 4 we show that our porous scaffold designs do not lose mechanical stability while degrading. This is critical for the delivery of our bioactive component of the graft, as it alone does not have the mechanical strength for direct implantation.

With chapters 2, 3, and 4 identifying that PPF scaffolds could be fabricated and degrade while providing long term mechanical support we were able to investigate the size and composition of the cell-laden alginate beads that would be the bioactive component housed in the lumen of the PPF scaffolds. This work is described in chapter 5. The objective of this work was twofold, one to produce small diameter beads to fill the PPF scaffolds with for *in vivo* implantation, and two, to determine if the addition

of HA to the alginate hydrogel could improve osteoblastic differentiation of hMSCs when cultured in the TPS bioreactor. These two goals were accomplished and we demonstrated that small diameter, hydroxyapatite (HA)-doped, alginate beads which encapsulated hMSCs could be reproducibly created. We also demonstrated that the addition of HA to these beads enhanced osteoblastic differentiation when cultured in the TPS bioreactor.

6.2 Proposed Future Work

This project focused on developing a bone tissue engineering solution using a porous 3D printed PPF scaffold to deliver hMSCs encapsulated in hydroxyapatite-doped alginate beads. Our goal was to provide long term mechanical stability while delivering a bioactive component to the bone defect site. However, one additional main objective for successful repair of bone defects would be to ensure vascularization of the defect site. Successful vascularization is understood to be at the heart of maintaining a viable cell population after implantation. Vascularization and the delivery of oxygen and nutrients has been identified as one of the major hurdles for successful cell implantation.[249] Other factors for successful repair of bone defects would focus on native tissue integration and subsequent *in vivo* evaluation.

6.2.1 Enhancing Rapid Vascularization

One area of interest for future work would be to enhance the ability of the scaffold for rapid vascularization once implanted into the bone defect. This could be investigated in a number of different studies including using PPF to delivery exogenous growth factors. Previous studies have used PPF for the controlled release of growth factors, corticoid steroids and even antibiotics.[277-279] In this same manner, PPF could be used to deliver vascular endothelial growth factor A (VEGFA), Fibroblastic Growth Factor 2 (FGF-2) and Platelet-Derived Growth Factor (PDGF) when acting as the carrier scaffold for the precultured alginate beads. Other methods to enhance vascularization could be to coculture

hMSCs with endothelial progenitor cells in the TPS bioreactor. Additionally the exogenous delivery of angiogenic growth factor, such as VEGFA, FGF-2 or PDGF, during TPS coculture could be investigated.

To follow up to the vascularization *in silico* modeling performed in chapter 6, we could perform an *in vivo* study that uses the suggested scaffold designs in a bone defect model to see if vascularization would occur as predicted. This would also be informative as it would help to understand if the small changes between groups as seen during *in silico* modeling have as significant of an impact when implanted *in vivo.*

6.2.2 Native Tissue Integration

Along with the release of growth factors to promote rapid vascularization, additional studies to investigate improved host tissue integration would be enlightening. Improved host tissue integration could be accomplished through improving the potential for cell adhesion to the scaffold surface and reducing the time to differentiation into osteoblasts. Changes such as increasing surface roughness, through acid washing or the addition of HA, could reduce the time to osteoblastic differentiation of hMSCs.[46, 280, 281] Enhanced surface roughness has also been linked to increased cell adhesion and osteoblast differentiation. [282, 283] To allow for native tissue integration and eventual replacement, we would also want to determine the point during degradation at which scaffolds would mechanically fail at physiological loads. This would tell us at which point the native tissue would have to be completely integrated with the scaffold.

6.2.3 Preclinical Studies

Some future work that could allow this project to be applied clinically would be for an i*n vivo* study to evaluate the combined strategy of the bioactive HA-doped alginate beads encapsulating hMSCs housed in porous 3D printed PPF scaffold. These studies would be modeled after previous *in vivo* studies using an athymic rat model with the inclusion of a 4mm defect, the size of a critical defect in rats.[284,

285] Additionally, 3D printing could be utilized to custom print scaffold to fit shape specific defects.[286] These unique scaffolds could be then filled with the bioactive HA-doped alginate beads for defect repair.

6.3 Closing Remarks

In closing, this dissertation outlines the work completed in the creation of a novel treatment for bone defects. We accomplished this through the combined approach of an absorbable porous hollow cylindrical scaffold that will provide mechanical support to the bioactive material housed in the lumen. We first demonstrated the biomaterial to be used for the porous scaffolds was noncytotoxic. Then we designed, fabricated and characterized the scaffolds using 3D printing, nondestructive characterization methods and an *in vivo* study. After fabrication and characterization, we performed a 224 day degradation study to investigate changes in scaffold mechanical and structural properties. In addition, we examined the potential of cytotoxicity from the degradation byproducts of the absorbable scaffold. Concurrently we developed the bioactive material that would be housed in the lumen of the porous scaffolds. The composition and size of bioactive material was studied for enhanced osteoblastic differentiation and reduced size to allow for ease of implantation within the porous scaffolds. Finally, future research was proposed for areas of additional investigation for improving the integration of the treatment method into the bone defect through rapid vascularization, enhanced native tissue integration, and preclinical studies. With further refinement and optimization our combined tissue engineering approach could provide for rapid and patient specific treatment of bone defects.

Bibliography

1. Dean, D., et al., *Continuous digital light processing (cDLP): Highly accurate additive manufacturing of tissue engineered bone scaffolds.* Virtual and Physical Prototyping, 2012. **7**(1): p. 13-24.
2. Giannoudis, P.V., H. Dinopoulos, and E. Tsiridis, *Bone substitutes: an update.* Injury, 2005. **36**(3): p. S20-S27.
3. Rezwan, K., et al., *Biodegradable and bioactive porous polymer/inorganic composite scaffolds for bone tissue engineering.* Biomaterials, 2006. **27**(18): p. 3413-3431.
4. Bauer, T.W. and G.F. Muschler, *Bone graft materials: an overview of the basic science.* Clinical orthopaedics and related research, 2000. **371**: p. 10.
5. Brown, K.L. and R.L. Cruess, *Bone and cartilage transplantation in orthopaedic surgery. A review.* The Journal of bone and joint surgery. American volume, 1982. **64**(2): p. 270.
6. Salgado, A.J., O.P. Coutinho, and R.L. Reis, *Bone tissue engineering: state of the art and future trends.* Macromolecular Bioscience, 2004. **4**(8): p. 743-765.
7. Uhthoff, H.K., P. Poitras, and D.S. Backman, *Internal plate fixation of fractures: short history and recent developments.* Journal of Orthopaedic Science, 2006. **11**(2): p. 118-126.
8. Burg, K.J.L., S. Porter, and J.F. Kellam, *Biomaterial developments for bone tissue engineering.* Biomaterials, 2000. **21**(23): p. 2347-2359.
9. Hollinger, J.O. and G.C. BATTISTONE, *Biodegradable bone repair materials synthetic polymers and ceramics.* Clinical orthopaedics and related research, 1986. **207**: p. 290.
10. Sabir, M., X. Xu, and L. Li, *A review on biodegradable polymeric materials for bone tissue engineering applications.* Journal of Materials Science, 2009. **44**(21): p. 5713-5724.
11. Ifkovits, J. and J. Burdick, *Review: Photopolymerizable and degradable biomaterials for tissue engineering applications.* Tissue Engineering, 2007. **13**(10): p. 2369-2385.
12. Hench, L.L. and J.M. Polak, *Third-Generation Biomedical Materials.* Science, 2002. **295**(5557): p. 1014-1017.
13. Karageorgiou, V. and D. Kaplan, *Porosity of 3D biomaterial scaffolds and osteogenesis.* Biomaterials, 2005. **26**(27): p. 5474-5491.
14. Abraham, G.A., et al., *Mechanical characterization of self-curing acrylic cements formulated with poly(methylmethacrylate)/poly(ϵ-caprolactone) beads.* Journal of Biomedical Materials Research Part B: Applied Biomaterials, 2004. **70B**(2): p. 340-347.
15. Rubin, J., C. Rubin, and C.R. Jacobs, *Molecular pathways mediating mechanical signaling in bone.* Gene, 2006. **367**: p. 1-16.
16. Peppas, N.A. and R. Langer, *New challenges in biomaterials.* Science, 1994. **263**(5154): p. 1715.
17. Rezwan, K., et al., *Biodegradable and bioactive porous polymer/inorganic composite scaffolds for bone tissue engineering.* Biomaterials, 2006. **27**(18): p. 3413-3431.
18. Orban, J.M., K.G. Marra, and J.O. Hollinger, *Composition options for tissue-engineered bone.* Tissue Engineering, 2002. **8**(4): p. 529-539.
19. Christopher, G., *Bone-grafting and bone-graft substitutes.* The Journal of Bone and Joint Surgery (American), 2002. **84**(3): p. 454-464.
20. Senn, N., *I. A New Method of Direct Fixation of the Fragments in Compound and Ununited Fractures.* Annals of Surgery, 1893. **18**(2): p. 125.
21. Perry, C.R., *Bone repair techniques, bone graft, and bone graft substitutes.* Clinical orthopaedics and related research, 1999. **360**: p. 71.
22. Pistner, H., et al., *Poly (l-lactide): a long-term degradation study in vivo:: Part II: physico-mechanical behaviour of implants.* Biomaterials, 1994. **15**(6): p. 439-450.
23. Engh, C., J. Bobyn, and A. Glassman, *Porous-coated hip replacement. The factors governing bone ingrowth, stress shielding, and clinical results.* J Bone Joint Surg Br, 1987. **69-B**(1): p. 45-55.
24. Disegi, J. and L. Eschbach, *Stainless steel in bone surgery.* Injury, 2000. **31**: p. D2-D6.
25. Gotman, I., *Characteristics of metals used in implants.* Journal of endourology, 1997. **11**(6): p. 383-389.
26. Uggowitzer, P.J., R. Magdowski, and M.O. Speidel, *Nickel free high nitrogen austenitic steels.* ISIJ international, 1996. **36**(7): p. 901-908.
27. Liu, X.Y., P.K. Chu, and C.X. Ding, *Surface modification of titanium, titanium alloys, and related materials for biomedical applications.* Materials Science & Engineering R-Reports, 2004. **47**(3-4): p. 49-121.

28. Long, M. and H. Rack, *Titanium alloys in total joint replacement-a materials science perspective.* BIOMATERIALS-GUILDFORD-, 1998. **19**: p. 1621-1639.
29. Matsuno, H., et al., *Biocompatibility and osteogenesis of refractory metal implants, titanium, hafnium, niobium, tantalum and rhenium.* Biomaterials, 2001. **22**(11): p. 1253-1262.
30. Spoerke, E.D., et al., *A bioactive titanium foam scaffold for bone repair.* Acta Biomaterialia, 2005. **1**(5): p. 523-533.
31. Pompe, W., et al., *Functionally graded materials for biomedical applications.* Materials Science and Engineering: A, 2003. **362**(1): p. 40-60.
32. Takeda, S., et al., *Cytotoxicity of pure metals].* Shika zairyō, kikai= Journal of the Japanese Society for Dental Materials and Devices, 1989. **8**(5): p. 648.
33. Watari, F., et al., *Biocompatibility of materials and development to functionally graded implant for bio-medical application.* Composites Science and Technology, 2004. **64**(6): p. 893-908.
34. Yamamuro, T., L.L. Hench, and J. Wilson, *CRC handbook of bioactive ceramics*1990: CRC press.
35. Stupp, S.I. and G.W. Ciegler, *Organoapatites: materials for artificial bone. I. Synthesis and microstructure.* Journal of biomedical materials research, 1992. **26**(2): p. 169-183.
36. Stupp, S.I., et al., *Organoapatites: materials for artificial bone. III. Biological testing.* Journal of biomedical materials research, 1993. **27**(3): p. 301-311.
37. Stupp, S.I., G.C. Mejicano, and J.A. Hanson, *Organoapatites: materials for artificial bone. II. Hardening reactions and properties.* Journal of biomedical materials research, 1993. **27**(3): p. 289-299.
38. Spoerke, E.D. and S.I. Stupp, *Colonization of organoapatite–titanium mesh by preosteoblastic cells.* Journal of Biomedical Materials Research Part A, 2003. **67**(3): p. 960-969.
39. Hollinger, J.O., et al., *Role of bone substitutes.* Clinical orthopaedics and related research, 1996. **324**: p. 55.
40. Wang, H., et al., *Biocompatibility and osteogenesis of biomimetic nano-hydroxyapatite/polyamide composite scaffolds for bone tissue engineering.* Biomaterials, 2007. **28**(22): p. 3338-3348.
41. Kveton, J.F., et al., *Reconstruction of suboccipital craniectomy defects with hydroxyapatite cement: a preliminary report.* The Laryngoscope, 1995. **105**(2): p. 156-159.
42. Costantino, P.D., et al., *Hydroxyapatite cement: I. Basic chemistry and histologic properties.* Archives of Otolaryngology- Head and Neck Surgery, 1991. **117**(4): p. 379.
43. Costantino, P.D., et al., *Experimental hydroxyapatite cement cranioplasty.* Plastic and reconstructive surgery, 1992. **90**(2): p. 174.
44. Lykins, C.L., et al., *Hydroxyapatite cement in craniofacial skeletal reconstruction and its effects on the developing craniofacial skeleton.* Archives of Otolaryngology- Head and Neck Surgery, 1998. **124**(2): p. 153.
45. Verret, D., et al., *Hydroxyapatite cement in craniofacial reconstruction.* Otolaryngology-Head and Neck Surgery, 2005. **133**(6): p. 897-899.
46. Kim, K., et al., *Early osteogenic signal expression of rat bone marrow stromal cells is influenced by both hydroxyapatite nanoparticle content and initial cell seeding density in biodegradable nanocomposite scaffolds.* Acta Biomater, 2010.
47. Laschke, M.W., et al., *Injectable nanocrystalline hydroxyapatite paste for bone substitution: in vivo analysis of biocompatibility and vascularization.* Journal of Biomedical Materials Research Part B: Applied Biomaterials, 2007. **82**(2): p. 494-505.
48. Itoh, S., et al., *The biocompatibility and osteoconductive activity of a novel hydroxyapatite/collagen composite biomaterial, and its function as a carrier of rhBMP-2.* Journal of biomedical materials research, 2001. **54**(3): p. 445-453.
49. Sun, J.-S., et al., *Effect of hydroxyapatite particle size on myoblasts and fibroblasts.* Biomaterials, 1997. **18**(9): p. 683-690.
50. Evans, E., *Toxicity of hydroxyapatite in vitro: the effect of particle size.* Biomaterials, 1991. **12**(6): p. 574-576.
51. Liu, C., et al., *Evaluation of the biocompatibility of a nonceramic hydroxyapatite*.* Journal of endodontics, 1997. **23**(8): p. 490-493.
52. Fisher, J.P., D. Dean, and A.G. Mikos, *Photocrosslinking characteristics and mechanical properties of diethyl fumarate/poly(propylene fumarate) biomaterials.* Biomaterials, 2002. **23**(22): p. 4333-43.
53. Elisseeff, J., et al., *Transdermal photopolymerization for minimally invasive implantation.* Proceedings of the National Academy of Sciences, 1999. **96**(6): p. 3104.
54. Nguyen, K.T. and J.L. West, *Photopolymerizable hydrogels for tissue engineering applications.* Biomaterials, 2002. **23**(22): p. 4307-4314.
55. Göpferich, A., *Mechanisms of polymer degradation and erosion.* Biomaterials, 1996. **17**(2): p. 103-114.
56. Habibovic, P. and K. de Groot, *Osteoinductive biomaterials—properties and relevance in bone repair.* Journal of tissue engineering and regenerative medicine, 2007. **1**(1): p. 25-32.
57. Jansen, J., et al., *Fumaric acid monoethyl ester-functionalized poly(D,L-lactide)/N-vinyl-2-pyrrolidone resins for the preparation of tissue engineering scaffolds by stereolithography.* Biomacromolecules, 2009. **10**(2): p. 214-20.
58. Kasper, F.K., et al., *Synthesis of poly(propylene fumarate).* Nat Protoc, 2009. **4**(4): p. 518-25.

59. Törmälä, P., et al., *Ultra high strength absorbable self reinforced polyglycolide (SR PGA) composite rods for internal fixation of bone fractures: In vitro and in vivo study.* Journal of biomedical materials research, 1991. **25**(1): p. 1-22.
60. Saha, S. and S. Pal, *Mechanical properties of bone cement: a review.* Journal of biomedical materials research, 1984. **18**(4): p. 435-462.
61. Hutmacher, D., *Scaffolds in tissue engineering bone and cartilage.* Biomaterials, 2000. **21**(24): p. 2529-2543.
62. Hutmacher, D.W., M. Sittinger, and M.V. Risbud, *Scaffold-based tissue engineering: rationale for computer-aided design and solid free-form fabrication systems.* Trends Biotechnol, 2004. **22**(7): p. 354-62.
63. Lee, K.W., et al., *Fabrication and characterization of poly(propylene fumarate) scaffolds with controlled pore structures using 3-dimensional printing and injection molding.* Tissue Eng, 2006. **12**(10): p. 2801-11.
64. Cooke, M.N., et al., *Use of stereolithography to manufacture critical-sized 3D biodegradable scaffolds for bone ingrowth.* J Biomed Mater Res B Appl Biomater, 2003. **64**(2): p. 65-9.
65. Holy, C., M. Shoichet, and J. Davies, *Engineering three-dimensional bone tissue in vitro using biodegradable scaffolds: Investigating initial cell-seeding density and culture period.* Journal of Biomedical Materials Research Part A, 2000. **51**(3): p. 376-382.
66. Golz, T., et al., *Temperature elevation during simulated polymethylmethacrylate (PMMA) cranioplasty in a cadaver model.* Journal of Clinical Neuroscience, 2010. **17**(5): p. 617-622.
67. Wang, L., et al., *Characterization of porous polymethylmethacrylate space maintainers for craniofacial reconstruction.* Journal of biomedical materials research. Part B, Applied biomaterials, 2013. **101**(5): p. 813-25.
68. Mousa, W.F., et al., *Biological and mechanical properties of PMMA-based bioactive bone cements.* Biomaterials, 2000. **21**(21): p. 2137-2146.
69. Arora, M., et al., *Polymethylmethacrylate bone cements and additives: A review of the literature.* World journal of orthopedics, 2013. **4**(2): p. 67-74.
70. Franco-Marques, E., et al., *Thermal and dynamic mechanical characterization of acrylic bone cements modified with biodegradable polymers.* Journal of Applied Polymer Science, 2013. **128**(5): p. 3455-3464.
71. Espigares, I., et al., *New partially degradable and bioactive acrylic bone cements based on starch blends and ceramic fillers.* Biomaterials, 2002. **23**(8): p. 1883-1895.
72. Kalteis, T., et al., *[Acute tissue toxicity of PMMA bone cements].* Z Orthop Ihre Grenzgeb, 2004. **142**(6): p. 666-72.
73. Lewis, G., *Properties of acrylic bone cement: state of the art review.* Journal of biomedical materials research, 1997. **38**(2): p. 155-182.
74. Lewis, G., *Alternative acrylic bone cement formulations for cemented arthroplasties: Present status, key issues, and future prospects.* Journal of Biomedical Materials Research Part B: Applied Biomaterials, 2008. **84B**(2): p. 301-319.
75. Melchels, F., J. Feijen, and D. Grijpma, *A review on stereolithography and its applications in biomedical engineering.* Biomaterials, 2010.
76. Dean, D., et al., *Effect of transforming growth factor beta 2 on marrow-infused foam poly(propylene fumarate) tissue-engineered constructs for the repair of critical-size cranial defects in rabbits.* Tissue Eng, 2005. **11**(5-6): p. 923-39.
77. Fisher, J.P., et al., *Effect of biomaterial properties on bone healing in a rabbit tooth extraction socket model.* J Biomed Mater Res A, 2004. **68**(3): p. 428-38.
78. Fisher, J.P., et al., *Soft and hard tissue response to photocrosslinked poly(propylene fumarate) scaffolds in a rabbit model.* Journal of biomedical materials research, 2002. **59**(3): p. 547-56.
79. Fisher, J.P., et al., *Synthesis and properties of photocross-linked poly(propylene fumarate) scaffolds.* Journal of Biomaterials Science Polymer Edition, 2001. **12**(6): p. 673-87.
80. Peter, S.J., et al., *Characterization of partially saturated poly(propylene fumarate) for orthopaedic application.* J Biomater Sci Polym Ed, 1997. **8**(11): p. 893-904.
81. Yaszemski, M.J., et al., *In vitro degradation of a poly(propylene fumarate)-based composite material.* Biomaterials, 1996. **17**(22): p. 2127-2130.
82. Lee, K.W., et al., *Poly(propylene fumarate) bone tissue engineering scaffold fabrication using stereolithography: effects of resin formulations and laser parameters.* Biomacromolecules, 2007. **8**(4): p. 1077-84.
83. Kim, K., et al., *Stereolithographic Bone Scaffold Design Parameters: Osteogenic Differentiation and Signal Expression.* Tissue Engineering Part B: Reviews, 2010. **16**(5): p. 523-539.
84. Wallace JE, S.A., Wang MO, Kyobum K, Fisher JP, Mikos AG, and Dean D. *Continuous DLP Rendering of Tissue Engineering Scaffolds. Where Discovery Meets Innovation.* in *TERMIS-NA 2010 Annual Conference*. 2010. Orlando, FL.
85. Nguyen, K. and J. West, *Photopolymerizable hydrogels for tissue engineering applications.* Biomaterials, 2002. **23**(22): p. 4307-4314.
86. Hasirci, V., et al., *PLGA bone plates reinforced with crosslinked PPF.* J Mater Sci Mater Med, 2002. **13**(2): p. 159-67.
87. Hedberg, E.L., et al., *In vitro degradation of porous poly(propylene fumarate)/poly(DL-lactic-co-glycolic acid) composite scaffolds.* Biomaterials, 2005. **26**(16): p. 3215-25.
88. Yeatts, A.B. and J.P. Fisher, *Tubular perfusion system for the long-term dynamic culture of human mesenchymal stem cells.* Tissue Eng Part C Methods, 2011. **17**(3): p. 337-48.

89. Park, J.C., et al., *Evaluation of the cytotoxicity of polyetherurethane (PU) film containing zinc diethyldithiocarbamate (ZDEC) on various cell lines.* Yonsei medical journal, 2002. **43**(4): p. 518.
90. Tsuchiya, T., *Studies on the standardization of cytotoxicity tests and new standard reference materials useful for evaluating the safety of biomaterials.* Journal of biomaterials applications, 1994. **9**(2): p. 138-157.
91. Shi, X., et al., *Poly (propylene fumarate)*2006: CRC Press: Boca Raton, FL.
92. Tsuchiya, T., et al., *In vivo tissue/biomaterials toxic responses: Correlation with cytotoxic potential but not cell attachment.* Clinical materials, 1994. **16**(1): p. 1-8.
93. Oliva, A., et al., *Biocompatibility studies on glass ionomer cements by primary cultures of human osteoblasts.* Biomaterials, 1996. **17**(13): p. 1351-1356.
94. Anand, V.P., *Biocompatibility Safety Assessment of Medical Devices: FDA/ISO and Japanese Guidelines.* Medical Device & Diagnostic Industry, January, 2000.
95. International Organization for Standardization, *Biological evaluation of medical devices*, in *ISO 10993: parts 1 - 12*Various, ISO: Geneva, Switzerland.
96. Kim, M.-N., et al., *Toxicity and biodegradation of products from polyester hydrolysis.* Journal of Environmental Science and Health, Part A, 2001. **36**(4): p. 447-463.
97. Pagga, U., *Testing biodegradability with standardized methods.* Chemosphere, 1997. **35**(12): p. 2953-2972.
98. Allori, A.C., A.M. Sailon, and S.M. Warren, *Biological basis of bone formation, remodeling, and repair - Part I: Biochemical signaling molecules.* Tissue Engineering Part B-Reviews, 2008. **14**(3): p. 259-273.
99. Zhang, Y., et al., *The effects of Runx2 immobilization on poly (-caprolactone) on osteoblast differentiation of bone marrow stromal cells in vitro.* Biomaterials, 2010.
100. Westendorf, J.J., R.A. Kahler, and T.M. Schroeder, *Wnt signaling in osteoblasts and bone diseases.* Gene, 2004. **341**: p. 19-39.
101. Lian, J.B., et al., *Regulatory controls for osteoblast growth and differentiation: Role of Runx/Cbfa/AML factors.* Critical Reviews in Eukaryotic Gene Expression, 2004. **14**(1-2): p. 1-41.
102. Yoon, D.M. and J.P. Fisher, *Chondrocyte signaling and artificial matrices for articular cartilage engineering.* Tissue Engineering, 2007: p. 67-86.
103. Leipzig, N.D., S.V. Eleswarapu, and K.A. Athanasiou, *The effects of TGF-[beta] 1 and IGF-I on the biomechanics and cytoskeleton of single chondrocytes.* Osteoarthritis and Cartilage, 2006. **14**(12): p. 1227-1236.
104. Davies, L.C., et al., *The Potential of IGF-1 and TGF 1 for Promoting Adult" Articular Cartilage Repair: An In Vitro Study.* Tissue Engineering Part A, 2008. **14**(7): p. 1251-1261.
105. Almarza, A.J. and K.A. Athanasiou, *Design Characteristics for the Tissue Engineering of Cartilaginous Tissues.* Annals of Biomedical Engineering, 2004. **32**(1): p. 2-17.
106. Shakibaei, M., C. Csaki, and A. Mobasheri, *Diverse roles of integrin receptors in articular cartilage*2008: Springer Verlag.
107. Mollenhauer, J.A., *Perspectives on articular cartilage biology and osteoarthritis.* Injury, 2008. **39**(1, Supplement 1): p. 5-12.
108. Otero, M. and M.B. Goldring, *Cells of the synovium in rheumatoid arthritis. Chondrocytes.* Arthritis Research & Therapy, 2007. **9**(5): p. 220.
109. Burrage, P.S., K.S. Mix, and C.E. Brinckerhoff, *Matrix metalloproteinases: Role in arthritis.* Frontiers in Bioscience, 2006. **11**: p. 529-543.
110. Millward-Sadler, S.J. and D.M. Salter, *Integrin-dependent signal cascades in chondrocyte mechanotransduction.* Annals of Biomedical Engineering, 2004. **32**(3): p. 435-446.
111. Van der Kraan, P.M., et al., *Interaction of chondrocytes, extracellular matrix and growth factors: relevance for articular cartilage tissue engineering.* Osteoarthritis and Cartilage, 2002. **10**(8): p. 631-637.
112. Woods, A., G. Wang, and F. Beier, *Regulation of chondrocyte differentiation by the actin cytoskeleton and adhesive interactions.* Journal of Cellular Physiology, 2007. **213**(1): p. 1-8.
113. Zuscik, M.J., et al., *Regulation of chondrogenesis and chondrocyte differentiation by stress.* The Journal of Clinical Investigation, 2008. **118**(2): p. 429-438.
114. Yamane, S. and A.H. Reddi, *Induction of chondrogenesis and superficial zone protein accumulation in synovial side population cells by BMP-7 and TGF- 1.* Journal of orthopaedic research, 2008. **26**(4): p. 485-492.
115. Di Guglielmo, G.M., et al., *Distinct endocytic pathways regulate TGF-[beta] receptor signalling and turnover.* Nat Cell Biol, 2003. **5**(5): p. 410-421.
116. Le Roy, C. and J.L. Wrana, *Clathrin-and non-clathrin-mediated endocytic regulation of cell signalling.* Nature Reviews Molecular Cell Biology, 2005. **6**(2): p. 112-126.
117. Pujol, J.-P., et al., *Interleukin-1 and Transforming Growth Factor-ss 1 as Crucial Factors in Osteoarthritic Cartilage Metabolism.* Connective Tissue Research, 2008. **49**(3/4): p. 293-297.
118. Starkman, B.G., et al., *IGF-I stimulation of proteoglycan synthesis by chondrocytes requires activation of the PI 3-kinase pathway but not ERK MAPK.* Biochemical Journal, 2005. **389**(Pt 3): p. 723.

119. Baserga, R., et al., *The IGF-I receptor in cell growth, transformation and apoptosis.* Biochimica et Biophysica Acta (BBA) - Reviews on Cancer, 1997. **1332**(3): p. F105-F126.
120. Giustina, A., G. Mazziotti, and E. Canalis, *Growth Hormone, Insulin-Like Growth Factors, and the Skeleton.* Endocr Rev, 2008. **29**(5): p. 535-559.
121. Govoni, K., D.J. Baylink, and S. Mohan, *The multi-functional role of insulin-like growth factor binding proteins in bone.* Pediatric Nephrology, 2005. **20**(3): p. 261-268.
122. Conover, C.A., *Insulin-like growth factor-binding proteins and bone metabolism.* Am J Physiol Endocrinol Metab, 2008. **294**(1): p. E10-14.
123. Samani, A.A., et al., *The role of the IGF system in cancer growth and metastasis: overview and recent insights.* Endocrine Reviews, 2007. **28**(1): p. 20.
124. Perrini, S., et al., *The GH/IGF1 axis and signaling pathways in the muscle and bone: mechanisms underlying age-related skeletal muscle wasting and osteoporosis.* J Endocrinol, 2010. **205**(3): p. 201-210.
125. Humbel, R., E. , *Insulin-like growth factors I and II.* European Journal of Biochemistry, 1990. **190**(3): p. 445-462.
126. Bernstein, A., H.O. Mayr, and R. Hube, *Can bone healing in distraction osteogenesis be accelerated by local application of IGF-1 and TGF- 1?* Journal of Biomedical Materials Research Part B: Applied Biomaterials, 2010. **92**(1): p. 215-225.
127. Zhang, M., et al., *IGF-1 regulation of type II collagen and MMP-13 expression in rat endplate chondrocytes via distinct signaling pathways.* Osteoarthritis and cartilage / OARS, Osteoarthritis Research Society, 2009. **17**(1): p. 100-106.
128. Malemud, C.J., *Cytokines as Therapeutic Targets for Osteoarthritis.* BioDrugs, 2004. **18**(1): p. 23-35.
129. Wang, J., et al., *Insulin-like growth factor 1-induced interleukin-1 receptor II overrides the activity of interleukin-1 and controls the homeostasis of the extracellular matrix of cartilage.* Arthritis & Rheumatism, 2003. **48**(5): p. 1281-1291.
130. Wang, Y.-J., et al., *Insulin-Like Growth Factor-1 Treatment Prevents Anti-Fas Antibody-Induced Apoptosis in Endplate Chondrocytes.* Spine, 2006. **31**(7): p. 736-741 10.1097/01.brs.0000208128.49912.64.
131. Hay, E., et al., *Bone morphogenetic protein receptor IB signaling mediates apoptosis independently of differentiation in osteoblastic cells.* Journal of Biological Chemistry, 2004. **279**(3): p. 1650-1658.
132. Massague, J., *THE TRANSFORMING GROWTH-FACTOR-BETA FAMILY.* Annual Review of Cell Biology, 1990. **6**: p. 597-641.
133. Massague, J., *TGF-beta signal transduction.* Annual Review of Biochemistry, 1998. **67**: p. 753-791.
134. Janssens, K., et al., *Transforming growth factor-beta 1 to the bone.* Endocrine Reviews, 2005. **26**(6): p. 743-774.
135. Selvamurugan, N., et al., *Transforming growth factor- 1 regulation of collagenase-3 expression in osteoblastic cells by cross-talk between the Smad and MAPK signaling pathways and their components, Smad2 and Runx2.* Journal of Biological Chemistry, 2004. **279**(18): p. 19327.
136. Massagué, J. and R.R. Gomis, *The logic of TGF [beta] signaling.* FEBS letters, 2006. **580**(12): p. 2811-2820.
137. Moustakas, A. and C.H. Heldin, *Non-Smad TGF-beta signals.* Journal of Cell Science, 2005. **118**(16): p. 3573-3584.
138. Canalis, E., A.N. Economides, and E. Gazzerro, *Bone morphogenetic proteins, their antagonists, and the skeleton.* Endocrine Reviews, 2003. **24**(2): p. 218-235.
139. Massagué, J., J. Seoane, and D. Wotton, *Smad transcription factors.* Genes & development, 2005. **19**(23): p. 2783.
140. Miyazono, K., *TGF-[beta] signaling by Smad proteins.* Cytokine & Growth Factor Reviews, 2000. **11**(1-2): p. 15-22.
141. Izzi, L. and L. Attisano, *Regulation of the TGF signalling pathway by ubiquitin-mediated degradation.* Oncogene, 2004. **23**(11): p. 2071-2078.
142. Blaney Davidson, E.N., P.M. van der Kraan, and W.B. Van Den Berg, *TGF-[beta] and osteoarthritis.* Osteoarthritis and Cartilage, 2007. **15**(6): p. 597-604.
143. Sykaras, N. and L.A. Opperman, *Bone morphogenetic proteins (BMPs): how do they function and what can they offer the clinician?* Journal of Oral Science, 2003. **45**(2): p. 57-74.
144. Darling, E.M. and K.A. Athanasiou, *Growth factor impact on articular cartilage subpopulations.* Cell and tissue research, 2005. **322**(3): p. 463-473.
145. Li, T.F. and R.J. O'Keefe, *TGF- signaling in chondrocytes.* Frontiers in bioscience: a journal and virtual library, 2005. **10**: p. 681.
146. Roman-Blas, J.A., D.G. Stokes, and S.A. Jimenez, *Modulation of TGF-[beta] signaling by proinflammatory cytokines in articular chondrocytes.* Osteoarthritis and Cartilage, 2007. **15**(12): p. 1367-1377.
147. Lires-Deán, M., et al., *Anti-apoptotic effect of transforming growth factor-[beta]1 on human articular chondrocytes: role of protein phosphatase 2A.* Osteoarthritis and Cartilage, 2008. **16**(11): p. 1370-1378.
148. Edwards, D.R., et al., *Differential effects of transforming growth factor-[beta] 1 on the expression of matrix metalloproteinases and tissue inhibitors of metalloproteinases in young and old human fibroblasts.* Experimental gerontology, 1996. **31**(1-2): p. 207-223.
149. Edwards, D.R., et al., *Transforming growth factor beta modulates the expression of collagenase and metalloproteinase inhibitor.* The EMBO journal, 1987. **6**(7): p. 1899.
150. Koay, E.J., G. Ofek, and K.A. Athanasiou, *Effects of TGF- 1 and IGF-I on the compressibility, biomechanics, and strain-dependent recovery behavior of single chondrocytes.* Journal of biomechanics, 2008. **41**(5): p. 1044-1052.

151. Urist, M.R., *Bone: Formation by Autoinduction.* Science, 1965. **150**(3698): p. 893-899.
152. Xiao, Y.-T., L.-X. Xiang, and J.-Z. Shao, *Bone morphogenetic protein.* Biochemical and biophysical research communications, 2007. **362**(3): p. 550-553.
153. Balemans, W. and W. Van Hul, *Extracellular regulation of BMP signaling in vertebrates: a cocktail of modulators.* Developmental biology, 2002. **250**(2): p. 231-250.
154. Bessa, P.C., M. Casal, and R.L. Reis, *Bone morphogenetic proteins in tissue engineering: the road from the laboratory to the clinic, part I (basic concepts).* Journal of Tissue Engineering and Regenerative Medicine, 2008. **2**(1): p. 1-13.
155. Gazzerro, E. and C. Minetti, *Potential drug targets within bone morphogenetic protein signaling pathways.* Current Opinion in Pharmacology, 2007. **7**(3): p. 325-333.
156. Cao, X. and D. Chen, *The BMP signaling and in vivo bone formation.* Gene, 2005. **357**(1): p. 1-8.
157. Haÿ, E., et al., *Bone morphogenetic protein-2 promotes osteoblast apoptosis through a Smad-independent, protein kinase C-dependent signaling pathway.* Journal of Biological Chemistry, 2001. **276**(31): p. 29028.
158. Miyazono, K., S. Maeda, and T. Imamura, *BMP receptor signaling: Transcriptional targets, regulation of signals, and signaling cross-talk.* Cytokine & Growth Factor Reviews, 2005. **16**(3): p. 251-263.
159. Gründer, T., et al., *Bone morphogenetic protein (BMP)-2 enhances the expression of type II collagen and aggrecan in chondrocytes embedded in alginate beads* 1.* Osteoarthritis and Cartilage, 2004. **12**(7): p. 559-567.
160. Bluteau, G., et al., *VEGF and VEGF receptors are differentially expressed in chondrocytes.* Bone, 2007. **40**(3): p. 568-576.
161. Klooster, A.R. and S.M. Bernier, *Tumor necrosis factor alpha and epidermal growth factor act additively to inhibit matrix gene expression by chondrocyte.* Arthritis Res Ther, 2005. **7**(1): p. R127-38.
162. Khalafi, A., et al., *Increased accumulation of superficial zone protein (SZP) in articular cartilage in response to bone morphogenetic protein-7 and growth factors.* Journal of orthopaedic research, 2007. **25**(3): p. 293-303.
163. Chubinskaya, S., M. Hurtig, and D.C. Rueger, *OP-1/BMP-7 in cartilage repair.* International Orthopaedics, 2007. **31**(6): p. 773-781.
164. Saadeh, P.B., et al., *Mechanisms of fibroblast growth factor-2 modulation of vascular endothelial growth factor expression by osteoblastic cells.* Endocrinology, 2000. **141**(6): p. 2075.
165. Ferrara, N., *Vascular endothelial growth factor: Basic science and clinical progress.* Endocrine Reviews, 2004. **25**(4): p. 581-611.
166. Dai, J. and A.B.M. Rabie, *VEGF: an essential mediator of both angiogenesis and endochondral ossification.* Journal of dental research, 2007. **86**(10): p. 937.
167. Tombran-Tink, J. and C.J. Barnstable, *Osteoblasts and osteoclasts express PEDF, VEGF-A isoforms, and VEGF receptors: possible mediators of angiogenesis and matrix remodeling in the bone.* Biochemical and biophysical research communications, 2004. **316**(2): p. 573-579.
168. Murata, M., K. Yudoh, and K. Masuko, *The potential role of vascular endothelial growth factor (VEGF) in cartilage: How the angiogenic factor could be involved in the pathogenesis of osteoarthritis?* Osteoarthritis and Cartilage, 2008. **16**(3): p. 279-286.
169. Hofmann, A., et al., *Cell viability, osteoblast differentiation, and gene expression are altered in human osteoblasts from hypertrophic fracture non-unions.* Bone, 2008. **42**(5): p. 894-906.
170. Vincent, T.L., et al., *FGF-2 is bound to perlecan in the pericellular matrix of articular cartilage, where it acts as a chondrocyte mechanotransducer.* Osteoarthritis and Cartilage, 2007. **15**(7): p. 752-763.
171. Takai, S., et al., *Activation of phosphatidylinositol 3-kinase/Akt limits FGF-2-induced VEGF release in osteoblasts.* Molecular and cellular endocrinology, 2007. **267**(1-2): p. 46-54.
172. Xing, L. and B.F. Boyce, *Regulation of apoptosis in osteoclasts and osteoblastic cells.* Biochemical and biophysical research communications, 2005. **328**(3): p. 709-720.
173. Veilleux, N. and M. Spector, *Effects of FGF-2 and IGF-1 on adult canine articular chondrocytes in type II collagen-glycosaminoglycan scaffolds in vitro.* Osteoarthritis and Cartilage, 2005. **13**(4): p. 278-286.
174. Boch, J.A., N. Wara-Aswapati, and P.E. Auron, *CONCISE REVIEW Biological: Interleukin 1 Signal Transduction--Current Concepts and Relevance to Periodontitis.* Journal of dental research, 2001. **80**(2): p. 400.
175. Saklatvala, J., *Inflammatory Signaling in Cartilage: MAPK and NF-B Pathways in Chondrocytes and the Use of Inhibitors for Research into Pathogenesis and Therapy of Osteoarthritis.* Current Drug Targets, 2007. **8**(2): p. 305-313.
176. Fan, Z.Y., et al., *IL-1 beta induction of IL-6 and LIF in normal articular human chondrocytes involves the ERK, p38 and NF kappa B signaling pathways.* Cytokine, 2004. **28**(1): p. 17-24.
177. Roman-Blas, J.A. and S.A. Jimenez, *Targeting NF-kappa B: A Promising Molecular Therapy in Inflammatory Arthritis.* International Reviews of Immunology, 2008. **27**(5): p. 351-374.
178. Bankers-Fulbright, J.L., K.R. Kalli, and D.J. McKean, *Interleukin-1 signal transduction.* Life Sciences, 1996. **59**(2): p. 61-83.
179. Blanchard, F., et al., *The dual role of IL-6-type cytokines on bone remodeling and bone tumors.* Cytokine & Growth Factor Reviews, 2009. **20**(1): p. 19-28.

180. Wang, H., et al., *Apoptosis induced by NO via phosphorylation of p38 MAPK that stimulates NF-[kappa] B, p53 and caspase-3 activation in rabbit articular chondrocytes.* Cell biology international, 2007. **31**(9): p. 1027-1035.
181. Bonizzi, G. and M. Karin, *The two NF-[kappa]B activation pathways and their role in innate and adaptive immunity.* Trends in Immunology, 2004. **25**(6): p. 280-288.
182. Gowen, M., et al., *An interleukin 1 like factor stimulates bone resorption in vitro.* Nature, 1983. **306**: p. 378-380.
183. Fujisaki, K., et al., *The effect of IL-1[alpha] on the expression of matrix metalloproteinases, plasminogen activators, and their inhibitors in osteoblastic ROS 17/2.8 cells.* Life Sciences, 2006. **78**(17): p. 1975-1982.
184. Tanabe, N., et al., *IL-1[alpha] affects mineralized nodule formation by rat osteoblasts.* Life Sciences, 2004. **75**(19): p. 2317-2327.
185. Tanabe, N., et al., *IL-1[alpha] stimulates the formation of osteoclast-like cells by increasing M-CSF and PGE2 production and decreasing OPG production by osteoblasts.* Life Sciences, 2005. **77**(6): p. 615-626.
186. Tsuboi, M., et al., *Tumor necrosis factor-[alpha] and interleukin-1 [beta] increase the Fas-mediated apoptosis of human osteoblasts.* Journal of Laboratory and Clinical Medicine, 1999. **134**(3): p. 222-231.
187. Lee, D.A., et al., *The influence of mechanical loading on isolated chondrocytes seeded in agarose constructs.* Biorheology, 2000. **37**(1): p. 149-161.
188. Mundy, G.R., *Osteoporosis and Inflammation.* Nutrition Reviews, 2007. **65**: p. S147-S151.
189. Steeve, K.T., et al., *IL-6, RANKL, TNF-alpha/IL-1: interrelations in bone resorption pathophysiology.* Cytokine & Growth Factor Reviews, 2004. **15**(1): p. 49-60.
190. Franchimont, N., S. Wertz, and M. Malaise, *Interleukin-6: An osteotropic factor influencing bone formation?* Bone, 2005. **37**(5): p. 601-606.
191. Nanes, M.S., *Tumor necrosis factor-alpha: molecular and cellular mechanisms in skeletal pathology.* Gene, 2003. **321**: p. 1-15.
192. Yamazaki, M., et al., *Tumor Necrosis Factor alpha Represses Bone Morphogenetic Protein (BMP) Signaling by Interfering with the DNA Binding of Smads through the Activation of NF-kappa B.* Journal of Biological Chemistry, 2009. **284**(51): p. 35987-35995.
193. Kaneki, H., et al., *Tumor necrosis factor promotes Runx2 degradation through up-regulation of Smurf1 and Smurf2 in osteoblasts.* Journal of Biological Chemistry, 2006. **281**(7): p. 4326-4333.
194. Lehmann, W., et al., *Tumor necrosis factor alpha (TNF-alpha) coordinately regulates the expression of specific matrix metalloproteinases (MMPS) and angiogenic factors during fracture healing.* Bone, 2005. **36**(2): p. 300-310.
195. Djouad, F., et al., *ERK1/2 Activation Induced by Inflammatory Cytokines Compromises Effective Host Tissue Integration of Engineered Cartilage.* Tissue Engineering Part A, 2009. **15**(10): p. 2825.
196. Sondergaard, B.C., et al., *MAPKs are essential upstream signaling pathways in proteolytic cartilage degradation - divergence in pathways leading to aggrecanase and MMP-mediated articular cartilage degradation.* Osteoarthritis and Cartilage, 2009. **18**(3): p. 279-288.
197. Qin, L., L.J. Raggatt, and N.C. Partridge, *Parathyroid hormone: a double-edged sword for bone metabolism.* Trends in Endocrinology and Metabolism, 2004. **15**(2): p. 60-65.
198. Perrini, S., et al., *Abnormalities of insulin-like growth factor-I signaling and impaired cell proliferation in osteoblasts from subjects with osteoporosis.* Endocrinology, 2008. **149**(3): p. 1302.
199. Bellido, T., et al., *Proteasomal degradation of Runx2 shortens parathyroid hormone-induced anti-apoptotic signaling in osteoblasts.* Journal of Biological Chemistry, 2003. **278**(50): p. 50259.
200. Ehling, A., et al., *The potential of adiponectin in driving arthritis.* The Journal of Immunology, 2006. **176**(7): p. 4468.
201. Lago, R., et al., *A new player in cartilage homeostasis: adiponectin induces nitric oxide synthase type II and pro-inflammatory cytokines in chondrocytes.* Osteoarthritis and Cartilage, 2008. **16**(9): p. 1101-1109.
202. Oshima, K., et al., *Adiponectin increases bone mass by suppressing osteoclast and activating osteoblast.* Biochemical and biophysical research communications, 2005. **331**(2): p. 520-526.
203. Liedert, A., et al., *Signal transduction pathways involved in mechanotransduction in bone cells.* Biochemical and biophysical research communications, 2006. **349**(1): p. 1-5.
204. Damsky, C.H., *Extracellular matrix-integrin interactions in osteoblast function and tissue remodeling.* Bone, 1999. **25**(1): p. 95-96.
205. Katsumi, A., et al., *Integrins in mechanotransduction.* Journal of Biological Chemistry, 2004. **279**(13): p. 12001-12004.
206. Giancotti, F.G. and E. Ruoslahti, *Integrin signaling.* Science, 1999. **285**(5430): p. 1028.
207. Loeser, R.F., *Chondrocyte integrin expression and function.* Biorheology, 2000. **37**(1): p. 109-116.
208. Loeser, R.F., *Integrins and cell signaling in chondrocytes.* Biorheology, 2002. **39**(1): p. 119-124.
209. Guo, W. and F.G. Giancotti, *Integrin signalling during tumour progression.* Nature Reviews Molecular Cell Biology, 2004. **5**(10): p. 816-826.
210. Liedert, A., et al., *Estrogen receptor and Wnt signaling interact to regulate early gene expression in response to mechanical strain in osteoblastic cells.* Biochemical and biophysical research communications, 2010. **394**(3): p. 755-759.

211. Sanchez, C., et al., *Osteoblast: A cell under compression.* Bio-Medical Materials & Engineering, 2008. **18**(4/5): p. 221-224.
212. Lee, D.A., et al., *Response of chondrocyte subpopulations cultured within unloaded and loaded agarose.* Journal of orthopaedic research, 1998. **16**(6): p. 726-733.
213. Villanueva, I., C.A. Weigel, and S.J. Bryant, *Cell-matrix interactions and dynamic mechanical loading influence chondrocyte gene expression and bioactivity in PEG-RGD hydrogels.* Acta Biomaterialia, 2009. **5**(8): p. 2832-2846.
214. Preiss-Bloom, O., et al., *Real-time monitoring of force response measured in mechanically stimulated tissue-engineered cartilage.* Artificial Organs, 2009. **33**(4): p. 318-327.
215. Chowdhury, T.T., et al., *Integrin-mediated mechanotransduction in IL-1 stimulated chondrocytes.* Biomechanics and Modeling in Mechanobiology, 2006. **5**(2): p. 192-201.
216. Vanderploeg, E.J., C.G. Wilson, and M.E. Levenston, *Articular chondrocytes derived from distinct tissue zones differentially respond to in vitro oscillatory tensile loading.* Osteoarthritis and Cartilage, 2008. **16**(10): p. 1228-1236.
217. Blanco, F.J., et al., *Chondrocyte apoptosis induced by nitric oxide.* The American journal of pathology, 1995. **146**(1): p. 75.
218. Rezwan, K., et al., *Biodegradable and bioactive porous polymer/inorganic composite scaffolds for bone tissue engineering.* Biomaterials, 2006. **27**(18): p. 3413-3431.
219. Kim, K., et al., *Effect of Initial Cell Seeding Density on Early Osteogenic Signal Expression of Rat Bone Marrow Stromal Cells Cultured on Cross-Linked Poly(propylene fumarate) Disks.* Biomacromolecules, 2009. **10**(7): p. 1810-1817.
220. He, S., et al., *Injectable biodegradable polymer composites based on poly(propylene fumarate) crosslinked with poly(ethylene glycol)-dimethacrylate.* Biomaterials, 2000. **21**(23): p. 2389-94.
221. Peter, S.J., et al., *In vivo degradation of a poly(propylene fumarate)/β-tricalcium phosphate injectable composite scaffold.* Journal of biomedical materials research, 1998. **41**(1): p. 1-7.
222. Timmer, M.D., C.G. Ambrose, and A.G. Mikos, *In vitro degradation of polymeric networks of poly(propylene fumarate) and the crosslinking macromer poly(propylene fumarate)-diacrylate.* Biomaterials, 2003. **24**(4): p. 571-7.
223. Kempen, D.H., et al., *Retention of in vitro and in vivo BMP-2 bioactivities in sustained delivery vehicles for bone tissue engineering.* Biomaterials, 2008. **29**(22): p. 3245-52.
224. Lewandrowski, K.U., et al., *Porous poly(propylene fumarate) foam coating of orthotopic cortical bone grafts for improved osteoconduction.* Tissue Engineering, 2002. **8**(6): p. 1017-27.
225. Vehof, J.W., et al., *Bone formation in transforming growth factor beta-1-coated porous poly(propylene fumarate) scaffolds.* Journal of Biomedical Materials Research, 2002. **60**(2): p. 241-51.
226. Fisher, J.P., et al., *Photoinitiated cross-linking of the biodegradable polyester poly(propylene fumarate). Part II. In vitro degradation.* Biomacromolecules, 2003. **4**(5): p. 1335-42.
227. Timmer, M.D., et al., *In vitro cytotoxicity of injectable and biodegradable poly(propylene fumarate)-based networks: unreacted macromers, cross-linked networks, and degradation products.* Biomacromolecules, 2003. **4**(4): p. 1026-33.
228. Kasper, F.K., et al., *Synthesis of poly(propylene fumarate).* Nature Protocols, 2009. **4**(4): p. 518-25.
229. Kim, K., et al., *Early osteogenic signal expression of rat bone marrow stromal cells is influenced by both hydroxyapatite nanoparticle content and initial cell seeding density in biodegradable nanocomposite scaffolds.* Acta Biomaterialia, 2011. **7**(3): p. 1249-1264.
230. Charlesby, A., S. Pinner, and S. Pinner, *Analysis of the solubility behaviour of irradiated polyethylene and other polymers.* Proceedings of the Royal Society of London. Series A. Mathematical and Physical Sciences, 1959. **249**(1258): p. 367-386.
231. Yeatts, A.B., et al., *Human mesenchymal stem cell position within scaffolds influences cell fate during dynamic culture.* Biotechnology and Bioengineering, 2012. **109**(9): p. 2381-91.
232. Betz, M.W., et al., *Macroporous hydrogels upregulate osteogenic signal expression and promote bone regeneration.* Biomacromolecules, 2010. **11**(5): p. 1160-8.
233. Betz, M.W., et al., *Cyclic acetal hydrogel system for bone marrow stromal cell encapsulation and osteodifferentiation.* Journal of Biomedical Materials Research A, 2008. **86**(3): p. 662-70.
234. Chen, J.-P., G.-Y. Chang, and J.-K. Chen, *Electrospun collagen/chitosan nanofibrous membrane as wound dressing.* Colloids and Surfaces A: Physicochemical and Engineering Aspects, 2008. **313–314**(0): p. 183-188.
235. Velayudhan, S., et al., *Biological evaluation of pliable hydroxyapatite–ethylene vinyl acetate co-polymer composites intended for cranioplasty.* Acta biomaterialia, 2005. **1**(2): p. 201-209.
236. La Gatta, A., et al., *A Novel Injectable Poly (ε-caprolactone)/Calcium Sulfate System for Bone Regeneration: Synthesis and Characterization.* Macromolecular bioscience, 2005. **5**(11): p. 1108-1117.
237. Timmer, M.D., et al., *Fabrication of poly(propylene fumarate)-based orthopaedic implants by photo-crosslinking through transparent silicone molds.* Biomaterials, 2003. **24**(25): p. 4707-14.
238. Tsuchiya, T., et al., *Comparative studies of the toxicity of standard reference materials in various cytotoxicity tests and in vivo implantation tests.* Journal of Applied Biomaterials, 1993. **4**(2): p. 153-6.
239. Yamamoto, A., R. Honma, and M. Sumita, *Cytotoxicity evaluation of 43 metal salts using murine fibroblasts and*

osteoblastic cells. Journal of biomedical materials research, 1998. **39**(2): p. 331-340.
240. Kim, K., et al., *The influence of stereolithographic scaffold architecture and composition on osteogenic signal expression with rat bone marrow stromal cells.* Biomaterials, 2011. **32**(15): p. 3750-63.
241. Kim, K., et al., *Early osteogenic signal expression of rat bone marrow stromal cells is influenced by both hydroxyapatite nanoparticle content and initial cell seeding density in biodegradable nanocomposite scaffolds.* Acta Biomaterialia, 2010.
242. Mygind, T., et al., *Mesenchymal stem cell ingrowth and differentiation on coralline hydroxyapatite scaffolds.* Biomaterials, 2007. **28**(6): p. 1036-47.
243. Das, A. and E. Botchwey, *Evaluation of angiogenesis and osteogenesis.* Tissue Eng Part B Rev, 2011. **17**(6): p. 403-14.
244. Chang, B.-S., et al., *Osteoconduction at porous hydroxyapatite with various pore configurations.* Biomaterials, 2000. **21**(12): p. 1291-1298.
245. ASTM, *Standard Test Method for Compressive Properties of Rigid Plastics*, in *D 695*, ASTM International: West Conshohocken, PA.
246. Fisher, J.P., et al., *Soft and hard tissue response to photocrosslinked poly(propylene fumarate) scaffolds in a rabbit model.* Journal of biomedical materials research, 2002. **59**(3): p. 547-556.
247. Wang, M.O., et al., *Evaluation of the in vitro cytotoxicity of cross-linked biomaterials.* Biomacromolecules, 2013. **14**(5): p. 1321-9.
248. Wettergreen, M., et al., *Creation of a unit block library of architectures for use in assembled scaffold engineering.* Computer-Aided Design, 2005. **37**(11): p. 1141-1149.
249. Johnson, P.C., et al., *Strategic directions in tissue engineering.* Tissue engineering, 2007. **13**(12): p. 2827-2837.
250. Hutmacher, D.W., *Scaffolds in tissue engineering bone and cartilage.* Biomaterials, 2000. **21**(24): p. 2529-2543.
251. Hollister, S.J., *Porous scaffold design for tissue engineering.* Nat Mater, 2005. **4**(7): p. 518-24.
252. Kim, K., et al., *Stereolithographic bone scaffold design parameters: osteogenic differentiation and signal expression.* Tissue Eng Part B Rev, 2010. **16**(5): p. 523-39.
253. Klawitter, J. and S. Hulbert, *Application of porous ceramics for the attachment of load bearing internal orthopedic applications.* Journal of biomedical materials research, 1971. **5**(6): p. 161-229.
254. Yang, S., et al., *The design of scaffolds for use in tissue engineering. Part I. Traditional factors.* Tissue engineering, 2001. **7**(6): p. 679-689.
255. Klenke, F.M., et al., *Impact of pore size on the vascularization and osseointegration of ceramic bone substitutes in vivo.* Journal of Biomedical Materials Research Part A, 2008. **85**(3): p. 777-786.
256. Artel, A., et al., *An agent-based model for the investigation of neovascularization within porous scaffolds.* Tissue Engineering Part A, 2011. **17**(17-18): p. 2133-2141.
257. Russell, W.M.S. and R.L. Burch, *The principles of humane experimental technique*1959, London,: Methuen. 238 p.
258. Mehdizadeh, H., et al., *Three-dimensional modeling of angiogenesis in porous biomaterial scaffolds.* Biomaterials, 2013. **34**(12): p. 2875-87.
259. *Repast Home Page*. 2012 [cited 2013; Available from: http://repast.sourceforge.net/.
260. North, M.J., et al., *Complex adaptive systems modeling with repast simphony.* Complex adaptive systems modeling, 2013. **1**(1): p. 1-26.
261. Moya, M.L., et al., *The effect of FGF-1 loaded alginate microbeads on neovascularization and adipogenesis in a vascular pedicle model of adipose tissue engineering.* Biomaterials, 2010. **31**(10): p. 2816-26.
262. Wallace, J., et al., *Validating continuous digital light processing (cDLP) additive manufacturing accuracy and tissue engineering utility of a dye-initiator package.* Biofabrication, 2014. **6**(1): p. 015003.
263. Hollister, S.J., *Porous scaffold design for tissue engineering.* Nature materials, 2005. **4**(7): p. 518-524.
264. Mikos, A.G. and J.S. Temenoff, *Formation of highly porous biodegradable scaffolds for tissue engineering.* Electronic Journal of Biotechnology, 2000. **3**(2): p. 23-24.
265. Altmeyer, P.J., et al., *Antipsoriatic effect of fumaric acid derivatives: results of a multicenter double-blind study in 100 patients.* Journal of the American Academy of Dermatology, 1994. **30**(6): p. 977-981.
266. MO Wang, V.C., Dreher ML, Mott EJ, Cheng MH, Cinar A, Mehdizadeh H, Somo S, Dean D, Brey EM and JP Fisher., *Evaluating 3D Printed Biomaterials: A Novel Approach Using Poly(Propylene Fumarate) Scaffolds.* (In review), 2014.
267. Yang, S., et al., *The design of scaffolds for use in tissue engineering. Part I. Traditional factors.* Tissue Engineering, 2001. **7**(6): p. 679-689.
268. ASTM, *Standard Test Method for in vitro Degradation Testing of Hydrolytically Degradable Polymer Resins and Fabricated Forms for Surgical Implants*, in *F1635*: West Conshohocken, PA.
269. ASTM, *Standard Practice for Assessment of Compatibility of Absorbable/Resorbable Biomaterials for Implant Applications*, in *F1983*, ASTM International: West Conshohocken, PA.
270. ASTM, *Standard Guide for Characterization and Testing of Biomaterial Scaffolds Used in Tissue-Engineered Medical Products*, in *F2150 - 07* 2007: West Conshohocken, PA.
271. He, S., et al., *Synthesis of biodegradable poly(propylene fumarate) networks with poly(propylene fumarate)–diacrylate*

macromers as crosslinking agents and characterization of their degradation products. Polymer, 2001. **42**(3): p. 1251-1260.
272. Kong, H.J., et al., *Controlling rigidity and degradation of alginate hydrogels via molecular weight distribution.* Biomacromolecules, 2004. **5**(5): p. 1720-1727.
273. Pisanti, P., et al., *Tubular perfusion system culture of human mesenchymal stem cells on poly-L-lactic acid scaffolds produced using a supercritical carbon dioxide-assisted process.* J Biomed Mater Res A, 2012. **100**(10): p. 2563-72.
274. Yeatts, A.B. and J.P. Fisher, *Bone tissue engineering bioreactors: dynamic culture and the influence of shear stress.* Bone, 2011. **48**(2): p. 171-81.
275. Yeatts, A.B. and J.P. Fisher, *Tubular perfusion system for the long-term dynamic culture of human mesenchymal stem cells.* Tissue Engineering Part C: Methods, 2010. **17**(3): p. 337-348.
276. Betz, M.W., et al., *Cyclic acetal hydrogel system for bone marrow stromal cell encapsulation and osteodifferentiation.* Journal of Biomedical Materials Research Part A, 2008. **86**(3): p. 662-70.
277. Gerhart, T.N., et al., *Antibiotic release from an experimental biodegradable bone cement.* J Orthop Res, 1988. **6**(4): p. 585-92.
278. Haesslein, A., et al., *Long-term release of fluocinolone acetonide using biodegradable fumarate-based polymers.* J Control Release, 2006. **114**(2): p. 251-60.
279. Kempen, D.H., et al., *Effect of autologous bone marrow stromal cell seeding and bone morphogenetic protein-2 delivery on ectopic bone formation in a microsphere/poly(propylene fumarate) composite.* Tissue Eng Part A, 2009. **15**(3): p. 587-94.
280. Balloni, S., et al., *Effects of titanium surface roughness on mesenchymal stem cell commitment and differentiation signaling.* International Journal of Oral & Maxillofacial Implants, 2009. **24**(4).
281. Zhao, F., et al., *Effects of hydroxyapatite in 3-D chitosan–gelatin polymer network on human mesenchymal stem cell construct development.* Biomaterials, 2006. **27**(9): p. 1859-1867.
282. Wall, I., et al., *Modified titanium surfaces promote accelerated osteogenic differentiation of mesenchymal stromal cells< i> in vitro</i>.* Bone, 2009. **45**(1): p. 17-26.
283. *Polymers in surgical repair.* Food Cosmet Toxicol, 1973. **11**(2): p. 314-8.
284. Yeatts, A.B., et al., *In vivo bone regeneration using tubular perfusion system bioreactor cultured nanofibrous scaffolds.* Tissue Engineering Part A, 2013. **20**(1-2): p. 139-146.
285. Watanabe, Y., et al., *Establishment of reproducible critical size bone defect model in rat femur.* Tissue engineering, 2014(ja).
286. Holzwarth, J.M. and P.X. Ma, *Biomimetic nanofibrous scaffolds for bone tissue engineering.* Biomaterials, 2011. **32**(36): p. 9622-9629.